



# **Finite Element Method Simulations of Redox Processes in Nanoporous Gold and in Lithium Batteries**

(Finite-Elemente-Methoden-Simulationen von Redoxprozessen in nanoporösem Gold und in Lithiumbatterien)

Von der Fakultät für Mathematik und Naturwissenschaften  
der Carl von Ossietzky Universität Oldenburg  
zur Erlangung des Grades und Titels

Doktor der Naturwissenschaften (Dr. rer. nat.)  
angenommene Dissertation

von Herrn **Luis Humberto Balboa Blanco**, MSc.  
geboren am 23. April 1981 in Mexiko-Stadt, Mexiko

Oldenburg, Oktober 2025

Gutachter: Prof. Dr. Gunther Wittstock

Zweitgutachter: Prof. Dr. Dmitry Momotenko

Tag der Disputation: 06. März 2026

Die Dissertationsarbeit wurde von Mai 2015 bis Mai 2020 an der Carl von Ossietzky Universität Oldenburg, in der Fakultät für Mathematik und Naturwissenschaften im Institut für Chemie unter der Anleitung von Prof. Dr. Gunther Wittstock angefertigt. Die experimentellen Arbeiten zu nanoporosem Gold wurden von Mareike Hänsch durchgeführt, die zu Platin auf Kohlenstoff von Julian Behnken und die zu Lithiumelektroden von Bastian Krüger, alle aus der AG Wittstock an der Carl von Ossietzky Universität Oldenburg. Alle externen Beiträge zu dieser Arbeit sind in den jeweiligen Kapiteln beschrieben. Die veröffentlichten Teile der Dissertation sind mit [X#] gekennzeichnet und in Kapitel 9.1 aufgeführt.

## **Abstract**

This thesis investigates the transport phenomena in nanoporous electrodes and in lithium electrodes using a combination of scanning electrochemical microscopy (SECM) and finite element method (FEM) simulations. The primary goal is to develop and validate analytical models that accurately describe key properties such as porosity, film thickness, and current density distribution in electrochemical systems with complex geometries. Initial studies are devoted to heterogeneous models of nanoporous gold (NPG) and platinum on carbon (Pt/C), highlighting how variations in pore structure impact electrochemical responses. These findings led to the development of improved analytical equations that capture the dynamics of mass transport more effectively.

Subsequently, homogeneous models are introduced to simplify the representation of transport by diffusion properties while maintaining accuracy across a range of porosities. A new analytical equation for SECM approach curves was developed, validated through simulations, and shown to be applicable under diverse experimental conditions. The thesis further examines lithium electrodes and SEI evolution using numerical simulations to model the secondary current density distribution under realistic conditions. The results demonstrate how probe positioning and geometry affect the local current density distribution and data interpretation, offering practical guidance for minimizing measurement artefacts in SEI studies. Overall, this work provides valuable tools for optimizing electrode design and contributes to advancing high-performance electrochemical systems.

## Zusammenfassung

Diese Dissertation untersucht die Transportphänomene in nanoporösen Elektroden und Lithium-Elektroden mithilfe einer Kombination aus elektrochemischer Rastermikroskopie (SECM, *scanning electrochemical microscopy*) und Simulationen mit der Methode der finiten Elemente (FEM). Das Hauptziel besteht darin, analytische Modelle zu entwickeln und zu validieren, die Schlüsseleigenschaften wie Porosität, Schichtdicke und Stromdichteverteilung in komplexen elektrochemischen Systemen genau beschreiben. Zunächst werden heterogene Modelle von nanoporösem Gold (NPG) und Platin auf Kohlenstoff (Pt/C) vorgestellt, wobei deutlich wird, wie Variationen in der Porenstruktur die elektrochemischen Reaktionen beeinflussen. Diese Erkenntnisse führten zur Entwicklung verbesserter analytischer Gleichungen, die die Dynamik des Massentransports effektiver erfassen.

Anschließend werden homogene Modelle eingeführt, um die Darstellung der Transporteigenschaften zu vereinfachen, während die Genauigkeit über einen breiten Porositätsbereich erhalten bleibt. Eine neue analytische Gleichung für SECM-Annäherungskurven wurde entwickelt, durch Simulationen validiert und erwies sich als anwendbar unter unterschiedlichen experimentellen Bedingungen. Die Arbeit untersucht auch Lithium-Elektroden und die Entwicklung der Festelektrolyt-Grenzschicht (SEI) mithilfe numerischer Simulationen, mit denen die sekundäre Stromdichteverteilung unter realistischen Bedingungen modelliert wird. Die Ergebnisse zeigen, wie die Positionierung und Geometrie der SECM-Sonde die lokale Stromdichteverteilung und die Datenauswertung beeinflussen, und liefern praktische Hinweise zur Minimierung von Messartefakten in SEI-Studien. Insgesamt bietet diese Arbeit wertvolle Werkzeuge zur Optimierung des Elektroden-designs und leistet einen Beitrag zur Weiterentwicklung leistungsfähiger elektrochemischer Systeme.

## **Acknowledgments**

I would like to express my sincere gratitude to Prof. Dr. Gunther Wittstock for providing the interesting research topic and for supervising my work throughout all these years. His detailed and critical insights, constructive ideas for progress, and continuous support have been invaluable for the completion of this thesis. I am also grateful to Prof. Dr. Dmitry Momotenko for kindly taking on the role of second examiner.

I would like to thank Mareike for the many great and constructive discussions, both scientific and otherwise, throughout our time together during the PhD, and to Julian for always being such a nice person to talk to and for his support and contributions during our joint work. I also wish to thank Bastian for the insightful discussions regarding the lithium SECM setup.

I would like to thank all colleagues and friends of the Wittstock group for creating such a great and lively working atmosphere, with many special moments both inside and outside the university. I am especially grateful to Abdallatif for his exceptional kindness and the moments we shared.

Finally, I wish to express my deepest gratitude to my family. First to my parents, Abi and Toto, and now to Julia and our children Emil and Teo, for their unconditional support and patience, without which my studies and this work would not have been possible. Muchas gracias por todo.

# Table of Contents

<b>1. Introduction .....</b>	<b>1</b>
<b>2. Modelling of electrochemical processes.....</b>	<b>3</b>
2.1 Mass transport.....	3
2.2 Interfacial reactions .....	4
2.3 Scanning electrochemical microscopy .....	6
2.3.1 Microelectrodes.....	7
2.3.2 Working principle of feedback mode.....	9
2.3.3 Surface interrogation mode.....	11
2.4 Transport in porous media.....	13
2.5 Numerical simulation principles.....	16
2.5.1 The electrochemical problem to solve .....	16
2.5.2 The finite element method .....	20
2.6 Current calculation in COMSOL.....	26
2.6.1 Calculation of faradaic current at a microelectrode.....	26
2.7 Modeling approaches of porous materials.....	31
2.7.1 Example of homogenization approach.....	32
2.7.2 Structural characteristics of nanoporous gold (NPG) .....	37
2.7.3 Deriving pore structure models from experimental images.....	41
2.8 Simulation of the heterogenous material .....	43
<b>3. Heterogeneous model of SI-SECM on cavity filled electrodes.....</b>	<b>48</b>
3.1 Cavity microelectrodes .....	48
3.2 Description of the research problem.....	49
3.3 Experimental details covered in the simulation.....	50
3.4 Experimental data .....	50
3.5 Porous substrate and description of surface reaction.....	53
3.6 Simulation description and results.....	58
3.6.1 Domain equations and boundary conditions.....	58
3.7 Conclusions .....	65
<b>4. Homogeneous model of passive porous substrates.....</b>	<b>66</b>
4.1 Description of the research problem and the experimental data.....	66

## Introduction

4.2 Theory.....	68
4.3 Simulation description and results.....	70
4.3.1 Domain equations and boundary conditions.....	72
4.3.2 Sensitivity to the angle $\alpha$ between the microelectrode plane and the sidewall of the insulating sheath of the microelectrode .....	73
4.3.3 Determination of porosity .....	77
4.3.4 Determination of layer thickness .....	80
4.3.5 Determination of porosity and film thickness simultaneously.....	82
4.3.6 Influence of skin layer.....	83
4.4 Conclusions .....	85
<b>5. Current density distribution on Li electrodes combined with an SECM probe .....</b>	<b>88</b>
5.1 Theoretical background.....	89
5.1.1 Solid electrolyte interphase.....	89
5.1.2 Current density distributions.....	91
5.2 Simulation description and results.....	92
5.2.1 Domain equations and boundary conditions.....	93
<b>6. Summary and Outlook .....</b>	<b>102</b>
<b>7. Appendix .....</b>	<b>104</b>
7.1 Parameters, variables, and equations used in Chapter 3.....	104
7.2 Parameters, variables, and equations used in Chapter 4.....	107
7.3 MATLAB script used in Chapter 4 .....	109
7.4 Parameters, variables, and equations used in Chapter 5.....	110
7.5 Abbreviations.....	112
7.6 Symbols .....	113
<b>8. References .....</b>	<b>115</b>
<b>9. Own publications and conference contributions .....</b>	<b>125</b>
9.1 Publications .....	125
9.2 Conference contributions.....	125
<b>10. Curriculum Vitae.....</b>	<b>126</b>

## 1. Introduction

There is a growing demand for high-performance electrochemical systems in energy storage, catalysis and sensing as they are able to link chemical and electrical conversion processes and thus might serve as key vectors between energy carriers.<sup>[1,2]</sup> Many of these processes are sluggish, this limitation can be mitigated by employing porous electrodes to increase the surface area available for the reaction. Nanoporous gold electrodes and lithium metal electrodes represent two examples for this strategy where the unique structural and electrochemical properties allow a quantitative assessment of the different influencing factors. To optimize these materials for practical applications, it is crucial to understand transport phenomena like ion diffusion, current distribution, and surface reactions, all of which are influenced by the microstructure of the electrodes.

Scanning electrochemical microscopy (SECM) has become a valuable tool for studying these processes at the microscale.<sup>[3]</sup> SECM allows for localized electrochemical measurements, giving insights into spatial variations in reactivity, mass transport, and surface properties.<sup>[3]</sup> However, interpreting SECM data for complex structures such as nanoporous electrodes requires accurate models that can describe the physical and electrochemical processes involved. This thesis tackles these challenges by developing and validating analytical models using finite element method (FEM) simulations, with a special focus on the transport properties of porous electrodes and lithium batteries.

Chapter 2 provides the theoretical background, introducing the basic principles of SECM and FEM simulations. These fundamentals are key to understanding the models and simulations presented in later chapters. Concepts such as mass transport and interfacial reactions are covered, which are critical for describing how SECM experiments measure the electrochemical behavior of materials. The chapter also explains SECM operation modes, such as feedback mode (FB) and surface interrogation mode (SI-SECM), setting the stage for the modeling work that follows.

Chapter 3 addresses the heterogeneous model of SI-SECM applied to cavity-filled electrodes, focusing on the interaction between redox mediators and metal oxides adsorbed on porous electrode surfaces, such as nanoporous gold (NPG) and platinum supported on carbon (Pt/C). The chapter models how surface reactions and porous structures affect feedback currents, with a particular focus on the impact of different oxide species on the electrochemical response. Using FEM simulations, the porous structure is represented in a way that amplifies the surface area, demonstrating how the electrode's extended conductive surface enhances the titration process during SECM experiments.

The study also explores variations in feedback behavior due to multiple oxide layers, providing insights into their influence on electrochemical measurements.

Chapter 4 presents a homogeneous model for passive porous electrodes, aimed at simplifying the description of transport properties while ensuring accuracy. This chapter introduces an updated analytical equation to model SECM approach curves on passive porous substrates, focusing on key parameters like porosity and film thickness. Numerical simulations are used to refine the model, with corrections for porosity and diffusion. The chapter also evaluates the presence of a skin layer and its role in influencing the transport properties of porous materials, while addressing the challenge of fitting porosity and film thickness simultaneously.

Chapter 5 looks at lithium electrodes, focusing on the solid electrolyte interphase (SEI), a critical component in determining the performance and safety of lithium batteries. This chapter explores how the SECM probe affects the current density distribution during lithium dissolution and deposition. Simulations of current densities highlight the need to carefully position the SECM probe to ensure accurate measurements and a better understanding of how current is distributed in the system.

Finally, Chapter 6 summarizes the main findings of the thesis, highlighting the benefits of combining SECM with FEM simulations to study transport phenomena in nanoporous electrodes and lithium batteries. The chapter also discusses potential future research directions, showing how the developed models and methods could help optimize the design of high-performance electrochemical systems.

By linking experimental SECM data with FEM simulations, this thesis provides a detailed understanding of how transport phenomena influence the performance of porous electrodes and lithium batteries. The models developed not only validate existing theories but also offer new insights into the mechanisms that drive electrochemical behavior, providing valuable tools for improving the design of these systems.

## 2. Modelling of electrochemical processes

Most electrochemical processes require coupling the electrical, chemical and transport phenomena which take place in an electrochemical cell. This usually means in the simplest case building a system of transport equations for species in solution coupled with heterogenous reaction equations describing the electron transfer which takes place at the surface of the electrodes. Most of the equations are expressed in terms of concentration dynamics, that is, the concentration of one or more species as a function of time. There is a very large amount of texts which cover in much greater detail the fundamentals of the processes described in this chapter such the classic electrochemistry book from Bard and Faulkner.<sup>[4]</sup>

### 2.1 Mass transport

Mass transport of chemical species in solution can be described by the Nernst-Planck Eq. (1) for the flux  $J$  of species  $i$ , in which the three terms describe the diffusion, the migration and the convection respectively. However, all simulations carried out in this work focus on the transport of species by diffusion only.

$$J_i = -D_i \nabla c_i - \frac{z_i F}{RT} D_i \nabla \phi + c_i v \quad (1)$$

$J_i$  is the molar flux per unit area of species  $i$  at the given point in space,  $D_i$  is the diffusion coefficient of species  $i$ ,  $c_i$  is the concentration,  $z_i$  the charge number,  $F$  the Faraday constant,  $R$  the universal gas constant,  $T$  the temperature,  $\phi$  is the potential and  $v$  the fluid velocity. The operator  $\nabla$  is the spatial derivative.

The first term on the right-hand side of Eq. (1) corresponds to Fick's first law of diffusion. It says that the net flux of solute crossing an area perpendicular to the flux direction is proportional to the negative of the concentration gradient at the plane. Most treated systems contained sufficient supporting electrolyte in the solution thus most of the ionic current was conducted by the supporting electrolyte. There was no mechanical stirring nor forced convection ( $v = 0$ ) and thus the third term could be neglected.

Fick's second law of diffusion describes the change of concentration of the species  $i$  with respect to time and is derived from Eq. (1) with the use of the continuity equation Eq. (2) which states that, in absence of homogenous reactions, a change in mass (related to concentration here) in any part of a

system is due to inflow and outflow of material into and out of that part of the system. It states that no material is created nor destroyed.

$$\frac{\partial c_i}{\partial t} + \nabla \cdot J_i = 0 \quad (2)$$

## 2.2 Interfacial reactions

The electrochemical reactions which take place at the surface of the electrodes in an electrochemical cell (heterogeneous reactions) are often determined by the kinetics of electron transfer between electrode and the electroactive species in solution. The net reaction rate  $r$  in Eq. (3) of an electrochemical reaction is proportional to the electrical current flowing through the electrochemical cell.

$$r = \frac{i}{nFA} \quad (3)$$

Here  $i$  is the current,  $n$  the number of electrons and  $A$  the surface area of the electrode. In order to have an accurate description of the kinetics present in any dynamic process it is imperative that the kinetics agree with the thermodynamic description of the model at equilibrium. For electrode reactions, the thermodynamic equilibrium is characterized by the Nernst equation, which describes the electrode potential with respect to the bulk concentrations of the electroactive species in solution. The standard potential ( $E^0$ ) is defined for conditions where all species are in their standard states (1 bar, 1 mol L<sup>-1</sup>, 298.15 K) and the corresponding Nernst equation is expressed in terms of the activities of the oxidized and reduced species. Since activity coefficients are rarely known with precision, it is more convenient in practice to work with concentrations. To account for the deviation from ideal behavior, the formal potential ( $E^{0'}$ ) is used, which incorporates activity effects and other medium-specific influences.

For the general case of a reduction reaction [Eq. (4)] at the electrode in which a species O is reduced to R.



The corresponding Nernst equation [Eq. (5)] describes the electric potential at the electrode as a function of the concentration of the oxidized ( $c_o$ ) and reduced species ( $c_R$ ).

$$E = E^{0'} + \frac{RT}{nF} \ln \frac{c_o}{c_R} \quad (5)$$

In the general case, the relation links the electrode potential to the ratio of the surface concentrations of the redox couple. When the bulk concentrations are used in Eq. (5), the expression yields the equilibrium potential ( $E_{eq}$ ), which is the potential at which the forward and backward reaction rates are equal, and the net current is zero.

Assuming first order kinetics for the reaction in Eq. (4), the forward reaction rate  $r_f$  is obtained from the rate constant  $k_f$  by Eq. (6):

$$r_f = k_f c_o = \frac{i_c}{nFA} \quad (6)$$

The forward reaction is a reduction and therefore a cathodic reaction with the rate being proportional to the cathodic current  $i_c$ , the backward reaction  $i_a$  is an oxidation which rate is proportional to the anodic current in Eq. (7):

$$r_b = k_b c_R = \frac{i_a}{zFA} \quad (7)$$

The net reaction is obtained from Eq. (8).

$$r_{net} = r_f - r_b = k_f c_o - k_b c_R = \frac{i}{zFA} \quad (8)$$

With the total cell current according to Eq. (9).

$$i = i_a - i_c = zFA(k_f c_o - k_b c_R) \quad (9)$$

The electrochemical rate constants have a particular property, they vary with the applied electrode potential, and it does so in the form of Eq. (10).

$$k_f = k^0 e^{-\alpha \frac{zF}{RT}(E-E_{eq})} \quad k_b = k^0 e^{(1-\alpha) \frac{zF}{RT}(E-E_{eq})} \quad (10)$$

Where  $(E-E_{eq})$  is the overpotential, which is the deviation of the electrode potential from the equilibrium value. In practice, it is often convenient to replace the equilibrium potential  $E_{eq}$  by the formal potential  $E^{0'}$ , which represents the equilibrium potential under standard or reference

conditions, where activities of oxidized and reduced species are equal. The overpotential ( $E-E^0$ ) then expresses the deviation of the applied potential from this reference value. The transfer coefficient  $\alpha$  lies between 0 and 1 for simple electron transfer reactions and serves as a measure of the symmetry of the activation energy barrier needed for the cathodic and anodic reactions to occur. The standard heterogeneous rate constant  $k^0$ , characterizes the intrinsic speed of the electron-transfer process at the electrode interface under equilibrium conditions, so that the rates of the forward and backward reactions are equal and no net current flows. All this results in the Butler-Volmer equation which is regarded as the fundamental equation of electrode kinetics:

$$i = F A k^0 \left( c_{\text{O}} e^{-\alpha \frac{zF}{RT}(E-E^0)} - c_{\text{R}} e^{(1-\alpha) \frac{zF}{RT}(E-E^0)} \right) \quad (11)$$

### 2.3 Scanning electrochemical microscopy

All simulations carried out in this work refer to measurements using scanning electrochemical microscopy (SECM), an electrochemical characterization method developed by Royce Engstrom in 1986<sup>[5]</sup> and popularized by Allen Bard in 1989.<sup>[6]</sup> SECM uses a microelectrode (ME), often called ultramicroelectrodes in the literature, as scanning probe to measure the current generated by an electrochemical reaction at its active disk-shaped area. In SECM experiments, the ME is positioned close to the sample surface, and the electrochemical response is monitored as the electrode is scanned over the surface. By mapping the local electrochemical activity, SECM provides valuable information about surface reactions, corrosion, catalysis, and other electrochemical processes with high spatial resolution. It has applications in various fields, including material science, biochemistry, and electroanalytical chemistry.<sup>[7-18]</sup>

The SECM apparatus consists of a bipotentiostat which controls the potential at the ME probe and in many cases, it also controls the potential of the sample, often called substrate, which is connected as a second working electrode. The distance between the ME and the substrate is set by micro-positioners, ensuring a very precise and consistent positioning. As in most electrochemical cells, the SECM system is completed by a reference electrode and an auxiliary electrode. In a SECM experiment, the ME and substrate are immersed in a solution containing a supporting electrolyte and a redox-active species called mediator, which can enter into multiple oxidation-reduction cycles at the ME and substrate, thereby sustaining a steady-state current that enables quantitative analysis of

local reactivity. The two operation modes of SECM studied in this thesis are the feedback mode (FB) and the surface interrogation mode (SI-SECM).

### 2.3.1 Microelectrodes

Microelectrodes (MEs) can be combined with conventional electrochemical experiments like voltammetry and chronoamperometry, broadening the applicability and research possibilities of electrochemical methods.<sup>[19]</sup> They also enable experiments without supporting electrolyte<sup>[20]</sup> and the analysis of electroactive species in gas mixtures.<sup>[21]</sup> In the context of this work, MEs play a particular critical role as the core component in SECM, where they enable spatially resolved measurements of electrochemical processes at the micro- and nanoscale. MEs have radii ranging from a few nanometers to 25  $\mu\text{m}$  and consist of a wire made of the electrode material (often Pt) sealed in glass and polished to form a disc ME. The glass serves as an insulator and is usually beveled, allowing the ME to be positioned very close to the substrate without the surrounding insulator touching its surface. A simplified SECM scheme demonstrating the ME without a substrate is shown in Figure 1. Usually, at the beginning of an SECM experiment only one form of a redox mediator is present in the solution. As an example, let us consider only the reduced form R of the mediator is present in the electrolyte. By applying a potential positive of the equilibrium potential, an oxidation takes place at the ME,  $R \rightarrow O + ne$  which produces a current flow between the ME and the auxiliary electrode, set far away from the ME to avoid any interference with the measurement. At the auxiliary electrode, a reduction reaction occurs as a counter-reaction to the reduction happening at the working electrode. The counter-reaction at the auxiliary electrode is in most cases not of interest.

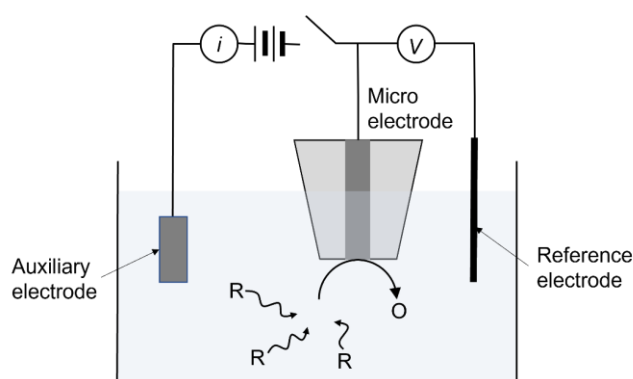


Figure 1. Scheme of a microelectrode in a simplified SECM setup.

Typical current vs. potential plots, known as voltammograms, of the described oxidation reaction using a ME and a regular disk-shaped electrode are compared in Figure 2 where no substrate is

present, simulating an infinite distance. In the case of the voltammogram using a ME (Figure 2a), an S-shape curve is produced, with a steep slope in the region where the electrochemical reaction rate limits the current measured before reaching its limit value where the current is controlled by the steady-state diffusion of the mediator to the ME.

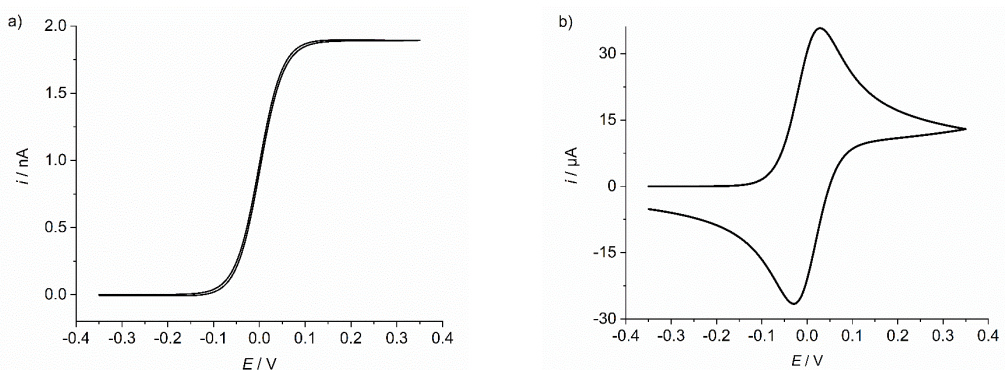


Figure 2. Simulated voltammograms for a) a ME with  $r_T = 5 \mu\text{m}$  and b) a regular electrode with  $r_T = 5 \text{mm}$  at a scan rate of  $5 \text{mV/s}$ , and a redox mediator concentration of  $1 \text{mM}$ .

The hemispherical diffusion present in disk-shaped MEs allows for the establishment of the steady-state diffusion-limited current in much shorter timescales than that of macroscopic electrodes and has the value according to Eq. (12) when the ME is surrounded by an insulating glass sheath<sup>[22]</sup> at a distance from the substrate large enough to be considered infinite:

$$i_{T,\infty} = gnFDc^*r_T \quad (12)$$

Here  $g$  is a factor that depends on the geometry of the insulating glass sheath (4 for infinite large insulators). The short time, in which the current reaches its steady-state, means that the current value remains practically unperturbed by convective effects, which presents the advantage that the scanning probe can be moved in the solution and still be treated as a steady-state system. Also, as the currents recorded are in the order of nA, the ohmic drop associated with the current is also negligible<sup>[23]</sup> in most cases as opposed to experiments carried out with regular electrodes.

The simulated voltammogram obtained in the same electrolyte at a larger electrode under otherwise identical conditions is shown in Figure 2b. The much larger surface of the electrode and, consequently, a larger number of reacting species in the vicinity of the electrode, generates a planar diffusion and concentration gradient which impedes the system to quickly reach steady-state conditions resulting in a typical macroscopic voltammogram.

### 2.3.2 Working principle of feedback mode

The feedback mode (FB) is used to obtain kinetic or reactivity information of a substrate to be probed by the ME. Its general principles are illustrated in Figure 3, considering the initial presence of only the reduced form R of the mediator. The hemispherical diffusion of the mediator which produces the steady-state diffusion-limited current described by Eq. (12) is shown Figure 3a. As the ME approaches an electrically insulating substrate, such as glass, the current decreases due to the hindered diffusion of the mediator to the ME (Figure 3b), this corresponds to the negative feedback mode. However, when the substrate is electrochemically active, enabling the regeneration of the mediator at its surface, the measured current increases as the ME approaches it (Figure 3c). Even if the mediator diffusion from the bulk solution is hindered, the substrate serves as a reagent source for the tip reaction which leads to much larger currents than those predicted by Eq. (12). There are three ways in which the mediator can be regenerated:<sup>[3]</sup> electrochemical conversion at the substrate, wherein the oxidized form of the mediator is converted back to R as in Figure 3c, an (enzyme-)catalyzed reaction which consumes R and regenerates O, and local reduction of the sample material by R (etching).<sup>[24]</sup>

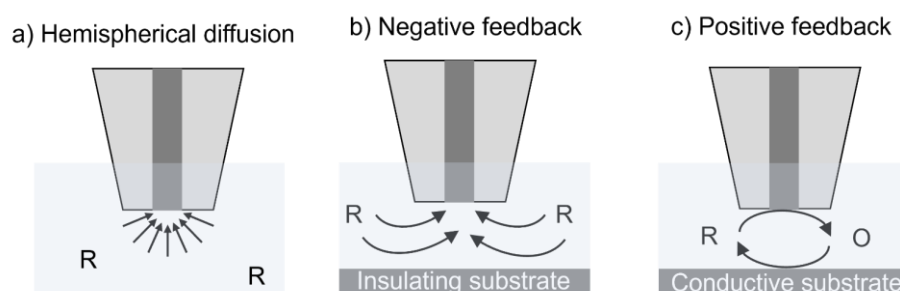


Figure 3. Illustration of the basic SECM principles. When the ME is positioned; a) far from the substrate, a steady state current is observed; b) near to an insulating substrate, leading to a negative feedback current; c) near to a conductive substrate, positive feedback current arises.

The electroactive surface being probed does not need to be connected to a potentiostat to generate the feedback current. If the substrate is sufficiently larger than the ME, a concentration cell is formed at its surface (Figure 4).<sup>[25]</sup>

If an oxidation  $R \rightarrow O + ne$  occurs at the ME while the bulk solution contains only R, and the ME approaches a large unbiased conductive substrate such as gold, it leads to the observation of a positive feedback current as the open circuit potential of the entire substrate surface is dictated by the Nernst Eq. (5). Hence, when only R is present in the bulk solution of the redox couple R / O, the potential of

the conductive substrate is negative of the formal potential and O generated at the ME is reduced at the sample resulting in a positive feedback current.<sup>[25,26]</sup>

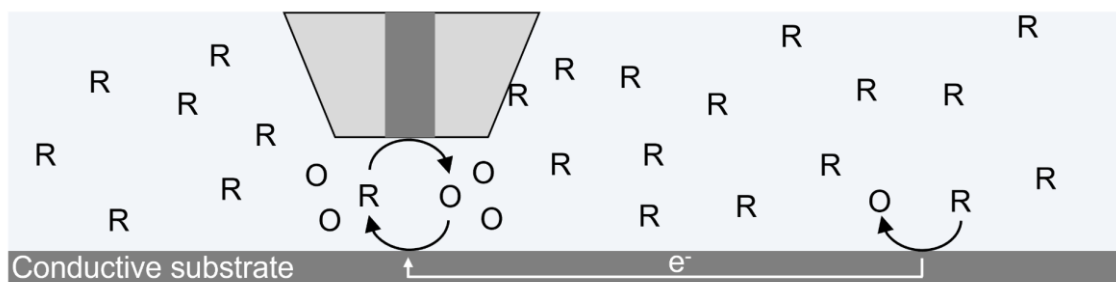


Figure 4. Positive feedback current due to lateral electron transfer caused by the formation of a concentration cell on an unbiased conductive substrate.

The plot of the ME current  $i_T$  vs. the distance  $d$  is known as an approach curve (Figure 5). The limiting cases of the positive feedback and negative feedback correspond to curves 4a and 4g respectively. It is common to present the plot in dimensionless form by plotting  $I_T = i_T/i_{T,\infty}$  (the measured current  $i_T$  divided by the current at infinite distance  $i_{T,\infty}$  from the substrate) vs.  $L = d/r_T$  (the distance  $d$  between the ME and the substrate divided by the radius of the ME  $r_T$ ). By presenting the plot in dimensionless form, the plotted curves do not depend on the concentration of the mediator or its diffusion coefficient.

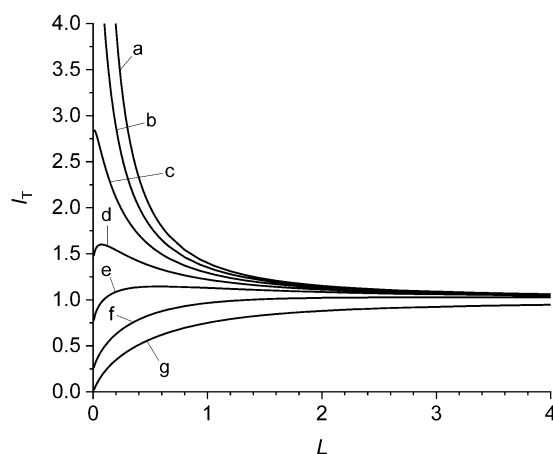


Figure 5. Simulated approach curves illustrating various feedback conditions based on the dimensionless rate constant  $\kappa$ : a) positive feedback with  $\kappa = \infty$ ; b)  $\kappa = 10$ ; c)  $\kappa = 4$ ; d)  $\kappa = 2$ ; e)  $\kappa = 1$ ; f)  $\kappa = 0.3$ , g) hindered diffusion with  $\kappa = 0$ .

The current is influenced by the ratio  $R_g$  between the radii of the glass sheath to the ME, denoted  $r_g$ , and the active electrode  $r_T$ . The effect of  $R_g$  is stronger for the negative FB case, as the glass sheath also blocks diffusion of the redox species. In many practical scenarios, this effect has minimal

influence if  $\kappa$  is sufficiently large. When considering the regeneration reaction at the substrate, the limiting cases for the heterogeneous rate constant would be  $k_s \rightarrow 0$  in the case of an insulator (hindered diffusion) and  $k_s \rightarrow \infty$  for a conductor. For intermediate values of  $k_s$  approach curves can be used to get valuable information on the rate of heterogeneous charge transfer at the sample electrode. If the ME radius and the diffusion coefficient of the mediator are known and assuming a first-order heterogeneous rate constant  $k_s$ , then the heterogeneous rate constant in dimensionless form  $\kappa$  is defined in Eq. (13).

$$\kappa = \frac{k_s r_T}{D} \quad (13)$$

In FB mode SECM experiments, simulations play a crucial role in analyzing reaction kinetics and diffusion characteristics at electrode surfaces. By generating theoretical approach curves that represent the current response as the ME approaches the substrate, simulations enable the evaluation of electron transfer processes and diffusion dynamics.<sup>[27–29]</sup> Adjusting parameters such as the heterogeneous rate constant, diffusion coefficient, and ME radius enables the extraction of kinetic data, which are often difficult to measure directly. Simulations apply boundary conditions that reflect the presence of conductive or insulating substrates, distinguishing between positive and negative feedback to characterize different electron transfer rates. Testing hypotheses regarding surface reactivity and mediator behavior, simulations illustrate the effects of various parameters on feedback currents and aid in interpreting experimental data. This approach validates experimental findings and offers a comprehensive understanding of kinetics and diffusion near active surfaces, enhancing SECM's utility in probing surface electrochemistry.<sup>[3,25]</sup> This approach will be demonstrated in Chapter 3, where SECM simulations are employed to analyze feedback currents at nanoporous gold and Pt-supported carbon cavity microelectrodes, providing quantitative insight into their electron transfer kinetics and mass transport properties.

### 2.3.3 Surface interrogation mode

SECM can also be used as a powerful method to study adsorbed reaction intermediates in-situ. This technique is known as the surface interrogation mode of SECM (SI-SECM) and operates similarly to the FB mode.<sup>[30–35]</sup> The main difference is that it is mostly applied under transient conditions which allows to obtain quantitative information of the adsorbed species at the substrate. This information is provided by comparing the measured current and the hindered diffusion current, which serves as the baseline. The surface under investigation is, instead of the usually quasi-infinite substrate used in classic SECM experiments, a second ME of around the same size as the interrogator ME. A potential

can be applied to both electrodes which allows an adsorbate to be electrochemically generated at the substrate which is then titrated by the mediator produced at the interrogator ME (Figure 6). This produces a transient feedback current as long as adsorbate A is available. When the adsorbed species are depleted, the current decays to its value for hindered diffusion. The distance separating both MEs should be  $L \leq 0.3$  to obtain a large collection efficiency,<sup>[36]</sup> which is defined as the ratio of the amount of species generated at the substrate and the amount collected at the interrogator ME. Under these conditions, a transient feedback current is observed as long as adsorbate A is available. When the adsorbed species are depleted, the current decays to its value for hindered diffusion.

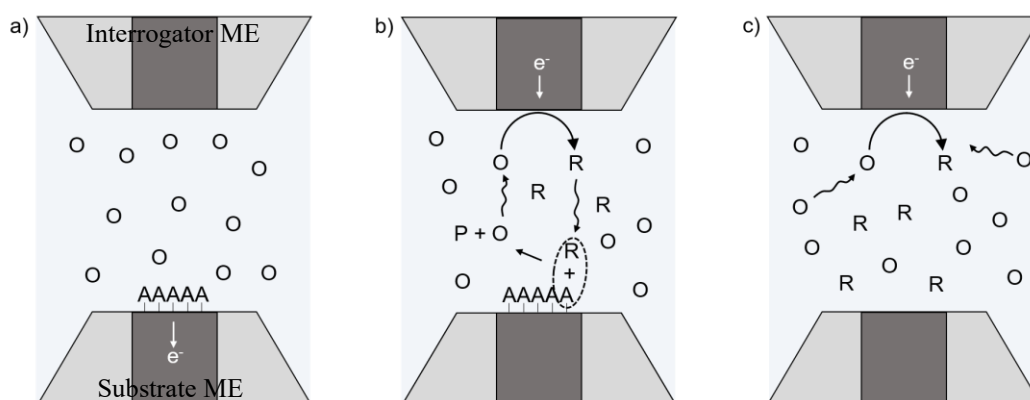


Figure 6. Surface interrogation mode of SECM (SI-SECM). a) Metal oxides (A) are electrochemically formed at the substrate ME. b) O is reduced to R at the tip of the ME which reacts with A at the substrate regenerating O and producing a positive feedback current. c) When A has completely reacted, a hindered diffusion current is registered at the interrogator ME.

The kinetic constants of the chemical reaction between the adsorbed species and the mediator can also be evaluated depending on the shape of the current plot. For faster kinetics, the current registered would be higher and decay after a shorter time provided constant amounts of A are compared. A simulation of a cyclic voltammogram (CV) showing an SI-SECM experiment is shown in Figure 7. Curve 6a corresponds to the negative feedback current and 6e to the positive feedback. Curve 6b shows the current profile of an SI-SECM simulation with a surface concentration  $\Gamma$  of A and reaction rate for the adsorbates and mediator of  $k_{SI}$  in  $A + R \rightarrow B + O$ , while curve 6c shows a simulation with a starting surface concentration of  $\Gamma$  and reaction rate of  $10k_{SI}$ . Curve 6d has a starting surface concentration of  $3.5\Gamma$  and a reaction rate of  $10k_{SI}$ . It is evident that the slope is dependent on the reaction rate and the amount titrated is related to the integral of the current curve.

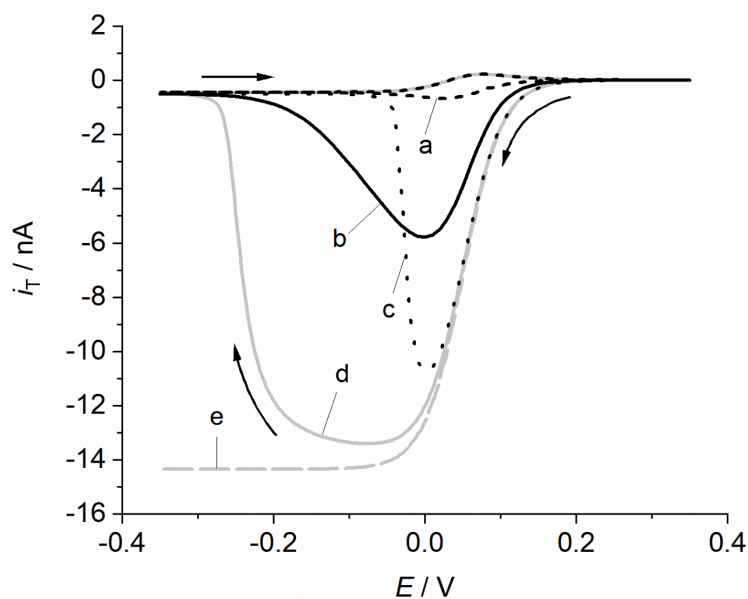


Figure 7. Simulated SI-SECM curves. During the forward scan in a cyclic voltammogram CV the adsorbates are titrated by the redox mediator leading to a feedback current. This feedback current is influenced by the quantity and reaction rate of the reaction between adsorbate and mediator. Curves *b*, *c* and *d* represent different reaction rates and quantities of adsorbates, with curve *b* showing a moderate feedback response due to a lower adsorbate concentration and slower reaction rate, curve *c* depicts a stronger feedback response resulting from a larger reaction rate while keeping the same adsorbate concentration of curve *b*. Curve *d* depicts a stronger feedback response resulting from a higher concentration and larger reaction rate. Curve *a* represents the hindered diffusion feedback (no adsorbate present), while curve *e* illustrates the positive feedback current limit.

Simulations of SI-SECM experiments can aid to evaluate more accurately the kinetic characteristics of the system under investigation, even if the reaction mechanisms are not fully understood.<sup>[33,37,38]</sup> The technique has been effectively utilized in transient current experiments, such as chronoamperometry<sup>[27,34,39–41]</sup> and cyclic voltammetry<sup>[42–44]</sup> to study a wide variety of surfaces ranging from metal catalysts like gold and platinum<sup>[45]</sup> to bacteria biofilms.<sup>[46]</sup>

## 2.4 Transport in porous media

The exploration of porous materials and porous electrodes has become of great importance because of its dominance in industrial applications. The main characteristic of porous materials is the intimate contact between the solid material and the solution due to their extensive surface area to volume ratio. The most common definition of the term pore is a space or cavity in a continuous solid material<sup>[47,48]</sup> in which the porosity ( $P$ ) of a medium can be calculated as the fraction of void volume ( $V_V$ ) and total volume ( $V_T$ ).

$$P = \frac{V_v}{V_T} \quad (14)$$

In porous electrodes, the solid matrix consist of a single reactive electronic conductor or a mixture consisting of nonconductive, reactive materials in addition to electronic conductors.<sup>[49]</sup>

There are several ways of treating porosity in simulations of reaction transport problems, and most of them can be categorized into two approaches, depending on the scale of the problem: the microscopic and the macroscopic approach. In the microscopic approach, the geometry, phases, and structure of the porous network are studied in detail. Description of electrochemical and transport processes based on first principles is only possible at the microscopic level (pores usually being smaller than 200 nm) which makes it computationally impossible to solve for scales usually important in electrochemical experiments as they typically involve systems with length scales of at least 50  $\mu\text{m}$ .<sup>[50]</sup> To overcome this limitation, macroscopic models are developed which aim to represent the microscopic properties by using effective transport coefficients and source terms in homogenized partial differential equations.<sup>[47,51]</sup>

The general equation for homogenous diffusive transport in a porous medium in terms of concentration is given by Eq. (15).

$$P \frac{\partial c_i}{\partial t} + \nabla \cdot (-D_{\text{eff}} \nabla c_i) = 0 \quad (15)$$

Here  $D_{\text{eff}}$  is the effective diffusion coefficient of the homogenized porous phase and its proper estimation has been the focus of a very large number of ongoing studies for over a century.<sup>[52,53]</sup>

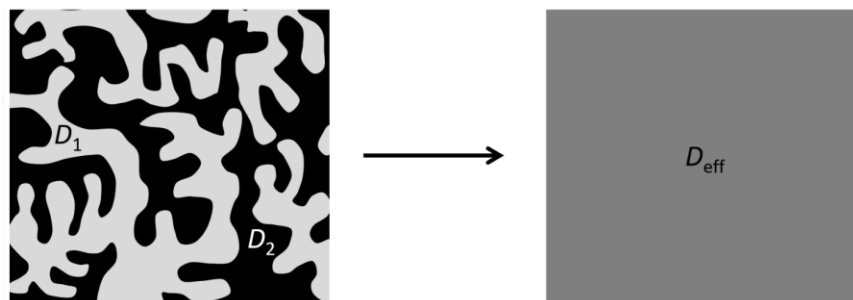


Figure 8. Microscopic features of a porous structure with two phases (left),  $D_1$  and  $D_2$  are the diffusion coefficients for each of the phases,  $D_2 = 0 \text{ m}^2 \text{ s}^{-1}$  in case of solid. Homogenized porous medium with effective macroscopic diffusion coefficient  $D_{\text{eff}}$  valid on the whole domain (right).

In this work all porous domains consisted exclusively of two phases, one liquid phase filling completely the void volume and one solid matrix. A very commonly used method to relate  $D_{\text{eff}}$  and the normal fluid diffusion coefficient  $D$  is given by Eq (16).<sup>[54]</sup>

$$D_{\text{eff}} = D \frac{P}{\tau} \quad (16)$$

Equation (16) introduces the tortuosity factor  $\tau$ , used to describe the sinuosity and interconnectedness of the pore domain. The way to quantify and even understand tortuosity is a matter of debate to this day as there is no universal definition. It is employed in different ways by engineers, chemists and geologists to describe the slower transport of, in most cases, fluids through porous structures.<sup>[54,55]</sup> Electrical tortuosity typically relies on conductivity for its definition, while hydraulic tortuosity is conventionally characterized by geometric parameters. On the other hand, diffusional tortuosity is commonly determined based on the dynamic changes in concentration over time. A more promising approach could involve defining tortuosity by considering the underlying material or electrical current flux in relation to the forces propelling this flow.

In the context of unsteady transport processes, including diffusion, an array of tortuosities emerges, each corresponding to the various pathways followed by particles as they traverse the medium. However, when dealing with measurements under steady flow conditions like those utilized to assess resistivity or permeability, crucial information regarding particle travel times is lost, resulting in the homogenization of tortuosity values. Figure 9 shows several different ways of defining the tortuosity.

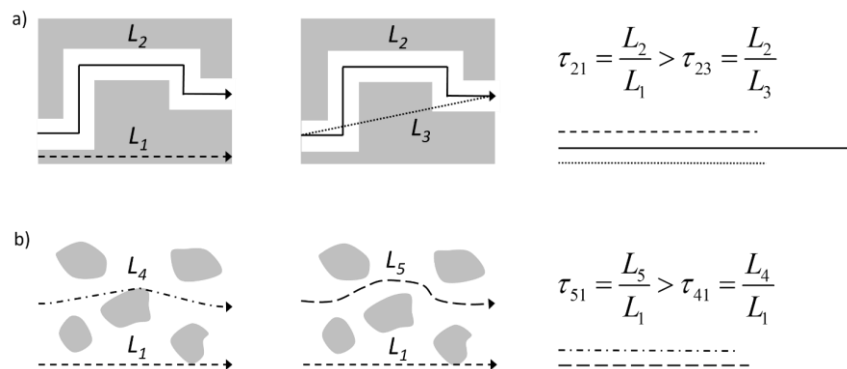


Figure 9. Comparison of two different methods for calculating  $\tau$  based on geometry are shown in a). Difference of geometric and hydraulic tortuosity is observed in b).

One way to define it geometrically, is the ratio of the shortest path between two connected points and the straight line projected in the direction of the flow ( $\tau_{21}$ ). Another more commonly used method of defining the tortuosity geometrically is the shortest path of two connected points divided by the

straight distance between them ( $\tau_{23}$ ). Tortuosity can also be defined hydraulically,<sup>[56]</sup> which is based in Darcy's law of flow and considers the effective path length taken by the fluid ( $\tau_{51}$ ) rather than the shortest possible path ( $\tau_{41}$ ).

When treating systems in which molecular diffusion in solution is the only transport phenomenon present, fitting the tortuosity factor as described in Eq. (16) seems the more convenient approach as porosity is a well-defined physical property and usually much easier to determine experimentally. Tortuosity, aside from having different meanings, is also used as a factor to account for many processes related to the size and shape of the porous structure which are also difficult to quantify and cannot be related to the porosity, such as molecules colliding with pore walls and their sticking factors.

## **2.5 Numerical simulation principles**

Numerical analysis has seen remarkable advancements over the past half-century, driven largely by the exponential growth of information technology, which has provided unprecedented computational power. Numerical analysis steps in when traditional mathematical methods are impractical for industrial applications, offering tailored approximation techniques to solve complex problems.<sup>[57]</sup> This field is essential for approximating solutions to equations with partial derivatives, a common foundation in modeling real-world systems.<sup>[57]</sup> Applications span diverse domains such as physics, mechanics, finance, and economics, where the translation of complex phenomena frequently leads to partial differential equations. A range of methods, including finite element, finite volume, and spectral methods, have been developed to tackle these equations, with the finite element method (FEM) standing out due to its flexibility in modeling complex geometries and widespread use in engineering and applied sciences.<sup>[57]</sup> Nowadays, FEM is accessible to end-users through user-friendly software packages such as COMSOL which require no programming knowledge.

### **2.5.1 The electrochemical problem to solve**

Modelling electrochemical processes almost always attempts to tackle the complexities of solving transport phenomena of electrochemical species. The analytical solutions for these transport equations are often very challenging or even impossible, except for a few idealized cases. Fortunately, the more complicated problems which closely represent reality are solvable through numerical simulations on computers.

In 1964, Feldberg and Auerbach<sup>[58]</sup> were among the first to develop a numerical model to simulate electrode processes. Over the years, the field of numerical analysis saw remarkable progress, particularly after 1980, when personal computers became widely accessible. Initially, the finite difference method was preferred in electrochemistry.<sup>[59,60]</sup> The FEM was first applied in electrochemistry by Penczek and Stojek in 1984.<sup>[61,62]</sup> However, in comparison to simpler methods like that of the finite differences, FEM was considered more complex and time-consuming in one-dimensional systems, leading to limited adoption. It was not until 1994, when Nann and Heinze proposed its specific use for addressing electrochemical and SECM problems, that FEM gained widespread popularity in this field.<sup>[63]</sup> The application of FEM becomes very powerful particularly when dealing with systems that require more than one spatial dimension, as it is the case for SECM problems which require at least two dimensions. Another unique advantage of FEM is that it can naturally account for edge effects arising from the micrometric dimensions of the electrodes.<sup>[64]</sup>

The notation used in this section follows the conventions established by Nann and Heinze in their seminal work on electrochemical simulations using FEM.<sup>[63]</sup> Bold symbols denote matrices, while arrows indicate vector quantities. This notation is applied to clearly distinguish scalar quantities from multi-dimensional entities, particularly in systems involving multiple interacting species. Additionally, a dot above a variable indicates the time derivatives of the variables in the context of dynamic changes. By adopting this established methodology, clarity is maintained in representing the complexities of diffusion and reaction processes within the framework of finite element modeling. As previously stated, diffusional mass transport serves as the foundation for most electrochemical simulation programs. Fick's second law [Eq. (2)] can be generalized by writing the concentration  $c$  in a vector formulation as

$$\vec{c} = \vec{c}(t, \vec{x}) \quad \forall \vec{x} \in \Omega \quad (17)$$

In this notation,  $\Omega$  is a bounded open region within an  $n$ -dimensional space that has a continuously smooth boundary. The concentration vector is assumed to be a function of both time and position. Each component of the concentration vector corresponds to the concentration of a different chemical species, allowing for the simultaneous description of multiple species in a system. This formulation is particularly useful in diffusion models, where the concentration of each species changes over time and varies across spatial coordinates.

$$\begin{pmatrix} c_A \\ c_B \\ \vdots \\ c_N \end{pmatrix} = \begin{pmatrix} c_A(t, \bar{x}) \\ c_B(t, \bar{x}) \\ \vdots \\ c_N(t, \bar{x}) \end{pmatrix} \quad (18)$$

Thus, using this notation, Eq. (2) becomes

$$\dot{\vec{c}} = \mathbf{D}\nabla^2\vec{c} \quad (19)$$

With  $\mathbf{D}$  as a diagonal matrix, containing the diffusion coefficients.

$$\mathbf{D} = \begin{pmatrix} D_A & 0 & \cdots & 0 \\ 0 & D_B & \cdots & 0 \\ \vdots & \vdots & \ddots & \vdots \\ 0 & 0 & \cdots & D_N \end{pmatrix} \quad (20)$$

The long form of the right side of Eq. (19) is

$$\nabla^2\vec{c} = (\nabla^2\vec{c}_A, \nabla^2\vec{c}_B, \dots, \nabla^2\vec{c}_N)^T \quad (21)$$

In this vector formulation, interaction between different species has not yet been considered. In Eq. (19) a reaction term can be added to consider homogenous chemical reactions. A reaction matrix  $\mathbf{k}$  is defined so that the product of the reaction matrix and the concentration vector gives the first-order chemical reaction rates.

$$\begin{pmatrix} \dot{\vec{c}}_A \\ \dot{\vec{c}}_B \\ \vdots \\ \dot{\vec{c}}_N \end{pmatrix} = \begin{pmatrix} k_{11} & k_{12} & \cdots & k_{1N} \\ k_{21} & k_{22} & \cdots & k_{2N} \\ \vdots & \vdots & \ddots & \vdots \\ k_{N1} & 0 & \cdots & k_{NN} \end{pmatrix} \cdot \begin{pmatrix} c_A \\ c_B \\ \vdots \\ c_N \end{pmatrix} \quad (22)$$

Eq. (19) now becomes

$$\dot{\vec{c}} = \mathbf{D}\nabla^2\vec{c} + \mathbf{k}\vec{c} \quad (23)$$

Second-order reactions result in nonlinear systems. These systems are solved iteratively by applying the Banach fixed point theorem according to  $\vec{c}_{n+1} = f(\vec{c}_n)$ , where

$$f(\vec{c}) = \mathbf{D}\nabla^2\vec{c} + \mathbf{k}\vec{c} \quad \forall \vec{x} \in \Omega \quad (24)$$

$\vec{c}_n$  represents the concentration vector at the current iteration ( $n$ ),  $f(\vec{c}_n)$  is a function that calculates the updated concentration based on the previous values,  $\vec{c}_{n+1}$  is the updated concentration vector for the next iteration.

For a second-order reaction



Results in matrix  $\mathbf{k}$ .

$$\mathbf{k} = \begin{pmatrix} -\frac{1}{2}k_f c_B & -\frac{1}{2}k_f c_A & \frac{1}{2}k_b c_D & \frac{1}{2}k_b c_C \\ -\frac{1}{2}k_f c_B & -\frac{1}{2}k_f c_A & \frac{1}{2}k_b c_D & \frac{1}{2}k_b c_C \\ \frac{1}{2}k_f c_B & \frac{1}{2}k_f c_A & -\frac{1}{2}k_b c_D & -\frac{1}{2}k_b c_C \\ \frac{1}{2}k_f c_B & \frac{1}{2}k_f c_A & -\frac{1}{2}k_b c_D & -\frac{1}{2}k_b c_C \end{pmatrix} \quad (26)$$

In the case of more complex simulations not considered in this work, convection and migration terms can be incorporated by adding the appropriate terms.

In the next step, electrochemical initial and boundary conditions must be introduced.

There are three types of boundary conditions present in electrochemistry problems. The first is the Dirichlet boundary condition.

$$\vec{c}(t, \vec{x}) = \vec{c}^* \quad \forall \vec{x} \in \partial\Omega_D \quad (27)$$

The Dirichlet boundary condition, often referred to as a semi-infinite boundary, specifies that the concentration vector  $\vec{c}(t, \vec{x})$  is constant at a known value  $\vec{c}^*$  for all  $t$  and  $\vec{x}$  within the Dirichlet domain  $\Omega_D$ . In electrochemical systems, this Dirichlet domain can represent a region where concentration is controlled or fixed, such as the outer boundary of the simulation domain. For example, this boundary condition might reflect the starting concentration of the mediator in solution, which is held constant in the solution bulk, ensuring stable conditions at large distance from the ME throughout the simulation.

The second type of boundary condition is the Neumann boundary condition, where the flux at the boundary is specified. This condition is typically applied to inert walls or symmetry axes, where no flux is present.

$$\nabla_n \vec{c}(t, \vec{x}) = 0 \quad \forall \vec{x} \in \partial\Omega_N \quad (28)$$

where  $\nabla_n \vec{c} = 0$  indicates that the normal component of the concentration gradient at the boundary element  $\partial\Omega_N$  is zero, ensuring no flux across these boundaries. Alternatively, for the semi-infinite limit, this condition can be selected instead of the Dirichlet boundary by fixing a known flux to define an electrode boundary. The last type of electrochemically interesting boundary is the Cauchy boundary, which combines aspects of both Dirichlet and Neumann boundary conditions. This condition appears when a heterogeneous charge transfer with Butler-Volmer kinetics is introduced. A new reaction matrix is defined called electrode matrix  $\mathbf{E}$ . It contains the rate constants of heterogeneous charge transfers by analogy to homogenous chemical reactions. In the case of a simple charge transfer



Where  $k_c$  and  $k_a$  are the forward (cathodic) and backward (anodic) rate constants of the heterogeneous charge transfer. The electrode matrix is given as

$$\mathbf{E} = \begin{pmatrix} -k_c & k_a \\ k_c & -k_a \end{pmatrix} \quad (30)$$

As the final formulation of this type of Cauchy boundary condition, one obtains:

$$\nabla_n \vec{c}(t, \vec{x}) = \mathbf{E} \vec{c}(t, \vec{x}) \quad \forall \vec{x} \in \partial\Omega_C \quad (31)$$

where  $\partial\Omega_C$  represents the specific boundary element where the Cauchy boundary condition is applied. In this case it specifically designates the boundary associated with the electrode surface, where the heterogeneous charge transfer reactions take place. This boundary condition thus reflects the electrochemical reaction kinetics at the electrode surface, linking the flux and concentration through the electrode matrix.

A generalized formulation of the electrochemically relevant equations is now available and can be used in the finite element method.

### 2.5.2 The finite element method

The finite element method is used to approximate the solution of the searched function  $u$  (for instance the concentration field) by using a sequential continuous polynomial function.

$$u = \sum_{j=0}^{N-1} c_j b_j \quad c_j \in \mathbb{R} \quad (32)$$

Where  $\{b_j\}_{j=0,\dots,N-1}$  are the basis functions of the finite element space and  $c_j$  are the corresponding coefficients that define the discrete solution. In our particular case, these coefficients represent the concentration at node  $j$ . The points where the  $c_j$  terms are defined are called nodes. Elements are arbitrary polyhedron constructed from various nodes. In the two-dimensional case, they are usually triangles.

To solve the generalized Eq. (23), time and space are separated in the approximation function.

$$u(t, \vec{x}) = \sum_{j=0}^{N-1} c_j(t) b_j(\vec{x}) \quad c_j(t), \vec{x} \in \mathbb{R} \quad (33)$$

The approximation function (33) is now inserted in Eq. (23) and the residual functions  $\mathbf{R}$ , are added.

$$\sum_{j=0}^{N-1} \dot{\vec{c}}_j(t) b_j(\vec{x}) = \mathbf{D} \sum_{j=0}^{N-1} \vec{c}_j(t) \nabla^2 b_j(\vec{x}) + \mathbf{k} \sum_{j=0}^{N-1} \vec{c}_j(t) b_j(\vec{x}) + \mathbf{R}(t, \vec{x}) \quad (34)$$

The residual functions can be moved by a variational formulation.

$$\sum_{j=0}^{N-1} \dot{\vec{c}}_j(t) \int_{\Omega} b_j b_i d\vec{x} = \mathbf{D} \sum_{j=0}^{N-1} \vec{c}_j \int_{\Omega} \nabla^2 b_j b_i d\vec{x} + \mathbf{k} \sum_{j=0}^{N-1} \vec{c}_j \int_{\Omega} b_j b_i d\vec{x} \quad (35)$$

$$i = 0, \dots, N-1$$

Green's first law is applied to the term with the second partial derivation.

$$\sum_{j=0}^{N-1} \dot{\vec{c}}_j(t) \int_{\Omega} b_j b_i d\vec{x} = \mathbf{D} \sum_{j=0}^{N-1} \vec{c}_j \left( - \int_{\Omega} \nabla b_j \nabla b_i d\vec{x} + \int_{\partial\Omega} \nabla_n b_j \nabla b_i d\vec{x} \right) + \mathbf{k} \sum_{j=0}^{N-1} \vec{c}_j \int_{\Omega} b_j b_i d\vec{x} \quad (36)$$

$$i = 0, \dots, N-1$$

At this point, the boundary integrals can be disregarded as the boundary conditions are integrated after the assembly of the equation system. Following certain rearrangements, the ensuing function is derived in Eq. (37).

$$\sum_{j=0}^{N-1} \dot{\vec{c}}_j \int_{\Omega} b_j b_i d\vec{x} + \sum_{j=0}^{N-1} \vec{c}_j \left( \mathbf{D} \int_{\Omega} \nabla b_j \nabla b_i d\vec{x} - \mathbf{k} \vec{c}_j \int_{\Omega} b_j b_i d\vec{x} \right) = 0 \quad (37)$$

$$i = 0, \dots, N-1$$

Equation (37) represents a system of equations, which can be written as

$$\mathbf{M} \dot{\vec{c}} + \mathbf{S} \vec{c} = 0 \quad (38)$$

here the matrices are defined as

$$\mathbf{M} = (m_{ji}), \quad m_{ji} = \int_{\Omega} b_j b_i d\bar{x} \quad (39)$$

$$\mathbf{S} = (s_{ji}), \quad s_{ji} = \mathbf{D} \int_{\Omega} \nabla b_j \nabla b_i d\bar{x} - \mathbf{k} \int_{\Omega} b_j b_i d\bar{x} \quad (40)$$

and

$$\vec{c} = \left[ (c_{A0}, c_{B0}, \dots, c_{n0}), \dots, (c_{A(N-1)}, c_{B(N-1)}, \dots, c_{n(N-1)}) \right]^T \quad (41)$$

Matrix  $\mathbf{M}$  is called the mass matrix, matrix  $\mathbf{S}$  the stiffness matrix.

### **Basis functions**

Basis functions  $b_i$  are defined at every node of every individual element.

$$b_i(p_j) = \delta_{ij} \quad (42)$$

With  $p_j$  as nodes of the element and  $\delta_{ij}$  the Kronecker delta which equals 1 at its own node ( $i$ ) and 0 at all other nodes. Linear and quadratic polynomials are used as basis functions.

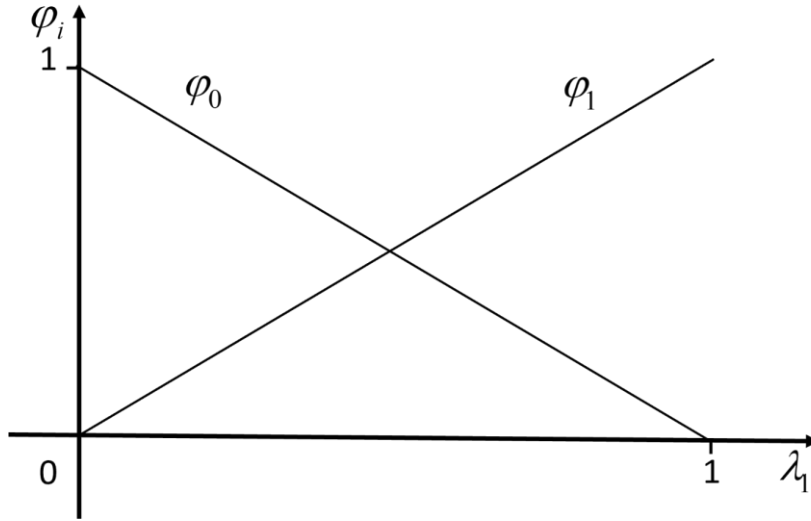


Figure 10. Linear basis functions  $\varphi_i(\vec{x}) = \lambda_i(\vec{x})$  with  $\lambda_i$  as barycentric coordinates for a one-dimensional element.

Figure 10 shows linear basis functions on a one-dimensional element while Figure 11 shows a quadratic one. In principle, basis functions of arbitrary orders can be constructed by choosing polynomials which obey Eq. (42), but it is advantageous to choose them so that only nodes which are direct neighbors contribute to the resulting matrices in Eq. (39) and (40).

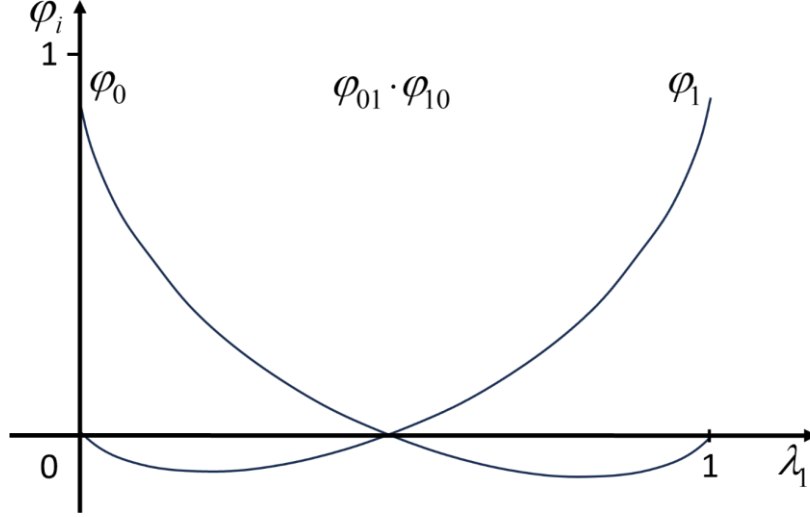


Figure 11. Quadratic basis functions  $\varphi_i(\vec{x}) = \lambda_i(\vec{x})(2\lambda_i(\vec{x}) - 1)$  and  $\varphi_j(\vec{x}) = 4\lambda_i(\vec{x})\lambda_j(\vec{x})$  for a one-dimensional element.

### Time discretization

To solve the system of equations in Eq. (38), a time discretization scheme is required. For this purpose, the  $\Theta$ -scheme is applied, which combines explicit and implicit time integration methods.

$$(1 - \Theta) \cdot \text{explicit} + \Theta \cdot \text{implicit}, \quad \Theta \in [0, 1] \quad (43)$$

Depending on the value of the parameter  $\Theta$ , the  $\Theta$ -scheme interpolates between a fully explicit method ( $\Theta = 0$ ) and a fully implicit method ( $\Theta = 1$ ). A value of  $\Theta = 0.5$  yields the ‘‘Crank–Nicolson’’ scheme, which is semi-implicit.<sup>[65]</sup>

$$\vec{c}^m := \vec{c}(m\Delta t, \vec{x}) \quad m = 0, \dots, t_{\text{tot}} / \Delta t \quad (44)$$

Equation (44) is the discretized solution of the concentration vector at a time step  $m$ . Applying the  $\Theta$ -scheme to Eq. (38) gives

$$(1 - \Theta) \left( \mathbf{M} \frac{\vec{c}^m - \vec{c}^{m-1}}{\Delta t} + \mathbf{S}^{m-1} \vec{c}^{m-1} \right) + \Theta \left( \mathbf{M} \frac{\vec{c}^m - \vec{c}^{m-1}}{\Delta t} + \mathbf{S}^m \vec{c}^m \right) = 0, \quad \Theta \in [0, 1] \quad (45)$$

The stiffness matrix is now time dependent as the Butler–Volmer equation is applied at every time step. By rearranging it in the form

$$\left( \frac{1}{\Delta t} \mathbf{M} + \Theta \mathbf{S}^m \right) \vec{c}^m = \left( \frac{1}{\Delta t} \mathbf{M} - (1 - \Theta) \mathbf{S}^{m-1} \right) \vec{c}^{m-1}, \quad \Theta \in [0, 1] \quad (46)$$

this equation system assumes the form

$$\mathbf{A}\vec{x} = \vec{b} \quad (47)$$

where

$$A = \frac{1}{\Delta t} \mathbf{M} + \Theta \mathbf{S}^m \quad (48)$$

and

$$\vec{b} = \left( \frac{1}{\Delta t} \mathbf{M} - (1 - \Theta) \mathbf{S}^{m-1} \right) \vec{c}^{m-1} \quad (49)$$

and

$$\vec{x} = \vec{c}^m. \quad (50)$$

The system in Eq. (47) is non-symmetric. It can be multiplied by  $\mathbf{A}^T$  to make it symmetrical such that relaxation solvers such as Gauss-Seidel can be used to solve the system. This approach can be beneficial for numerical stability and convergence in iterative solvers, particularly when dealing with large sparse systems.

### ***Space discretization***

The adaptability of the algorithm enables a macro-level discretization of the region  $\Omega$ , which can subsequently be refined. The geometry of the elements depends on the dimensionality of the problem. For one-dimensional problems, the region is composed of linear segments. A two-dimensional region is divided into triangles, while in three-dimensional problems, tetrahedrons are used. Regions of particular interest can undergo local refinement, as seen, for instance, in the region surrounding the electrode (Figure 14).

The general algorithm of the adaptive strategy follows the sequence:

1. The solution on the given grid is calculated.
2. The error on each element is estimated.
3. The elements requiring refinement are identified.
4. The discretization is adapted, and the algorithm restarted at (1).

The fundamental concept underlying the error estimation in point 2 involves computing the gradient of the solution within each element and comparing it with the gradients of neighboring elements. If the disparity surpasses a specific predetermined threshold, both elements are designated for

refinement using a bisection approach. In essence, the bisection technique entails dividing a triangle into two smaller triangles by connecting one vertex with the midpoint of the opposing edge. The cumulative simulation error is determined by aggregating the errors across individual elements.

Usually when using commercial FEM software, space discretization is initially handled automatically, and refinement is applied by selecting the regions or boundaries of interest and imposing element size conditions.

In SECM simulations, where electrode diameters often measure less than 50  $\mu\text{m}$  and act as probes for quantifying heterogeneous electrochemical reactions, accurate computation of the current is essential. Since the current is directly tied to these heterogeneous processes, its precise evaluation is critical.

COMSOL has been the most widely used commercial software for simulating SECM experiments for over a decade, as evidenced by the large number of scientific publications that rely on it for numerical simulations.<sup>[66–78]</sup> Nevertheless, several internal variables can be used to calculate the electrode current. These include domain-based variables and boundary-based variables. Mathematically, both approaches are equivalent because they are derived from the same diffusion equations. Consequently, one would expect them to yield identical electrode current values. However, the author noticed discrepancies when comparing different model definitions in COMSOL which are mathematically equivalent.

For example, in a study by the Bard group on the electrochemical oxidation of N,N-dimethylaniline (DMA), SECM was employed to detect the short-lived radical cation intermediate  $\text{DMA}\cdot^+$ .<sup>[78]</sup> Because of the extremely small electrode dimensions (2  $\mu\text{m}$  ME, 5  $\mu\text{m}$  substrate) and the need to quantify very low currents associated with transient intermediates, the accuracy of the current calculation is of central importance. In this case, the COMSOL report in the supporting information reveals that a domain-based variable was used in COMSOL to evaluate the ME current. In contrast in another study from the Rodriguez-Lopez group employed boundary flux variables in their COMSOL simulations of SECM with mercury-capped MEs for lithium ion quantification in nonaqueous media<sup>[77]</sup> as evidenced by their full model available in the supporting information.

These examples underscore that even in highly precise SECM studies, the choice of internal COMSOL variables is non-trivial and is rarely, if ever, specified in the main article. Verification is only possible when the full model is provided as supporting information, which remains uncommon. This omission is understandable, as the underlying equations are mathematically correct and, in

theory, expected to yield equivalent results. Nevertheless, even specialized articles on COMSOL simulations in electrochemistry omit this issue entirely.<sup>[70]</sup>

Therefore, it was necessary to conduct a study to determine the most accurate and robust method for calculating the electrode current among the various approaches reported in the literature. For this purpose, the well-established Cottrell experiment was chosen as a benchmark case.

## 2.6 Current calculation in COMSOL

### 2.6.1 Calculation of faradaic current at a microelectrode

COMSOL offers a plethora of ways to create and define simulations, from predefined packages that often provide a straightforward approach to simulate various model cases to completely self-defined equation systems.

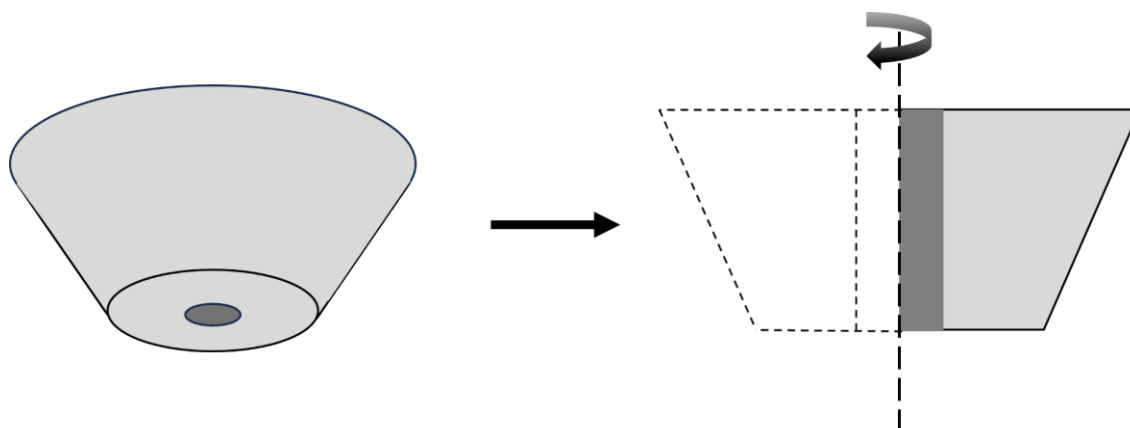


Figure 12. ME simulation geometry scheme, the 3D ME is commonly modeled in a two-dimensional cylindrical axisymmetric geometry to simulate SECM experiments.

A two-dimensional cylindrical axisymmetric geometry (no dependence on the azimuthal angle) is the natural choice when simulating typical SECM experiments in COMSOL. Most scientific studies<sup>[30,78,79]</sup> explicitly define the current, as shown in Eq. (51) rather than relying on the predefined COMSOL variables. These predefined variables are available only in specific modules designed for electrochemical simulations, which are often restrictive in their design and lack flexibility for custom applications. This approach necessitates transforming the general time-dependent diffusion equation Eq. (2) into cylindrical axisymmetric coordinates<sup>[80]</sup> and multiplying the result by the Faraday constant to calculate the current at the microelectrode (ME) tip as:

$$i_T = 2\pi nFD \int_{r=0}^{r=r_T} \frac{\partial c}{\partial z} r dr \quad (51)$$

The key variable for defining the electrode current is the normal flux of the reacting chemical species at the electrode surface. In COMSOL, this flux can be represented using either domain variables or boundary variables, depending on the context of the simulation.

Domain variables, such as the concentration gradient, are defined throughout the entire simulation space. This allows them to be evaluated at any point within the domain, whether at a specific location, on a boundary, or over an area in two-dimensional simulations. This flexibility makes domain variables particularly useful for analyzing fluxes or concentrations across the entire geometry. For instance, the normal flux of a species can be calculated using the concentration gradient ( $\partial c/\partial z$ ) and the diffusion coefficient  $D$ , as expressed in Eq. (51).

On the other hand, boundary variables are restricted to specific boundaries and are used to directly evaluate fluxes or other properties at these explicitly defined locations. While boundary variables are limited in scope, they are well-suited for boundary-specific calculations, such as evaluating the flux at the electrode surface. Table 1 lists the internal variable names in COMSOL for both domain and boundary representations of the normal flux for the concentration  $c$  of the studied species. Since diffusion is the only mechanism of transport in this thesis, these internal variables theoretically provide all equivalent quantities and are often utilized in scientific publications to calculate the electrode current.

Table 1: Internal domain variable names used in COMSOL to calculate the normal flux for the reacting species with concentration  $C$  at the electrode surface boundary.

Domain Variables		
Name	Description	Expression
D*Cz	Diffusion coefficient $\times$ Concentration gradient, z component	$D \int_{r=0}^{r=r_T} \frac{\partial c}{\partial z} r dr$
dflux_Cz	Total flux, z component	
dfluxMag_C	Diffusive flux magnitude	
tfluxMag_C	Total flux magnitude	

These variables align closely with the explicit definition of current in Eq. (51), where the normal flux is calculated based on the concentration gradient in the  $z$ -direction ( $\partial c/\partial z$ ) and multiplied by the diffusion coefficient  $D$  and the Faraday constant.

Table 2. Internal boundary variable names used in COMSOL to calculate the normal flux for the reacting species with concentration  $C$  at the electrode surface boundary.

Boundary Variables		
Name	Description	Expression
ndflux_C	Normal diffusive flux	$D \int_{r=0}^{r=r_1} \frac{\partial c}{\partial z} r dr$
ntflux_C	Normal total flux	
bndFlux_C	Boundary flux	

To test the accuracy of the variables listed in Table 1 and These variables align closely with the explicit definition of current in Eq. (51), where the normal flux is calculated based on the concentration gradient in the  $z$ -direction ( $\partial c/\partial z$ ) and multiplied by the diffusion coefficient  $D$  and the Faraday constant.

Table 2, a transient simulation describing the classic Cottrell experiment<sup>[81]</sup> was performed.

This experiment involves a planar electrode and describes the time-dependent current response under diffusion-controlled conditions, serving as a foundational method in electrochemistry to study diffusion kinetics and the transport of electroactive species toward the electrode surface. The simulation results were compared to the most accurate analytical equation available to date, shown in Eq. (52) proposed by Mahon et al,<sup>[82]</sup> which is applicable to microelectrodes and provides a more accurate analytical description of the transient current response. The Mahon equation accounts for radial diffusion effects and is particularly valid for very small time intervals ( $t \rightarrow 0$ ) at which the current changes most rapidly.

$$\Psi = \begin{cases} \frac{1}{\sqrt{\pi\theta}} + 1 + \sqrt{\frac{\theta}{4\pi}} - \frac{3\theta}{25} + \frac{3\theta^{\frac{3}{2}}}{25} & \theta \leq 1.281 \\ \frac{4}{\pi} + \frac{8}{\sqrt{\pi^5\theta}} + \frac{25\theta^{-\frac{3}{2}}}{2792} - \frac{\theta^{-\frac{5}{2}}}{3880} - \frac{\theta^{-\frac{7}{2}}}{4500} & \theta \geq 1.281 \end{cases} \quad (52)$$

With

$$\Psi = \frac{i}{n\pi F c^* D r_T^2} \quad \theta = \frac{Dt}{r_T^2}$$

Here  $\Psi$  is the dimensionless current,  $I$  the total current response,  $n$  the number of electrons transferred,  $F$  the Faraday's constant,  $r_T$  the microelectrode radius,  $c^*$  the bulk concentration of the studied species,  $D$  the diffusion coefficient, and  $t$  the time in seconds. Figure 13 shows the calculated current in dimensionless form using Eq. (52) and the simulated curves in COMSOL. All current calculations using the domain variables deliver exactly the same results. All boundary variables also deliver the exact same values. Looking at the logarithmic curve in Figure 13a, it is apparent that all three curves are very similar, converging at the  $\mu\text{s}$  scale. However, in Figure 13b, it is evident that the current calculated using domain variables deviates by around 5% at the 1-10 seconds time interval compared to the analytical equation and the current calculated using boundary variables.

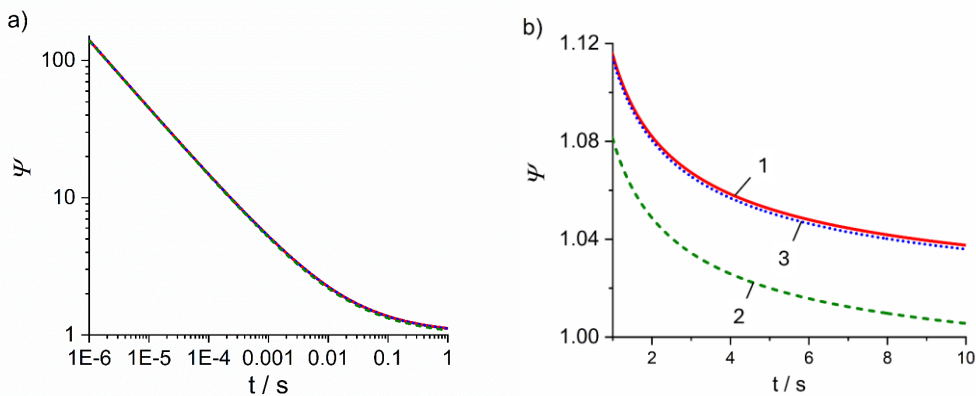


Figure 13. Comparison of the calculated current at an inlaid disc microelectrode using: 1) boundary variables (red straight line), 2) domain variables (green dash), 3) analytical approximation (blue dots); a) logarithmic time and logarithmic current values from  $t = 1 \times 10^{-6}$  s to 1 s; b) linear current vs. linear time between  $t = 1$  s to 10 s.

In addition to transient simulations, stationary simulations were also conducted to further compare the calculation of the dimensionless current. The results are displayed in Table 3. With the advance in computing power, meshing has become less of a limitation for FEM simulations, especially in two-dimensional geometries but remains a very important part in obtaining accurate results with the singularity point (edge between electrode and insulating material) being responsible for the largest source of error in FEM simulations concerning MEs.<sup>[83,84]</sup>

Table 3. Comparison between the calculated dimensionless simulated current values  $\Psi$  using boundary and domain variables, employing different maximum mesh element sizes at the electrode boundary and different element size at the singularity point between the electrode and insulating surface.  $ES$  and  $PS$  are dimensionless numbers used to scale the mesh elements.

max element size = $\frac{r_e}{ES}$	point size = $\frac{r_e}{PS}$	Boundary Variables	Domain Variables
$ES$	$PS$	$\Psi_B$	$\Psi_D$
10	10	1.0468	0.7119
10	100	1.0159	0.8968
10	1000	1.0128	0.9628
50	100	1.0156	0.9055
50	1000	1.0128	0.9667
100	100	1.0154	0.9086
100	1000	1.0127	0.9743
500	1000	1.0124	0.9795
1000	1000	1.0122	0.9797

A couple important aspects become clear by looking at Table 3. Boundary variables consistently provide more accurate and stable results across all mesh configurations. The values of  $\Psi_B$  calculated with boundary variables converge to a value near 1.012, with minimal variation as the mesh element ( $ES$ ) and singularity point refinement ( $PS$ ) improve. For instance, with a coarse mesh element ( $ES = 10$ ) and increasing singularity point refinement ( $PS = 10, 100, 1000$ ; line 1, line 2, line 3), the calculated values of  $\Psi_B$  steadily approach 1.0128. With a fine boundary mesh and singularity point refinement ( $ES = 1000$  and  $PS = 1000$ ; line 9), the value converges to 1.0122, indicating excellent accuracy with an error of less than 0.06 % when comparing  $ES = 100$  and  $PS = 1000$  (row 3 in Table 3) vs.  $ES = 1000$  and  $PS = 1000$  (row 9 in Table 3).

This stability demonstrates that boundary variables are less sensitive to mesh refinement, making them more reliable for simulations requiring high precision. The slight improvement in  $\Psi_B$  values with finer mesh configurations suggests that further refinement beyond  $ES = 1000$  may have diminishing returns for accuracy.

Domain variables exhibit much greater sensitivity to mesh refinement, with the calculated  $\Psi_D$  values varying widely for coarser configurations. For example, with  $ES = 10$  and  $PS = 10$ ,  $\Psi_D = 0.7119$ ,

which is significantly lower than the boundary variable result for the current of  $\Psi_B = 1.0468$ . However, as  $PS$  is refined to 1000, the domain variable result improves to  $\Psi_D = 0.9628$ , reducing the discrepancy but still falling short of the boundary variable value.

Even for finer boundary meshes like  $ES = 1000$ , domain variables do not fully converge to the same level of accuracy as boundary variables  $\Psi_D = 0.9797$  vs.  $\Psi_B = 1.0122$ . This sensitivity to the singularity point refinement highlights the importance of using highly refined meshes when employing domain variables. The poor convergence attained with the evaluated parameters suggests that domain variables may require significantly more computational effort to match the precision of boundary variables.

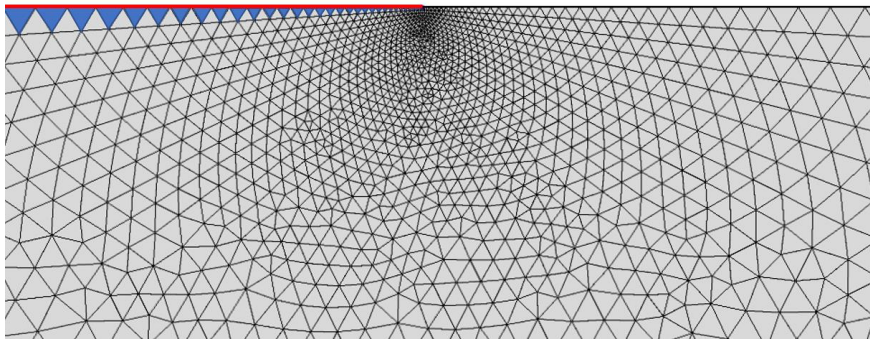


Figure 14. Mesh configuration around the singularity point between the electrode and the insulating surface in COMSOL. The electrode boundary is indicated by the red line, while the blue triangles highlight the domain elements that form the boundary. The parameter  $ES$  refers to the element size along the red boundary (electrode surface), and  $PS$  corresponds to the element size around the singularity point, located where the red boundary terminates on the right side.

Figure 14 displays the mesh around the singularity point, with the focus on the electrode boundary (shown as a red line) and the mesh elements that interact with this boundary. The inaccuracies observed with domain variables appear to arise from the way COMSOL performs its calculations internally. When a domain variable is used to evaluate a boundary, the computation of the fluxes seems to involve integrating over the mesh elements that are in contact with the boundary, rather than directly considering the boundary itself. As a result, to obtain precise flux calculations, it is essential to use boundary variables.

## 2.7 Modeling approaches of porous materials

As already mentioned, there are various approaches available to deal with porous media. Macroscopic homogeneous models of porous structures aim to capture as accurately as possible the intricacies of the microscopic heterogeneous structures. The grand challenge consists in identifying the

relationships that bridge various length scales and integrating them into a single equation system.<sup>[85]</sup> Rigorous mathematical approaches have been developed for this purpose, broadly referred to as heterogeneous multi-scale methods or simply multi-scale methods (MSM).

MSM brought a lot of progress in combining the field of mechanics of materials and that of materials science, mainly due to the successful combination of micromechanics and mathematical approaches with a steadily increasing multi-disciplinary character. The main advantage comes from successfully translating the accuracy of the microscopic models coupled with the efficiency and simplicity of the macroscopic models. From a perspective of numerical methods, multi-scale ideas have been long employed such as in multi-grid or mesh refinements in FEM, however these are in reality general purpose microscale solvers, as is evidently seen in the high-quality meshing needed at the microelectrode and the coarse meshing used to simulate the bulk electrolyte. The objective of MSM is to capture the macroscale behavior of the system with a significantly lower computational cost compared to solving a full microscale problem.<sup>[86,87]</sup>

### 2.7.1 Example of homogenization approach

As a general example to introduce how MSM can be applied, consider the classical one-dimensional diffusion problem, which is also discussed in Hornung's *Homogenization and Porous Media* as a standard case for illustrating homogenization techniques.<sup>[86]</sup>

$$-\nabla \cdot (D(x)\nabla c(x)) = 0 \quad \text{for } 0 < x < 1 \quad (53)$$

with boundary conditions

$$c(0) = 0, \quad c(1) = 1$$

on a smooth domain defined in the unit interval  $\Omega = [0,1]$ . Three possible cases are considered here for  $D$ , which corresponds to the diffusion coefficient in the diffusion equation and is a smooth, strictly positive function for the general case.

- 1) When  $D$  is a smooth function with no small-scale features.
- 2) When  $D$  has multiple scales and the scales are so different that they can be separated,  $D$  is written as  $D^\varepsilon$  where  $\varepsilon$  denotes the small scales.
- 3) When  $D$  has small scales which do not have any special features.

The first case is the simplest problem, while the third case presents the most challenging to solve. However, the way to handle these two extreme cases is very similar. It involves efficient fine scale

solvers such as multi-grid and adaptive mesh. Even in the third case, due to the nonuniform nature of the problem, the approach is to treat it as a very complicated problem that requires a detailed solution. Modern MSM are designed to handle problems of the second case, where solutions to a large-scale problem are obtained at a much lower cost than running full fine-scale simulations.

MSM has been already applied in electrochemical systems, particularly in porous electrodes.<sup>[88]</sup> In such models, macroscopic porous electrodes feature a microscale internal porous structure. A pore-scale model based on Fick's diffusion and Butler-Volmer reaction kinetics. This microscopic model was then upscaled using volume-averaging techniques to derive an effective macroscopic model that incorporates the key features of the electrode's microstructure. The macroscopic model effectively captured the influence of microstructural parameters, such as porosity and specific surface area, on diffusion and reaction kinetics, while significantly reducing computational costs compared to direct numerical simulations. The validity of the macroscopic model was confirmed by its agreement with numerical simulations and experimental data, showing its potential for bridging microscale phenomena with macroscale performance.

Homogenization is a subgroup of MSM and is commonly used to solve the second case mentioned above. It has been used to solve highly complex reaction-diffusion systems in porous systems such as corrosion of concrete.<sup>[89]</sup>

The differential equation (53) implies that the flux is defined as  $J(x) = -D(x)\nabla c(x)$  where  $D(x)$  is the local diffusion coefficient and  $c(x)$  is the local concentration of the electroactive species. Under steady-state conditions, the total flux remains constant across the domain  $\Omega$  (as the second derivative is zero), meaning

$$J = -D(x)\frac{dc(x)}{dx} = \text{constant}. \quad (54)$$

This constant flux can be expressed as  $J^*$  leading to

$$\frac{dc(x)}{dx} = -\frac{J^*}{D(x)}. \quad (55)$$

Integrating and applying boundary conditions  $c(0) = 0$  and  $c(1) = 1$  from Eq. (53) yields

$$1 = 0 - J^* \int_0^1 \frac{d\tilde{x}}{D(\tilde{x})},$$

And after solving for  $J^*$

$$J^* = -\frac{1}{\int_0^1 \frac{d\tilde{x}}{D(\tilde{x})}},$$

where the effective diffusion coefficient is defined by Eq (56).

$$\frac{1}{D^*} = \int_0^1 \frac{d\tilde{x}}{D(\tilde{x})} \quad (56)$$

Consequently, the effective (or average) diffusion coefficient  $D^*$  characterizing transport across the material is determined. Given that a unit concentration gradient was imposed in the domain  $\Omega$ , the effective transport equation, expressed in terms of the homogenized flux, diffusion coefficient, and concentration, simplifies to

$$J = -D^* \frac{dc^*(x)}{dx} = J^*. \quad (57)$$

This shows the essential features of homogenization, if the function  $D(x)$  describes diffusivity or another spatially varying property like, conductivity, or permeability in a porous medium, then the homogenized value  $D^*$  is the effective parameter that characterizes the transport across the porous domain.

To account for the small-scale structure of the material, a scale parameter  $\varepsilon = 1/n$  is introduced, where  $n$  represents the number of small-scale features (e.g. pores) within the domain. This parameter enables the separation of macroscopic (slow) and microscopic (fast) scales. Accordingly, the diffusion coefficient  $D(x)$  is rescaled to depend on the small-scale variable  $y = x/\varepsilon$  [Eq. (58)].

$$D^\varepsilon(x) = D(y) = D(x/\varepsilon) \text{ for } 0 < x < 1 \quad (58)$$

Homogenization assumes the microstructure is periodic, so that

$$D(y+1) = D(y) \text{ for all } y. \quad (59)$$

The original diffusion equation is rescaled to

$$-\frac{d}{dx} \left( D \left( \frac{x}{\varepsilon} \right) \frac{dc^\varepsilon}{dx} \right) = 0 \text{ for } 0 < x < 1. \quad (60)$$

The boundary conditions remain  $c^\varepsilon(0) = 0$  and  $c^\varepsilon(1) = 1$ .

To solve the multiscale behavior of  $c^\varepsilon(x)$  an asymptotic expansion is used to decouple macro- and microscales:

$$c^\varepsilon(x) = c_0(x) + \varepsilon c_1(y) + \varepsilon^2 c_2(y) + \dots, \text{ for } 0 < x < 1 \quad (61)$$

Where  $c_0(x)$  is the macroscopic concentration profile and  $c_1(y)$ ,  $c_2(y)$  are microscopic corrections due to pore-scale variations. The scale parameter  $\varepsilon \ll 1$  separates macro- and microscales. Higher-order terms ( $\varepsilon^2, \dots$ ) become negligible as  $\varepsilon \rightarrow 0$ . The expansion is then substituted into the modified diffusion equation

$$-\frac{d}{dx} \left( D^\varepsilon(x) \frac{dc^\varepsilon}{dx} \right) = 0 \quad (62)$$

applying the chain rule with respect to the fast and slow variables

$$-\frac{1}{\varepsilon} \frac{d}{dy} \left( D(y) \left[ \frac{1}{\varepsilon} \frac{dc_0}{dx} + \frac{dc_1}{dy} + \varepsilon \frac{dc_2}{dy} + \dots \right] \right) = 0 \quad (63)$$

Inserting the expansion into the equation and grouping terms by powers of  $\varepsilon$ , the leading-order term  $\mathcal{O}(1/\varepsilon^2)$  gives

$$-\frac{d}{dy} \left( D(y) \frac{dc_0}{dx} \right) = 0. \quad (64)$$

Since  $\frac{dc_0}{dx}$  is constant with respect to  $y$ , this implies

$$\frac{dc_0}{dx} = \text{constant}, \quad (65)$$

so that

$$c_0(x) = J^* x + C. \quad (66)$$

Applying boundary conditions  $c^\varepsilon(0) = 0$  and  $c^\varepsilon(1) = 1$  implies  $C = 0$ , so  $c_0(x) = J^* x$ .

Order  $\mathcal{O}(1/\varepsilon)$ :

$$-\frac{d}{dy} \left( D(y) \frac{dc_1}{dy} \right) = \frac{d}{dy} D(y) \quad (67)$$

This defines the so-called cell problem for  $c_1(y)$ , with periodic boundary conditions  $c_1(0) = c_1(1)$ . The cell problem is integrated over one period  $y \in [0, 1]$ :

$$-\int_0^1 \frac{d}{dy} \left( D(y) \frac{dc_1}{dy} \right) dy = \int_0^1 \frac{d}{dy} D(y) dy \quad (68)$$

Using periodicity ( $D(0) = D(1)$ ,  $c_1(0) = c_1(1)$ ), both integrals vanish. To resolve this, the average flux is used:

$$J^* = -D^* \frac{dc_0}{dx} = -\int_0^1 D(y) \left( \frac{dc_0}{dx} + \frac{dc_1}{dy} \right) dy \quad (69)$$

This formulation shows that the homogenized flux  $J^*$  combines the macroscopic gradient  $dc_0/dx$  with the microscale correction  $dc_1/dy$ . With a fixed periodic function  $D(x)$  having periodicity length 1. This means that the functions  $D(x)$  are oscillatory with increasing frequencies for  $\varepsilon \rightarrow 0$ , as can be seen in Figure 15a.

With  $(x/\varepsilon) = y$ , Eq. (69) can be rewritten as

$$c^\varepsilon(x) = c(x) + \varepsilon c_1(y) \quad (70)$$

Here  $c(x)$  is the macroscopic concentration profile and  $c_1$  is a 1-periodic function that captures the microscopic oscillations defined as

$$c_1(y) = \frac{\int_0^y \frac{dy}{D^\varepsilon(y)}}{\int_0^1 \frac{dy}{D(y)}} - y, \text{ for } 0 \leq y \leq 1. \quad (71)$$

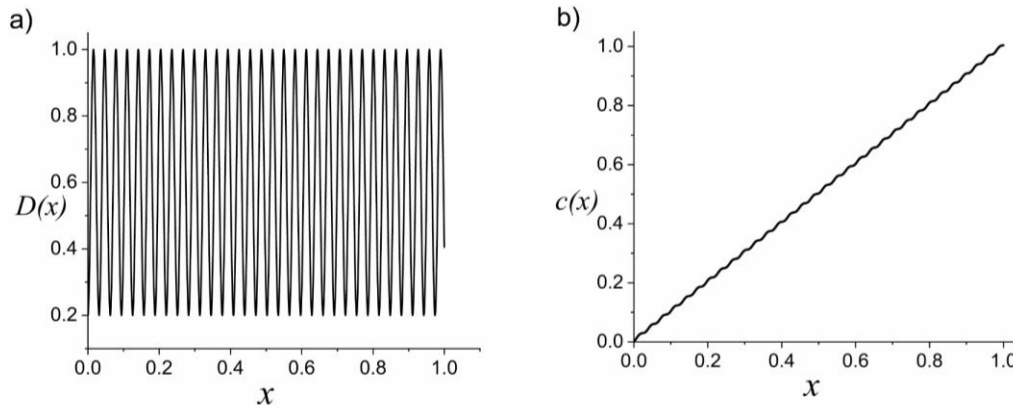


Figure 15. Oscillatory function  $D$  and global solution  $c(x)$  in the interval  $\Omega = [0,1]$ .

Consequently, pointwise convergence is assured. The function  $c(x)$  describes the global response of the function  $c^\varepsilon$ , while the function  $c_1(y)$  describes the local oscillations of  $c^\varepsilon$ , as seen in Figure 15b. This illustrates how the homogenization method handles the separation of scales. The scale parameter  $\varepsilon$  ideally represents the pore size within a porous medium, which is embedded into the global problem. By solving the problem when  $\varepsilon \rightarrow 0$ , the oscillatory behavior of the solution is removed. The variable  $x$  is normally referred to as the macroscopic (slow) variable, and  $y$  is known as the microscopic (fast) variable, both assumed to be independent. Formally, the technique used to solve the problem is the asymptotic expansion (sometimes called asymptotic homogenization) which is outside the scope of this work, but specialized literature on the subject can be consulted.<sup>[90–92]</sup>

### 2.7.2 Structural characteristics of nanoporous gold (NPG)

The renewed interest in gold catalysis traces its origins to the 1980s, marked by the initial discovery that nanosized gold clusters anchored on reducible metal oxides exhibit remarkable catalytic activity in the oxidation of carbon monoxide at low temperatures.<sup>[93,94]</sup> Independently, it was reported that atomic oxygen situated on the surface of single-crystal gold could be easily reduced by carbon monoxide, even at room temperature.<sup>[95]</sup>

The adsorption characteristics and reactivity of gold were summarized in terms of their size dependence, ranging from bulk to smaller particles, clusters, and individual atoms.<sup>[96]</sup> The catalytic performance of gold was found to be significantly influenced by factors such as dispersion,<sup>[97]</sup> support materials,<sup>[97,98]</sup> and the methods used for its preparation.<sup>[97,98]</sup> For cases where gold was deposited onto specific metal oxides in the form of hemispherical ultra-fine particles with diameters smaller than 5 nm,<sup>[97,99]</sup> remarkably high levels of activity and/or selectivity in various chemical processes were reported.<sup>[97,99,100]</sup> These processes included the combustion of carbon monoxide and saturated hydrocarbons,<sup>[96,101]</sup> the oxidation-decomposition of amines and organic halogenated compounds,<sup>[102,103]</sup> the partial oxidation of hydrocarbons, the hydrogenation of carbon oxides, unsaturated carbonyl compounds, alkynes, as well as the reduction of nitrogen oxides.<sup>[99]</sup>

Nanostructuring stands as one of the most effective methodologies for crafting materials endowed with novel or enhanced chemical attributes. Catalysis, a pivotal technology within the chemical industry,<sup>[104]</sup> plays a role in approximately 80-90% of all industrial processes.<sup>[105]</sup> It is intricately tied to the ongoing endeavor to diminish our energy consumption and carbon dioxide (CO<sub>2</sub>) emissions. In the realm of heterogeneous catalysis, nanostructuring has been employed from early on, as evidenced by the substantial portion of heterogeneous catalysts comprised of nanostructured materials.<sup>[94,105,106]</sup>

Within this context, heterogeneous gold catalysts serve as an exemplary illustration of the emergence of fresh chemical functionalities through nanostructuring.<sup>[105]</sup>

The term “nanoporous” was apparently coined by Kelly et al.<sup>[107]</sup> in a study of an Au/Ag alloy used to produce a dealloyed layer of nanometer-scale porosity referred to as nanoporous gold (NPG). The pores in NPG are mesopores according to the International Union of Pure and Applied Chemistry (IUPAC) classification, which classifies porous materials into microporous (pore size < 2 nm), mesoporous (2 nm < pore size < 50 nm) and macroporous (pore size > 50 nm) materials.<sup>[108]</sup> In light of the IUPAC definition, the term *nanoporous* is without any formal meaning.<sup>[109]</sup> However, it is widely accepted and extensively used in scientific literature.<sup>[110–115]</sup> and this thesis will follow this general use.

NPG was reported in recent years to have high activity for low-temperature CO and methanol oxidation,<sup>[93,116–118]</sup> and has also gained attention in the medical field due to its high performance in optical and electrical biosensors and actuators.<sup>[119,120]</sup>

Various methods have been developed to fabricate NPG, either from pure gold substrates or from alloys. Among these, by far the most common approach is the dealloying of Au-Ag alloys, which has been extensively employed as a reliable route to generate the characteristic nanoporous structure.<sup>[105,121–124]</sup> Other strategies include, for example, the deposition and subsequent selective etching of Au–Ag colloids.<sup>[125]</sup>

A common approach to achieving a nanoporous structure involves the corrosion of the less noble element within an alloy. In the case of binary systems, such as Au and Ag, the initial alloy structure undergoes a transformation, resulting in the formation of a nanoporous sponge-like material primarily composed of the more noble element from the original alloy. This method allows for the precise control and manipulation of the nanoporous structure, making it a valuable technique in the fabrication of NPG with tailored properties for various applications. Nonetheless, the process of dealloying an Ag-Au alloy can only take place when the silver (Ag) content within the alloy exceeds the parting limit, which typically falls within the range of 50 to 60 atomic percent<sup>[126]</sup> for binary alloys with a face-centered cubic lattice structure.<sup>[127]</sup>

Unlike supported Au nanoparticles, NPG does not rely on support material to construct three-dimensional electrodes or catalyst structures. This attribute simplifies the investigation of reaction mechanisms since the complexities associated with the interactions of reactants, intermediates, and products with the support or the ligand shell of nanoparticles are eliminated.

However, it is worth noting that NPG thin films can still be engineered on various supports for mechanical stability, such as glass slides<sup>[128,129]</sup> and silicon wafers.<sup>[130,131]</sup> Unlike nanoparticles dispersed finely on a porous support, in thin films, only the bottom layer comes into contact with the flat support, exerting a minimal influence.

The intricate microstructure of nanoporous gold formed by dealloying Ag-Au alloys was investigated using electron tomography and HAADF-STEM imaging. A three-dimensional reconstruction of the material revealed a highly interconnected, bicontinuous network of nanoscale ligaments and pores. The structure is characterized by a high specific surface area and significant structural inhomogeneity, with a wide distribution of ligaments and sizes.<sup>[132]</sup> The pronounced curvature of the ligaments in nanoporous gold leads to a high density of low-coordination gold atoms, which are key to the material's notable catalytic activity, especially in CO oxidation. Residual silver (Ag), typically present in small amounts after dealloying, enhances this catalytic activity, particularly by facilitating the activation of molecular oxygen, which is a key step in low-temperature CO oxidation. Nanoporous gold also demonstrates exceptional selectivity in oxidation reactions, such as the oxidative coupling of methanol and other alcohols.<sup>[110,133]</sup> This unique combination of high reactivity, selectivity, and robustness suggests a promising role for nanoporous gold in real-world catalytic applications, advancing gold-based catalysis toward practical use.<sup>[134]</sup>

Nanoporous electrodes are able to significantly enhance electrochemical efficiency, particularly for slow reactions. The improvement is primarily due to the increased interaction time between reactant molecules and the electrode surface within the nano-confined spaces, leading to more frequent collisions and higher reaction rates.

However, a critical aspect to consider of nanoporous electrodes is the overlapping of the electric double layer (EDL). When the pore size is similar to or smaller than twice the EDL thickness, the EDLs overlap, resulting in a lower electrical field gradient within the nanopores. This overlap reduces the effective surface area available for electrochemical reactions and leads to a loss of double-layer capacitance, which can be measured through cyclic voltammetry. Lower ionic strength and smaller pore sizes increase the likelihood of EDL overlapping, impacting the overall electrochemical performance of the electrodes.

Furthermore, Knudsen diffusion also plays a significant role in nanoporous materials. This type of diffusion occurs when the mean free path of gas molecules is comparable to or larger than the dimensions of the pores, causing molecule-wall collisions to dominate the transport process. While

this mechanism is particularly relevant for gas-phase applications of nanoporous materials, in the present thesis the focus lies on liquid-phase electrochemical systems where molecular diffusion in the electrolyte governs mass transport. Nevertheless, the concept of Knudsen diffusion illustrates how pore dimensions can strongly affect transport phenomena, underlining the general importance of pore size effects also for nanoporous electrodes.<sup>[135]</sup>

Erlebacher et al.<sup>[136]</sup> proposed that the formation of nanoscale porosity during dealloying in noble metals like gold arises from a spontaneous phase separation process, which they described in terms of spinodal decomposition at the solid–electrolyte interface. This interpretation offers a physical explanation for the emergence of a bicontinuous, self-organized nanoporous network.<sup>[137]</sup>

The basic mechanism of spinodal decomposition was first described by Cahn and Hilliard in the mid-20th century.<sup>[138–141]</sup> It involves the spontaneous separation of a homogeneous phase into two distinct compositions without the need for nucleation. This is governed by the free energy of the system, and the driving force is a negative second derivative of the free energy with respect to composition.

Figure 16 illustrates the spinodal and metastable regions of a regular solution. The diagram plots the normalized temperature as a function of composition  $c$ , illustrating the single-phase, metastable, and unstable (spinodal) regions characteristic of a regular solution. The critical temperature  $T_c$ , also known as the consolute temperature, marks the highest temperature at which phase separation can occur and corresponds to the point where the spinodal and binodal curves converge.

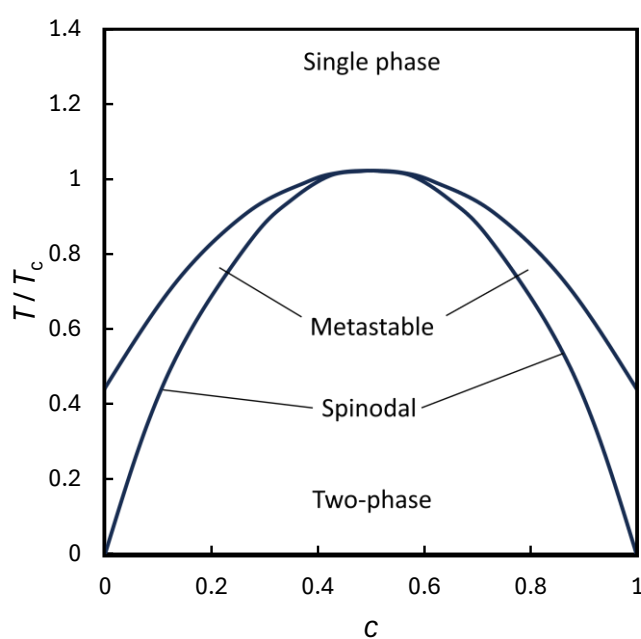


Figure 16. Phase diagram of a regular solution illustrating both the phase boundary at equilibrium and the spinodal region.

The time evolution of such systems can be simulated using the Cahn–Hilliard equation.<sup>[138]</sup> To illustrate this, the Cahn–Hilliard equation was implemented in MATLAB, and the resulting concentration profiles are shown in Figure 17.

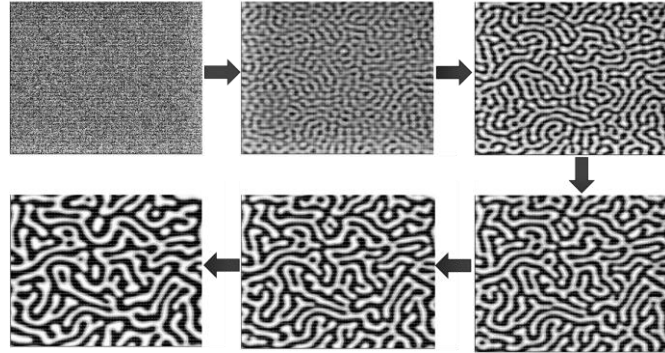


Figure 17. Evolution of the concentration profiles due to spinodal decomposition.

The concentration profile evolution captures the progressive separation of interconnected domains into characteristic bicontinuous structures, resembling the morphologies typically observed in nanoporous metals.

### 2.7.3 Deriving pore structure models from experimental images

In this context, image-based modeling approaches offer a valuable strategy to extract structure-property relationships from experimental data. Instead of relying solely on theoretical calculations, actual microstructural features can be extracted from SEM or tomography images, binarized, and processed to compute porosity and tortuosity. A freely available application developed in MATLAB has been proposed<sup>[142]</sup> to calculate the tortuosity and volume fractions from sequentially ordered two-dimensional tomography images of a three-dimensional microstructure. In line with this idea, a two-dimensional SEM (scanning electron microscopy) image of NPG provided by Dr. Matthias Graf (group of Prof. Dr. Jörg Weißmüller from Hamburg University of Technology) shown in

Figure 18, was first imported in MATLAB and converted to a binary image by replacing all pixels with luminance greater than a value set arbitrarily between 0 and 1.

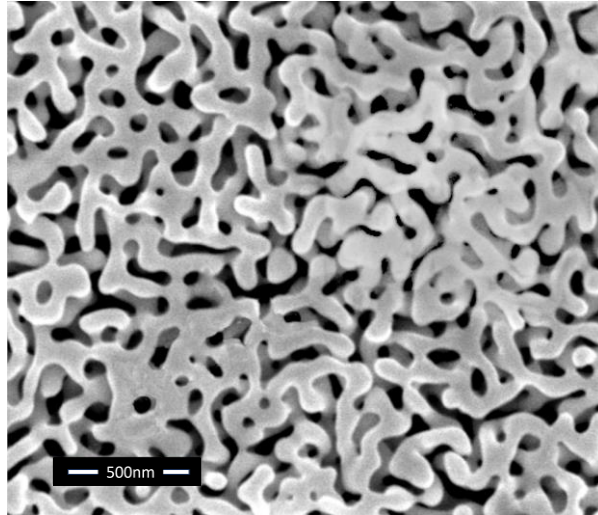


Figure 18. SEM image of nanoporous gold (NPG) provided by Dr. Matthias Graf (Prof. Weißmüller's group, Hamburg University of Technology). The image shows the bicontinuous ligament-pore structure used to generate the simulation geometries.

All pixels with a luminance larger than the chosen value were set to 1 (white) and all other pixels were set to 0 (black). The binary image can then be imported in COMSOL as a geometry using the Livelink for MATLAB module. Values of 0.5 and 0.6 produced the geometries shown in Figure 19, which show a pattern similar to the theoretical spinodal model in Figure 17. However, even at this early stage, the used image presents several obvious critical drawbacks.

As the image is a single two-dimensional SEM image of a three-dimensional structure instead of a series of images taken at different depths, it lacks the ability to provide any depth information to relate the pathways. The extracted 2D slice represents only a single plane of a complex 3D network and thus cannot capture the full connectivity or tortuosity in the out-of-plane direction. Consequently, any transport property derived from this approximation will inevitably miss potential pathways and constrictions that exist in the third dimension.

Additionally, the binarization process itself introduces ambiguity. The value used to segment the grayscale image into binary regions (solid vs. pore) is inherently arbitrary and can significantly influence the calculated porosity and geometry. Small changes in this value may result in fragmented structures, disconnected pore pathways, or loss of morphological details. While two thresholds (0.5 and 0.6) were explored in this work to obtain realistic geometries, the lack of correlation with a full 3D dataset limits the reliability of this approach.

The inversion between the tomography image and the resulting binary image from MATLAB, where ligaments and pores are switched, further complicates interpretation. Although this inversion is not fundamentally problematic due to the compositional symmetry of spinodal decomposition, it adds another layer of abstraction that may confuse the physical meaning of the simulated domains. In theory, spinodal systems exhibit symmetry around the critical composition (e.g., 0.3 Au / 0.7 Ag vs. 0.7 Au / 0.3 Ag), which justifies this flexibility to some extent. However, real experimental structures often deviate from ideal symmetric morphologies due to kinetics, coarsening, or fabrication-related anisotropies.

Most critically, the assumption that the 2D porosity corresponds directly to the 3D porosity of the actual material is questionable. While the grayscale SEM image may provide a representative surface section, the continuity and interconnectivity in 3D can dramatically alter the effective transport behavior. The simulations shown here are thus best interpreted as exploratory in nature; they aim to evaluate the feasibility of an image-based modeling workflow and to qualitatively compare geometries under simplified conditions. They are not intended to yield quantitatively accurate predictions of transport behavior in real NPG samples.

The electrolyte was chosen to occupy the grey domain as it is the only continuous phase in the 2D image and the solid NPG matrix the white domain. The porosity was then calculated by measuring the area of the gray domain and dividing it by the total area resulting in  $P=0.729$  for a) and  $P= 0.648$  for b) which are within the normal range of porosity in NPG.

The upcoming section discusses the simulation conducted to calculate the transport properties for both geometries and then the results are compared to effective transport models.

## **2.8 Simulation of the heterogenous material**

Simulations were conducted to calculate the transport properties due to diffusion for both geometries in Figure 19 to obtain effective transport models.

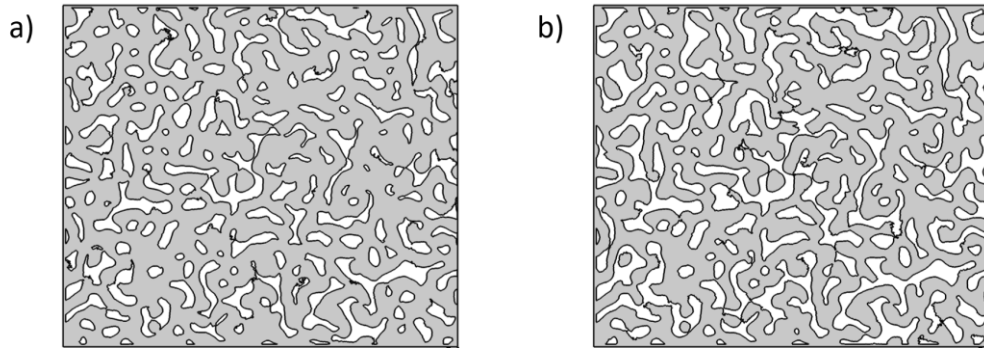


Figure 19. Geometries obtained from the NPG SEM image, a) luminance of 0.5 b) luminance of 0.6.

The simulations were performed with COMSOL using the *transport of diluted species* module in a two-dimensional coordinate system. Only geometry a) is shown here as both geometries are very similar.

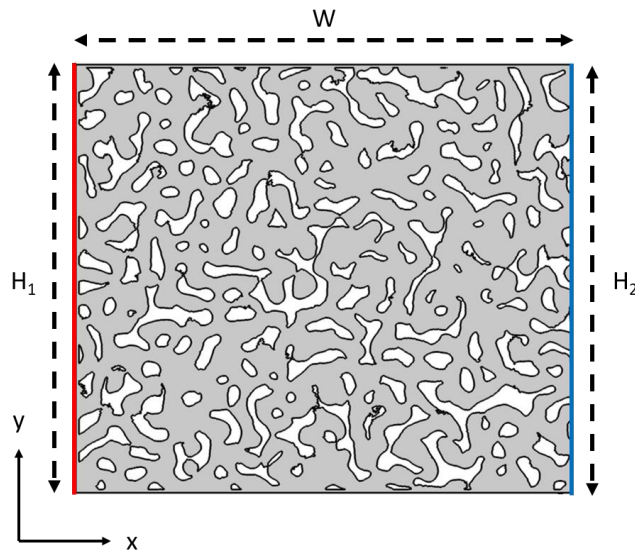


Figure 20. Simulation geometry generated for the two-dimensional image of the NPG sample in Figure 19a.

### ***Electrolyte Domain (grey area)***

A stationary simulation was first run on heterogeneous geometries. A concentration difference was set between both boundaries  $H_1$  and  $H_2$  to establish the concentration gradient across the electrolyte.

Steady-state transport is described by Fick's second law

$$\frac{\partial c_i}{\partial t} = D \left( \frac{\partial^2 c_i}{\partial x^2} + \frac{\partial^2 c_i}{\partial y^2} \right) = 0 \quad (72)$$

with the initial concentration

$$c_{\text{ini}} = 0 \text{ M} \quad (73)$$

### **Boundary $H_1$**

A fixed concentration of 10 mM was established at boundary  $H_1$

$$c_1 = 10 \text{ mM} \quad (74)$$

### **Boundary $H_2$**

A fixed concentration of 0 mM was established at boundary  $H_2$

$$c_2 = 0 \text{ M} \quad (75)$$

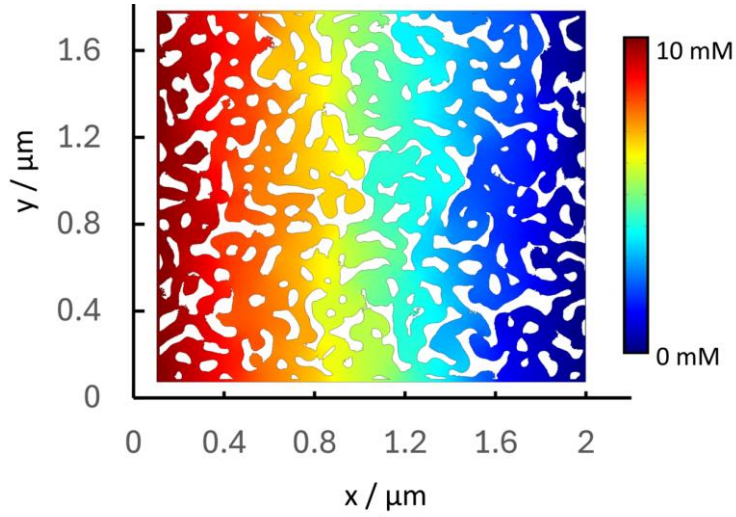


Figure 21. Concentration profile of the stationary simulation on the heterogeneous geometry.

The calculated steady-state concentration profile within the porous structure can be seen in Figure 21. The flux  $J_{\text{avg}}$  was calculated at boundary  $H_2$  and used to obtain the effective diffusion coefficient  $D_{\text{eff}}$  as shown in Eq. (77), which substitutes the differential expression of the concentration for a discrete difference.

$$J_{\text{avg}} = -\frac{1}{H_2} D \int \frac{\partial c}{\partial x} dy \quad (76)$$

$$D_{\text{eff}} = \frac{J_{\text{avg}}}{\left(\frac{c_2 - c_1}{W}\right)} \quad (77)$$

By obtaining  $D_{\text{eff}}$  it is now possible to obtain the tortuosity of the geometry as shown in Eq. (16).

$$D_{\text{eff}} = \frac{P}{\tau} \cdot D \quad (78)$$

Assuming a diffusion coefficient  $D = 5.5 \times 10^{-10} \text{ m}^2 \text{ s}^{-1}$  the following results were obtained for both geometries.

Table 4. Effective transport parameters of heterogeneous geometries.

	Geometry a)	Geometry b)
$D_{\text{eff}}$	$1.94 \times 10^{-10} \text{ m}^2 \text{ s}^{-1}$	$1.04 \times 10^{-10} \text{ m}^2 \text{ s}^{-1}$
$J_{\text{avg}}$	$1.2026 \times 10^{-3} \text{ mol m}^{-2} \text{ s}^{-1}$	$6.4095 \times 10^{-4} \text{ mol m}^{-2} \text{ s}^{-1}$
$P$	0.7295	0.6476
$\tau$	2.0722	3.4301

Transient simulations for a two-dimensional and one-dimensional homogenous domains using the effective transport parameters listed in Table 4 were done and compared to a transient simulation using heterogeneous geometries. The flux was measured at the right edge of all simulation spaces ( $\text{H}_2$  in the heterogeneous geometry shown). The diffusion equation for the homogenous models was defined as shown in Section 2.4

$$P \frac{\partial c}{\partial t} + \nabla \cdot (-D_{\text{eff}} \nabla c) = 0 \quad (79)$$

The flux was measured at the right edge of all simulation spaces ( $\text{H}_2$  in the heterogeneous geometry shown) and is shown in Figure 22.

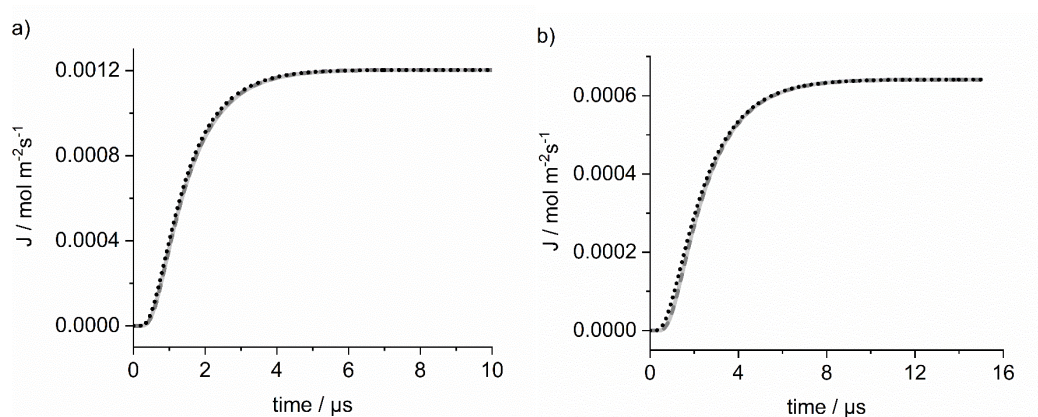


Figure 22. Comparison between boundary fluxes simulated with heterogeneous geometries from Figure 19a) and Figure 19b) and homogeneous one-dimensional and two-dimensional geometries. Heterogeneous (black dots), two-dimensional homogeneous (dark grey dashed), one-dimensional homogeneous (light grey straight line).

There is excellent correspondence among all three approaches which validate the use of effective transport properties instead of the heterogenous one. In the personal computer where the simulations were run, (Xeon 3.6 GHz, 32 Gb RAM. Windows 7) a 10  $\mu\text{s}$  simulation took 7 min 29 s for the heterogenous model, 14 s for the 2D homogenous, and 5 s for the 1D, with a file size of 10.55 GB, 60.8 MB, and 5.8 MB, respectively.

Due to the limitations in processing SEM images of NPG to generate accurate simulation geometries, the results cannot fully characterize the NPG sample. However, the model reduction and effective transport parameters provide a feasible approach, given that a suitable method for obtaining accurate geometry is available or the porosity is known.

### **3. Heterogeneous model of SI-SECM on cavity filled electrodes.**

#### **3.1 Cavity microelectrodes**

Cavity microelectrodes (CMEs) filled with porous electrocatalyst materials provide a reproducible and spatially defined platform for studying high-surface-area electrochemical systems. CMEs were introduced in the 1990s and have since found applications in characterizing a wide range of materials.<sup>[143]</sup> Their versatility has also led to applications in corrosion, catalysis, and biological systems, making them a robust tool for studying small, immobilized amounts of material.<sup>[144,145]</sup> This enables the extraction of quantitative electrochemical information on electrode material properties, even when working with only a few hundred nanograms of active phase.<sup>[146,147]</sup> CMEs have also been exploited to gain high-resolution insights when used as SECM probes to provide localized electrochemical information.<sup>[144]</sup>

CMEs are typically fabricated by sealing a metallic micro wire, such as platinum or gold, into a glass rod and then creating a microcavity through chemical etching. The microcavity can be filled with various electroactive materials, making CMEs highly versatile for systematic electrochemical studies.<sup>[145]</sup>

These advantages are particularly relevant in the context of surface interrogation SECM (SI-SECM), which is used to study surface-bound intermediates. However, filling CMEs with porous powders introduces additional complexity as diffusion pathways and the effective reaction volume are altered, which can lead to distorted voltammetric features, added resistance, capacitance, and limitations at high scan rates.<sup>[148,149]</sup> Therefore, while CMEs are powerful tools for high-speed studies, careful consideration of the porosity of the sample material is necessary to avoid misinterpretation of reaction kinetics.

Electrochemical etching<sup>[150]</sup> has proven to be a reliable preparation method of CMEs, particularly NPG MEs. The cavity depth, which is a key factor, as it influences the accessible surface area, mass transport characteristics, and reproducibility of the electrochemical measurements can be controlled by adjusting the etching times during fabrication.<sup>[145]</sup>

The present chapter introduces a finite element simulation model that extends this approach to the case of CMEs. The model was developed as part of a collaborative study that has been published.<sup>[151]</sup> The author's primary contribution to that work was the conceptualization, design, implementation,

and analysis of the simulation model, while the experimental SI-SECM investigations were carried out by Mareike Hänsch (Au/C electrodes) and Julian Behnken (Pt/C electrodes).

The model captures the spatial coupling between mediator diffusion and surface reactions occurring throughout the internal surface of the porous film. A key feature is its abstraction of the porous layer as a series of concentric layers that approximate the increased surface area inside the cavity, without explicitly resolving each pore. This structure enables the simulation to reproduce the depth-dependent titration behavior (referred to as vertical feedback) where redox mediator molecules progressively access and reduce adsorbed oxide species at increasing depths within the porous material.

The following sections detail the construction of the model, its physical basis, and its capacity to explain transient SECM responses measured on Pt/C and Au/C porous electrodes. In particular, the model supports the interpretation that multiple adsorbed oxide species with different reactivities coexist in these systems, and that their titration by the redox mediator occurs sequentially depending on their local accessibility and intrinsic kinetics.

### **3.2 Description of the research problem**

As previously mentioned, nanoporous conductive structures, such as nanoporous gold (NPG) and platinum nanoparticles on carbon support (np-Pt/C), combine the properties of both metals and nanostructured materials, exhibiting structure-related electrical, magnetic, mechanical, optical, catalytic, and electrocatalytic properties.<sup>[152]</sup> The electrochemical response of CMEs can vary considerably compared to flat conductive substrates.<sup>[153]</sup> The study of redox properties of porous electrode materials is central for understanding and optimizing their performance.

Traditional methods often fall short when applied to porous materials due to their complex structures and high surface areas. The development of CMEs combined with SI-SECM offers a novel approach to overcome these limitations. To enable the use of SI-SECM with porous materials, the Wittstock research group developed an extension of the technique for electrocatalysts in powder form.<sup>[151]</sup> In this configuration, the conventional flat microelectrode used to generate the adsorbate layer (as described in Section 2.3.3) is replaced by a cavity microelectrode filled with the catalyst powder, forming a porous electrode confined within the cavity. This adaptation eliminates the need to prepare the catalyst material as a freestanding microelectrode, thereby simplifying the experimental procedure and expanding the applicability of SI-SECM to a broader range of catalyst materials, which are often synthesized and used in powder form.

Previous digital simulation efforts focused primarily on SI-SECM experiments using flat, non-porous substrates.<sup>[154–158]</sup> The objectives of this study are to improve the performance of electrocatalysts through a combined approach of experimental SI-SECM and digital simulations. The research aims to provide deeper insights into the redox titration mechanisms at porous microelectrodes, validate experimental observations through simulations, and understand the kinetic behavior of surface oxides on NPG and Pt/C.

### 3.3 Experimental details covered in the simulation

In this study, all potential values are reported relative to the standard hydrogen electrode (SHE), and the concentration of the redox mediator used in the experiments was 10 mM.

The tip–sample working distance  $d$  was established using a two-step procedure. First, collinear alignment of tip and sample was achieved in sample-generation/tip-collection (SG/TC) mode. Second, the vertical distance was adjusted by feedback approach curves until the desired  $d$  was reached. Alignment was considered successful when the collection efficiency exceeded 94 %. In routine experiments  $d = 2\text{--}5\ \mu\text{m}$  was used, while additional tests were performed at larger distances (3, 8, and 15  $\mu\text{m}$ ) to examine the influence of the gap on the current response.

Surface oxides were generated at the cavity microelectrode (CME) by applying a controlled potential (120 s for NPG, 60 s for Pt/C) prior to surface interrogation. Following oxide formation, the CME was set to open circuit potential. Redox titration at the ME was performed by chronoamperometry for 100 s to produce the reduced form of the mediator, which then reacted chemically with the surface oxides and regenerated the oxidized form of the mediator.<sup>[151]</sup>

### 3.4 Experimental data

Figure 23a shows the experimental SI-SECM curves for NPG at various oxide formation potentials. While the overall shape of the transients is consistent, increasing the applied potential leads to longer titration durations, suggesting greater oxide coverage. The current plateau observed prior to decay reflects the reduction of adsorbed oxides and scales with the applied potential. Figure 23b compares transients recorded at different cavity depths using NPG with a fixed oxide preparation potential. As expected, longer titration durations are observed at greater depths, likely due to the increased oxide loading and extended diffusion path within the cavity. Small variations in curve shape may also reflect differences in packing homogeneity. In all cases, the final stages of the transient show a modest

current increase, which may indicate the presence of multiple oxide species with differing accessibility or reactivity. However, no structural data is available to confirm this interpretation.

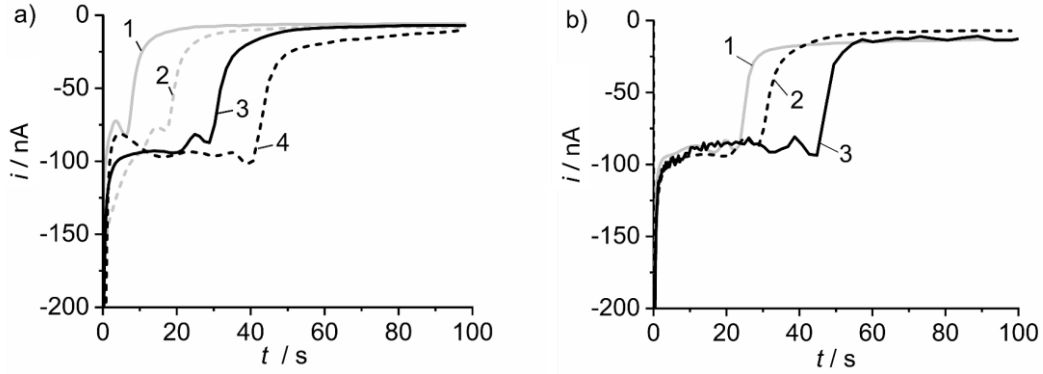


Figure 23. Experimental SI-SECM curves on NPG at different oxide generation potentials and a cavity depth of 34  $\mu\text{m}$  (left): (1a) 1.28 V, (2a) 1.58 V, (3a) 1.88 V, (4a) 2.18 V. Experimental SI-SECM curves on NPG with oxides adsorbed at 1.88 V and varying cavity depths (right): (1b) 11  $\mu\text{m}$ , (2b) 34  $\mu\text{m}$ , (3b) 17  $\mu\text{m}$ . Working distance for all cases was 3  $\mu\text{m}$ . Figure taken from own publication.<sup>[151]</sup>

The electrochemical active surface area ( $A_{\text{ECSA}}$ ) of the NPG-CMEs was determined by cyclic voltammetry in oxygen-free 0.1 M  $\text{H}_2\text{SO}_4$ .<sup>[159]</sup> In this method, the oxide reduction peak ( $i_p$ ) in the cathodic scan is integrated after subtraction of the background current ( $i_{\text{bg}}$ ) and divided by the scan rate ( $v$ ). By selecting a positive potential limit just before oxygen evolution (Burshtein minimum), it is assumed that one monolayer of oxide has formed. Using the reference charge density of  $Q_{\text{ox}} = 386 \mu\text{C}$  for one monolayer of gold oxide,<sup>[160,161]</sup> the  $A_{\text{ECSA}}$  is calculated using Eq. (80)

$$A_{\text{ECSA}} = \frac{\frac{1}{v} \int_{E_1}^{E_2} (i_p - i_{\text{bg}}) dt}{Q_{\text{ox}}} \quad (80)$$

The  $A_{\text{ECSA}}$  of the Pt/C-CMEs was evaluated from the charge of the hydrogen adsorption/desorption in the hydrogen underpotential deposition region. A value of  $Q_{\text{ox}} = 210 \mu\text{C}$  for 1 ML of adsorbed hydrogen was applied.<sup>[162]</sup> Table 5 lists the calculated values of  $A_{\text{ECSA}}$  for NPG-CMEs and Pt/C-CMEs.

Table 5. Cavity depths and electrochemical surface area of the CMEs

CME	Cavity depth / $\mu\text{m}$	$A_{\text{ECSA}}/\text{mm}^2$
NPG <sub>11<math>\mu\text{m}</math></sub>	11	0.375
NPG <sub>17<math>\mu\text{m}</math></sub>	17	0.965
NPG <sub>34<math>\mu\text{m}</math></sub>	34	0.545
Pt/C <sub>8<math>\mu\text{m}</math></sub>	8	0.154
Pt/C <sub>11<math>\mu\text{m}</math></sub>	11	0.289
Pt/C <sub>15<math>\mu\text{m}</math></sub>	15	0.328
Pt/C <sub>17<math>\mu\text{m}</math></sub>	17	0.455

The titration time was determined from the chronoamperometric current–time curves as the point at which the current decayed to the negative feedback value of mediator diffusion, indicating complete reduction of the surface oxides. A comparison of  $A_{\text{ECSA}}$  values among the three NPG electrodes and the titration times reveals a near linear relationship (Figure 24) indicating that  $A_{\text{ECSA}}$  is a more reliable parameter for interpreting titration kinetics than cavity depth alone. This highlights the importance of surface area normalization when comparing SI-SECM responses in porous systems.

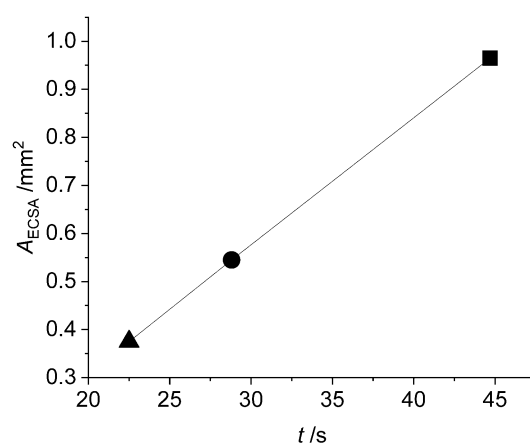


Figure 24. Relation between electrochemical active surface area and titration time. An almost linear relation is observed in the NPG experiments which is unrelated to the cavity depth. Cavity depths: (triangle) 11  $\mu\text{m}$ , (circle) 34  $\mu\text{m}$ , (square) 17  $\mu\text{m}$ . Figure taken from own publication and slightly modified.<sup>[151]</sup>

The SI-SECM transients obtained with Pt/C electrodes exhibited distinctly different behavior compared to NPG. As shown in Figure 25, curve 1 (0.8 V) corresponds to a lower oxide formation

potential and shows a small and gradual decay in current, suggesting a limited amount of reactive oxide. At higher formation potentials (curves 2 and 3), the current initially drops rapidly, followed by a broader current maximum and a delayed decay. These features point to the presence of more complex redox behavior than in the NPG case.

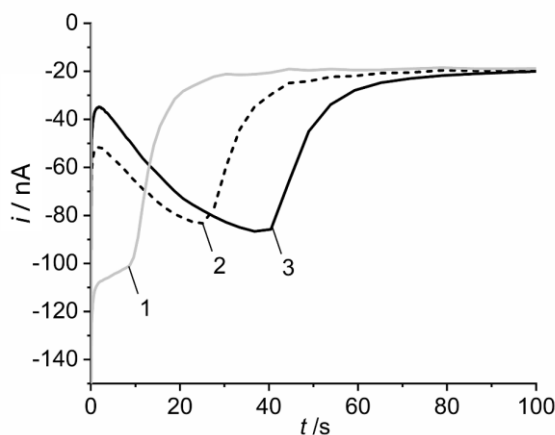


Figure 25. Experimental SI-SECM curves on Pt/C in a CME of 15  $\mu\text{m}$  cavity depth with different oxide generation potentials: (1) 0.8 V, (2) 1.0 V, (3) 1.2 V. Working distance for all cases was 5  $\mu\text{m}$ . Figure taken from own publication and slightly modified.<sup>[151]</sup>

One possible interpretation is that an initial oxide layer forms which reacts more slowly, and once breached, exposes a more reactive oxide underneath, resulting in the observed current increase. This scenario could arise from differences in accessibility or reactivity within the oxide film. However, it should be emphasized that no structural data is available to verify this interpretation, and the presence of stratified oxide layers remains speculative. The observed current decay following the peak suggests progressive depletion of reactive sites until the system reaches the negative feedback regime.

### 3.5 Porous substrate and description of surface reaction

Once the reduced form of the mediator R diffuses to the CME, it interacts with the porous substrate in ways that can lead to a diverse array of reaction mechanisms. These interactions are influenced by the characteristics of the substrate and the surface properties, potentially resulting in complex reaction pathways. A schematic representation of possible reaction mechanisms is provided in Figure 26, illustrating the intricate dynamics at play during this process. Upon reaching the surface, R reacts directly with the adsorbed oxides (A), resulting in the regeneration of the oxidized mediator form, O,

along with the formation of a product P (Figure 26a). As the outer surface is depleted of A, R continues to diffuse through the inner pores and titrates the inner surface (Figure 26b). Since the solid structure of the CME is conductive, the surface potential is uniform across its entire surface and a similar effect to the formation of a concentration cell when probing extended conductive substrates can be expected. The porous network becomes saturated with O and thus, its surface is positively biased. The reduced form R converts into O as soon as it comes in contact with the surface of the porous electrode and electrons are conducted through the solid matrix reducing O at a random location at an inner pore, which can be again oxidized as long as the surface is positively biased due to the mediator concentration in contact with the porous network inner surface (Figure 26c). This effect speeds up the titration considerably as electronic conductivity is much higher in the nanoporous metallic network than the diffusion and ion conductivity in the pore space. Similarly, after R was oxidized the transferred electron can react directly with A at another location of the porous matrix (Figure 26d).

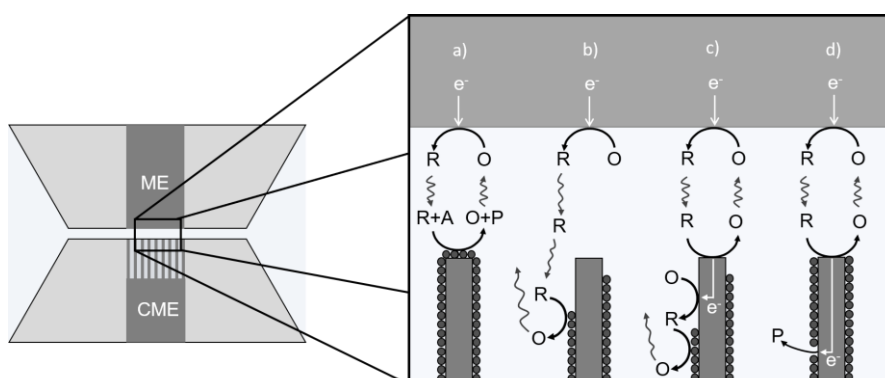


Figure 26. Different reaction mechanisms for the titration of A by R generated at the ME. R diffuses to the outer surface and reacts directly with A regenerating O (a), R diffuses into the pores to further titrate A by direct chemical reaction (b), vertical electron transfer due to formation of a concentration cell at the surface of the CME (c), direct titration of A by electron transfer (d). Figure taken from own publication and slightly modified.<sup>[151]</sup>

The reaction mechanisms from Figure 26c and Figure 26d are expected to enhance the overall titration rate considerably. This effect was coined as “vertical feedback” due to the similarities to the lateral electron transfer which promotes a positive feedback current in classic SECM experiments as described in Figure 4.

The proposed reaction mechanism used for simulations consists of several coupled reaction steps involving the ion diffusion in the electrolyte in the bulk and between both MEs, ion diffusion in the

liquid domain of the porous network, electron conductivity within the nanoporous network, surface reactions between mediator and adsorbed species, and electronic conduction within the metallic network. The central focus of the hypothesis is the reduced reaction time needed to titrate the adsorbed species within the porous structure due to very fast electron transport within the metallic phase.

The treatment of the simulation space as a heterogeneous system consisting of solid and liquid phases presents the advantage of explicitly treating electrochemical reactions and the surface chemical reactions in a natural manner. However, simulating diffusion through a three-dimensional porous network using FEM is a powerful technique, but it comes with several inherent disadvantages. These include the computational complexity associated with solving diffusion equations in three-dimensional space, the intricate task of generating an appropriate finite element mesh for complex porous structures, and the substantial memory and storage requirements for handling large simulations.

The porous domain of the electrode was thus kept as a two-dimensional axisymmetric geometry by generating concentric lamellae of the solid phase which represent the ligaments and the liquid phase of the porous electrode as shown in Figure 27, the spacing between each lamella was 50 nm for the NPG and 100 nm for the Pt/C simulations.

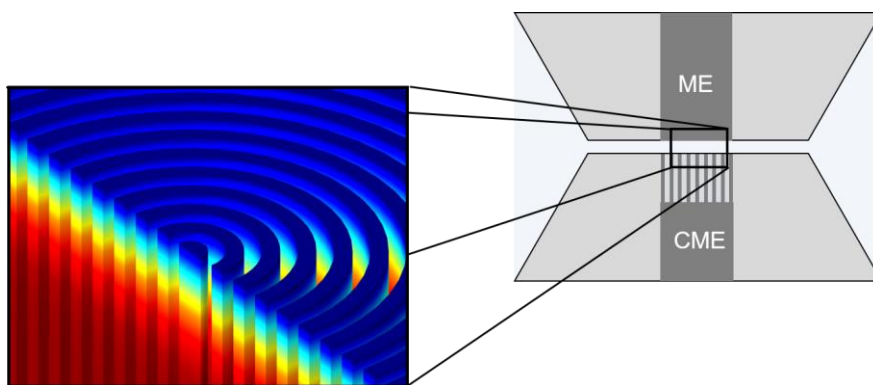


Figure 27. Close-up of a transversal section of a 3D representation of the geometry used to describe the porous substrate in the simulations. The color gradient represents the change in concentration of the mediator as it diffuses through the medium and the void part is the solid impermeable matrix.

The approach of treating the porous domain as a heterogeneous domain allowed to program surface reactions at the boundaries of the lamellae in a scale which approximates the real pore thickness (50-100 nm). As a direct consequence of this, the simulated  $A_{ECSA}$  was comparable (same order of magnitude) to the experimental values (see Table 6).

Table 6. Cavity depths and electrochemical surface area of the simulated CMEs

CME	Depth / $\mu\text{m}$	$A_{\text{ECSA}}/\text{mm}^2$
NPG <sub>8<math>\mu\text{m}</math></sub>	8	0.315
NPG <sub>12<math>\mu\text{m}</math></sub>	12	0.472
NPG <sub>16<math>\mu\text{m}</math></sub>	16	0.629
Pt/C <sub>15<math>\mu\text{m}</math></sub>	15	0.295

To simulate the vertical feedback effect, the first approach was to uniformly set the potential of the entire CME according to the Nernst Eq. (Eq. (5)) and combining it with the Butler-Volmer relation [Eq. (11)] to calculate the electrode potential at the CME in an open circuit potential behavior. This was done by integrating Eq. (5) across the whole surface and dividing by the surface area, in this way the electrode potential auto-corrects itself according to the average concentration of the mediator in contact with the CME. The potential is then substituted in the Butler-Volmer equation as follows

$$E_{\text{CME}} = \frac{1}{A_{\text{CME}}} \cdot \oint_{A_{\text{CME}}} \left( E^{0'} + \frac{RT}{nF} \ln \frac{c_{\text{O}}^*}{c_{\text{R}}^*} \right) \cdot dA \quad (81)$$

$$J_{\text{O}} = -k_0 \left( c_{\text{O}} e^{-\left(\frac{\alpha F}{RT}(E_{\text{CME}} - E^{0'})\right)} - c_{\text{R}} e^{-\left(\frac{(1-\alpha)F}{RT}(E_{\text{CME}} - E^{0'})\right)} \right) = \frac{i_{\text{CME}}}{F \cdot A_{\text{CME}}} \quad (82)$$

$$J_{\text{R}} = -J_{\text{O}} \quad (83)$$

$E_{\text{CME}}$  is the potential of the cavity microelectrode and  $J$  the flux of the corresponding form of the mediator.

This approach of describing the electrode potential worked well for simulations on flat surfaces where the ME current measured on substrates with different radii  $r_{\text{S}}$ . For a small radius ( $R_{\text{S}} = r_{\text{S}}/r_{\text{T}} = 0.1$ , dimensionless substrate radius) the current equals the negative feedback current value. The value rapidly increases with increasing substrate size until reaching  $R_{\text{S}} \approx 20$ , where the current increment in relation to substrate size slows down until finally reaching the positive feedback value at  $R_{\text{S}} \approx 100$ . This is shown in Figure 28.

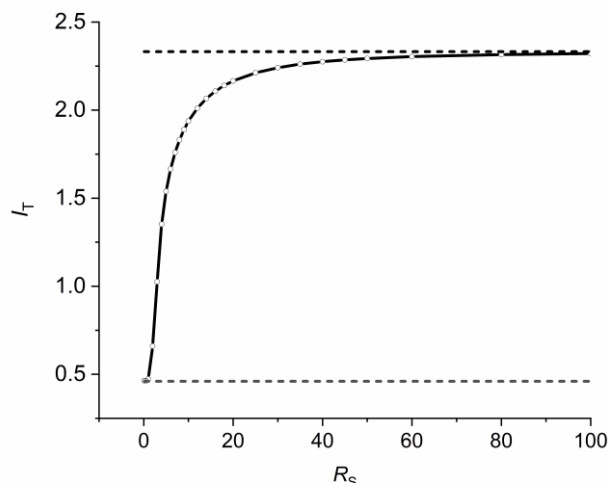


Figure 28. Simulated feedback current on a flat electrode set at OCP with varying normalized substrate electrode radius  $R_s$ ,  $L = 0.5$ ,  $R_g = 3$ . Top and bottom dashed lines indicate the calculated positive ( $\kappa = \infty$ ) and negative feedback ( $\kappa = 0$ ) current values with  $L = 0.5$ ,  $R_g = 3$ .

However, applying this approach to the complex geometry shown in Figure 26 resulted in significantly increased simulation times and convergence issues that could not be fully resolved. These difficulties likely stem from a combination of factors, including the intricate geometry requiring extremely fine meshing within the CME domain and the complexity of the coupled integral operations along the surface, embedded within the exponential terms of the differential equations governing the flux of each species. Furthermore, surface reactions between adsorbates and the mediator introduced additional challenges. Specifically, when the oxide diffusion coefficient was set to zero ( $D_A = 0 \text{ m}^2 \text{ s}^{-1}$ ), an unrealistically large amount of titratable material was predicted. This numerical issue persisted even when set to very small values ( $D_A \approx 0$ ), indicating a fundamental limitation of this approach.

To address these challenges, an alternative method was adapted from Rodriguez-Lopez et al.,<sup>[157]</sup> who encountered similar issues with flat substrate microelectrodes. In their approach, a diffusion coefficient for the oxides was assigned at 100 times the value of the redox mediator in solution. This adjustment effectively simulates the vertical feedback effect facilitated by rapid electron transfer across the CME surface, approximating a conductive substrate where the potential remains uniform across the porous electrode surface. This large value for  $D_A$  ensures a nearly homogeneous concentration of adsorbates throughout the simulation, which serves as a practical substitute for explicitly defining an open circuit potential on a conductive porous electrode.

### 3.6 Simulation description and results

The simulations were conducted using a two-dimensional axisymmetric geometry to represent the system shown in Figure 29. This approach allowed for a simplified yet effective modeling of the porous electrode structure. For the nanoporous gold (NPG) simulations, the pore thickness was set to 50 nm, while for the platinum on carbon support (Pt/C) simulations, a thicker pore size of 100 nm was used. These thicknesses were chosen to approximate the realistic structural characteristics of the materials; however, there was no direct attempt to precisely match the depth to the electrochemically active surface area  $A_{ECSA}$  between the experimental and simulation setups. This decision was due to the high variability observed in the depth and  $A_{ECSA}$  of the experimental samples, which would make exact matching impractical and could introduce unnecessary complexity into the simulation model.

The simulated  $A_{ECSA}$  values for different cavity depths are summarized in Table 6, highlighting the range of geometries tested in the simulations. For NPG, cavity depths of 8  $\mu\text{m}$ , 12  $\mu\text{m}$ , and 16  $\mu\text{m}$  were evaluated, corresponding to  $A_{ECSA}$  values of 0.315  $\text{mm}^2$ , 0.472  $\text{mm}^2$ , and 0.629  $\text{mm}^2$ , respectively. For Pt/C, a cavity depth of 15  $\mu\text{m}$  was modeled, resulting in an  $A_{ECSA}$  of 0.295  $\text{mm}^2$ . These values reflect the anticipated increase in surface area with greater cavity depth, which plays a critical role in the electrochemical response of the CMEs.

A full description of all constants, parameters and equations is found in the appendix 7.1.

#### 3.6.1 Domain equations and boundary conditions

This section describes the equation system used in the simulation space across the domain (I) and boundaries (1, 2, 3 and 4) as specified in Figure 29.

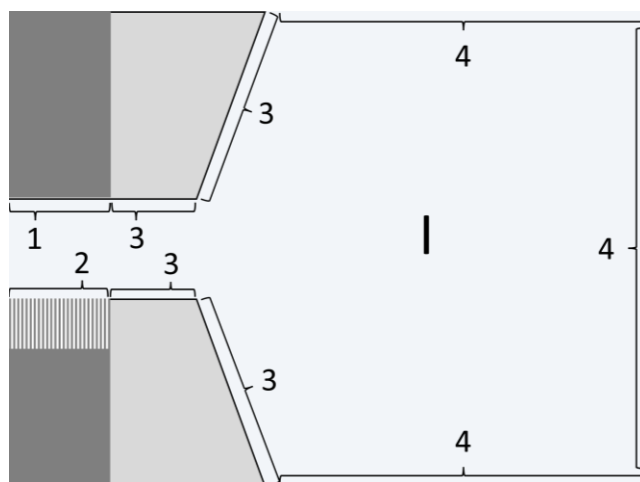


Figure 29. Schematic diagram of the simulation space. Box size for the electrolyte boundaries is 500 times the tip radius.

### ***Diffusion in the electrolyte (Domain I)***

According to the consideration in section 2.1, mass transport occurred exclusively by diffusion. The diffusion equation in cylindrical coordinates is given in Eq. (84), where  $c_i$  is the mediator concentration ( $i = O, R$ ) in its oxidized and reduced forms,  $D_i$  is the diffusion coefficient of the mediator assumed to be equal for both redox species with a value of  $5.5 \times 10^{-10} \text{ m}^2 \text{ s}^{-1}$  as reported for ruthenium hexamine.<sup>[157]</sup>

$$\frac{\partial c_i}{\partial t} = D_i \left( \frac{\partial^2 c_i}{\partial r^2} + \frac{1}{r} \frac{\partial c_i}{\partial r} + \frac{\partial^2 c_i}{\partial z^2} \right) \quad (84)$$

### ***Microelectrode flux (Boundary 1)***

The ME was modeled using Butler-Volmer kinetics with an electrode potential ( $E_T - E^0$ ) of -0.5 V ensuring diffusion-controlled reduction of the redox mediator. The ME used to titrate the substrate had a radius  $r_T = 25 \mu\text{m}$ .

$$\frac{\partial c_O}{\partial t} = -c_O k^0 e^{-\left(\frac{\alpha F}{RT}(E - E^0)\right)} + c_R k^0 e^{-\left(\frac{(1-\alpha)F}{RT}(E - E^0)\right)} \quad (85)$$

$$\frac{\partial c_R}{\partial t} = c_O k^0 e^{\left(\frac{\alpha F}{RT}(E - E^0)\right)} - c_R k^0 e^{\left(\frac{(1-\alpha)F}{RT}(E - E^0)\right)} \quad (86)$$

Where  $k_0$  is the heterogeneous standard rate constant ( $0.01 \text{ ms}^{-1}$ ),  $\alpha$  is the transfer coefficient (0.5),  $F$  the Faraday constant,  $R$  the gas constant,  $T$  the temperature (298 K).  $E_T$  the ME potential (-0.5 V),  $E_0$  the standard redox potential (0.0 V).

### ***Porous substrate (Boundary 2)***

Two different oxides adsorbed at the porous electrode surface were modelled. The first oxide (Ox1) being adsorbed directly at the surface of the porous electrode and the second one (Ox2) being adsorbed on top of Ox1. Under the assumption that Ox2 reacts first with the mediator and only when there is less than one monolayer (ML) of Ox2 present ( $\theta \leq 1$ ), Ox1 becomes accessible to the mediator.

$$\frac{\partial c_O}{\partial t} = (\theta_{\text{ox1}} - \theta_{\text{ox2}}) k_{\text{ox1}} c_R + \theta_{\text{ox2}} k_{\text{ox2}} c_R \quad (87)$$

$$\frac{\partial c_R}{\partial t} = -[(\theta_{\text{ox1}} - \theta_{\text{ox2}}) k_{\text{ox1}} c_R + \theta_{\text{ox2}} k_{\text{ox2}} c_R] \quad (88)$$

**Reaction rate oxide 1 (Boundary 2)**

The inner oxides mass balance equations

$$\frac{\partial \Gamma_{\text{ox1}}}{\partial t} = -(\theta_{\text{ox1}} - \theta_{\text{ox2}})k_{\text{ox1}}c_{\text{R}} + D_{\text{ox1}}\nabla^2 \Gamma_{\text{ox1}} \quad (89)$$

Where  $\Gamma$  is the adsorbate surface concentration in mol m<sup>-2</sup>,  $D$  the adsorbate diffusion coefficient in m<sup>2</sup> s<sup>-1</sup> and  $\theta$  the adsorbate surface coverage.

**Reaction rate oxide 2 (Boundary 2)**

$$\frac{\partial \Gamma_{\text{ox2}}}{\partial t} = -\theta_2 k_{\text{ox2}}c_{\text{r}} + D_{\text{ox2}}\nabla^2 \Gamma_{\text{ox2}} \text{ with } \theta_1 = \min\left(\frac{\Gamma_{\text{ox1}}}{\Gamma_{\text{max}}}, 1\right) \text{ and } \theta_2 = \min\left(\frac{\Gamma_{\text{ox2}}}{\Gamma_{\text{max}}}, 1\right) \quad (90)$$

Here  $\Gamma_{\text{max}}$  is the maximum concentration corresponding to 1 ML of adsorbate.

**Glass Insulator (Boundary 3)**

No flux along the glass sheath is assumed.

$$\frac{\partial c_i}{\partial t} = 0 \quad (91)$$

**Bulk (Boundary 4)**

The bulk boundary conditions were defined at a distance of  $500r_{\text{T}}$  to ensure accurate simulation results without extending the simulation domain unnecessarily.<sup>[163]</sup>

$$c_{\text{O}} = c_{\text{O}}^* \quad c_{\text{R}} = 0 \quad (92)$$

**Current at the ME (Boundary 1)**

The ME current is calculated from boundary values of  $\partial c_{\text{O}}/\partial z$  as described in section 2.6.1

$$i_{\text{T}} = 2\pi F D_{\text{O}} \int_{r=0}^{r=r_{\text{T}}} \frac{\partial c_{\text{O}}}{\partial z} r \, dr \quad (93)$$

The term  $\nabla^2 D_{\text{ox1,2}}$  on the right side of equations (89) and (90) represents the aforementioned surface diffusion of the adsorbed oxides.

Using the surface coverage ( $\theta$ ) instead of the surface concentration ( $\Gamma$ ) directly for the reaction rate allows to easily define the total contribution of each oxide to the surface reaction. At values above 1 ML,  $\theta$  keeps a value of 1 as we assume the maximum amount of oxide exposed to the mediator is 1

ML. The factor  $(\theta_1 - \theta_2)$  that precedes the rate law for the Ox1 reaction with the mediator guarantees that only the outer oxide reacts with the mediator if its surface coverage is larger than that of the Ox2.

The substrate had a radius of 25  $\mu\text{m}$  with depths varying from 8 to 16  $\mu\text{m}$ .

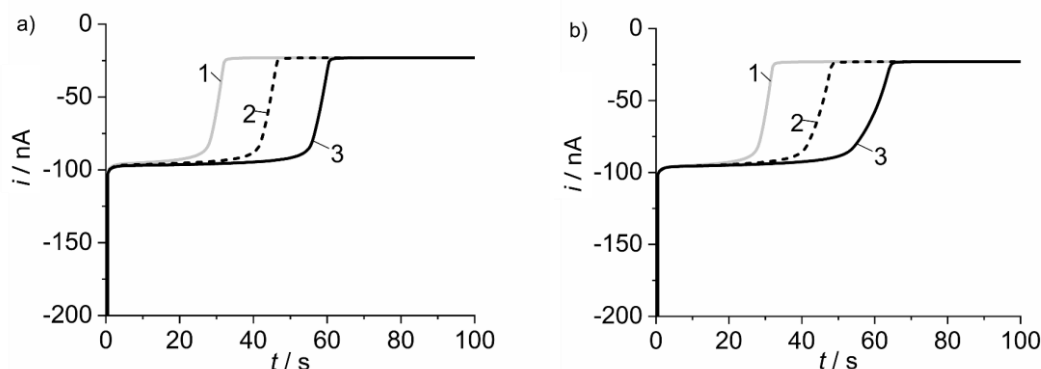


Figure 30. a) Simulated SI-SECM curves for the redox titration on NPG with varying adsorbate coverage and a cavity depth of 8  $\mu\text{m}$ ; (1a)  $\theta_1 = \theta_2 = 0.5$  ML, (2a)  $\theta_1 = \theta_2 = 0.75$  ML, (3a)  $\theta_1 = \theta_2 = 1$  ML V. b) simulated SI-SECM curves for the redox titration of NPG with varying cavity depths; (1b) 8  $\mu\text{m}$ , (2b) 12  $\mu\text{m}$  (3b) 16  $\mu\text{m}$ ,  $D_i = 5.5 \times 10^{-10} \text{ m}^2 \text{ s}^{-1}$ ,  $d = 5 \mu\text{m}$ ,  $c_0^* = 10 \text{ mmol L}^{-1}$ ,  $k_{\text{ox}1} = 0.01 \text{ m s}^{-1}$ ,  $k_{\text{ox}2} = 0.001 \text{ m s}^{-1}$ . Figure taken from own publication and slightly modified.<sup>[151]</sup>

Figure 30a shows the titration curves simulated for NPG with reaction rate constants for the two adsorbates  $k_{\text{ox}1} = 0.01 \text{ m s}^{-1}$ ,  $k_{\text{ox}2} = 0.001 \text{ m s}^{-1}$  and a cavity depth of 8  $\mu\text{m}$ . The fast reaction constants of the mediator with both oxides are high enough that the different oxides being titrated are indistinguishable from one another from the feedback current. As expected, a higher surface coverage leads to a longer titration time, since a larger amount of surface oxide must be reduced. The shape of the curves themselves are identical regardless of the amount of oxide being titrated. Figure 30b shows simulated curves with the same surface coverage ( $\theta_1 = \theta_2 = 0.5$  ML corresponding to 1 ML in total) and varying cavity depth. The titration duration increases as the depth increases and the shape of the current decay, observed once the oxides are completely reduced, presents a slightly less pronounced slope with increasing cavity depth. This effect is more noticeable as the cavity depth increases. This trend is consistent with the experimental curves depicted in Figure 23b where a slightly less pronounced slope at the end of the titration was registered as the cavity depth increases.

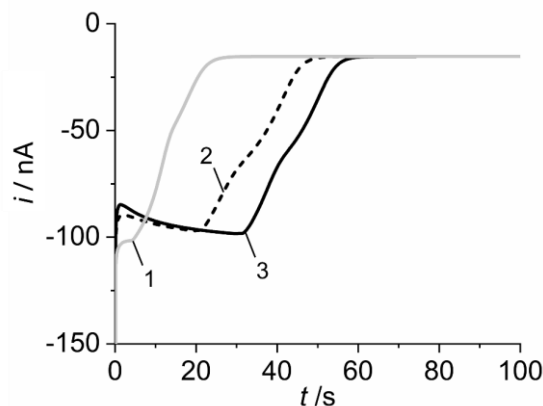


Figure 31. Simulated SI-SECM curves for Pt/C with different starting oxide coverages with a cavity depth of  $15\ \mu\text{m}$ , ME-substrate distance of  $8\ \mu\text{m}$  and  $k_{\text{ox}1} = 1 \times 10^{-5}\ \text{m s}^{-1}$ ,  $k_{\text{ox}2} = 2.4 \times 10^{-6}\ \text{m s}^{-1}$ ; (1)  $\theta_1 = 0.8\ \text{ML}$ ,  $\theta_2 = 0.2\ \text{ML}$ ; (2)  $\theta_1 = 1.5\ \text{ML}$ ,  $\theta_2 = 0.9\ \text{ML}$ ; (3)  $\theta_1 = 2.0\ \text{ML}$ ,  $\theta_2 = 1\ \text{ML}$ . Figure taken from own publication and slightly modified.<sup>[151]</sup>

The simulated curves for Pt/C CME are shown in Figure 31. The reaction constants of the mediator with the adsorbates are  $k_{\text{ox}1} = 1 \times 10^{-5}\ \text{m s}^{-1}$ ,  $k_{\text{ox}2} = 2.4 \times 10^{-6}\ \text{m s}^{-1}$ . The behavior of the experimental curves, as shown in Figure 25, was qualitatively reproduced with an outer oxide (Ox2) that reacts slowly with the mediator. Beneath Ox2, an inner oxide (Ox1) with a larger reaction rate constant produced the increment of the current when Ox2 was consumed by the mediator exposing Ox1, which reacts faster and consequently leads to an increase in the titration current over time, resulting in the distinctive peak-shaped currents registered in the experiments.

To evaluate the influence of the diffusion coefficient of the oxide for representation of the equipotential of the CME surface, the lamella geometry was horizontally segmented so that the porous walls were no longer continuous along the vertical axis as seen in Figure 32. In this configuration, the adsorbates can only diffuse along the walls of individual quadrants, which better represents a non-conductive CME and suppresses the vertical feedback effect. However, the mediator itself can still penetrate through the pore network and diffuse all the way to the bottom of the cavity. Thus, the entire porous volume remains accessible to the mediator, despite the absence of vertical electron transport between segments.

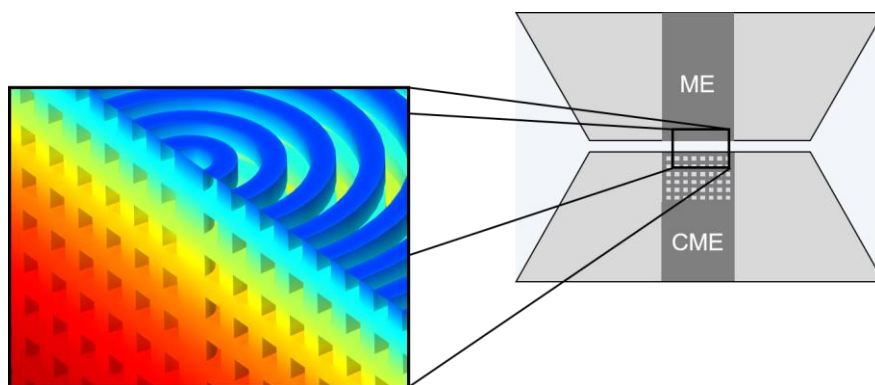


Figure 32. Close-up of a transversal section of a 3D representation of the geometry used to describe the segmented porous substrate in the simulations as a passive CME. The color gradient represents the change in concentration of the mediator as it diffuses through the medium and the void part is the solid impermeable matrix.

The SI-SECM curves for both the concentric lamellae and the segmented geometry of the substrate, as shown in Figure 33, reveal the significant influence of vertical feedback on the electrochemical behavior of CMEs. With identical kinetic parameters and oxide coverage across both configurations, the primary variable was the presence or absence of vertical feedback. Curves 1 and 2 correspond to CMEs with a cavity depth of  $8\ \mu\text{m}$ , while curves 3 and 4 represent a deeper cavity of  $16\ \mu\text{m}$ . The pore size was consistently set to  $200\ \text{nm}$ , which was a deliberate choice to simplify meshing in the simulation space and ensure computational efficiency.

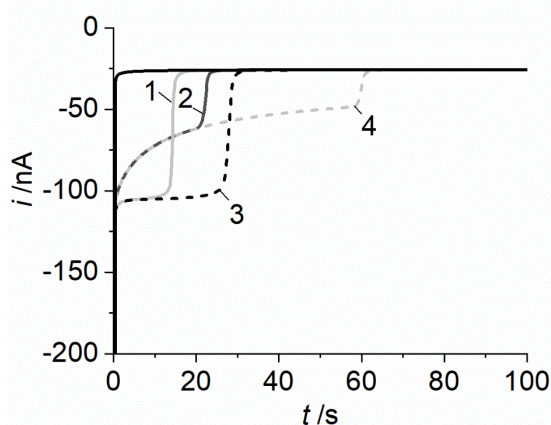


Figure 33. Simulated SI-SECM transients with and without vertical feedback with varying cavity depths. The black solid curve is the background current. Curves 1 and 2 have a depth of  $8\ \mu\text{m}$  and curves 3 and 4 a depth of  $16\ \mu\text{m}$ . Curves 1 and 3 show the titration with vertical feedback. Curves 2 and 4 represent the CME with no vertical feedback.

Without vertical feedback (curves 2 and 4), the current decays continuously in a logarithmic manner as long as there are oxides being titrated. Initially, the decay is relatively rapid, reflecting the easy

access of the mediator to reactive sites near the surface. As the reaction progresses, the decay slows, indicating that the remaining oxides are less accessible or require longer diffusion pathways for interaction. This pattern of decay is influenced by cavity depth, with deeper cavities exhibiting a more extended titration duration due to the increased surface area available for reaction. Once all oxides are titrated, the current transitions more sharply to the negative feedback threshold, marking the completion of the titration.

The decay of the current in curves 2 and 4 resembles curve 2 in in Figure 23 which may indicate incomplete connectivity within the catalyst powder.

Table 7. Integrated charge detected at the ME for the oxide titration simulations shown in Figure 33.

Curve number	Cavity depth / $\mu\text{m}$	Integrated area / $\text{nA}\cdot\text{s}$	Charge / $\mu\text{C}$
1	8	-1046.7	1.05
2	8	-974.0	0.97
3	16	-2103.7	2.10
4	16	-2000.4	2.00

When vertical feedback is present (curves 1 and 3), the current remains relatively stable throughout the titration process, as commonly observed in NPG experiments. This stability indicates that the conductive pathways within the porous network facilitate rapid adsorbate diffusion and uniform potential distribution across the CME surface, maintaining a steady-state reaction rate by mitigating local depletion of reactive sites.

The amount of oxides being titrated was quantified by integrating the simulated current and is shown in Table 7. For both cavity depths, the total charge is slightly higher when vertical feedback is present (curves 1 and 3). The larger charge reflects the faster and more complete titration process enabled by the conductive coupling between different pore regions. In this configuration, vertical electron conduction allows oxide at the lower regions of the cavity to be indirectly reduced, resulting in a more homogeneous potential distribution and faster titration kinetics.

In contrast, in the absence of vertical feedback (curves 2 and 4), the titration proceeds purely by diffusional access of the mediator to the oxide surface. The lack of electronic connectivity between vertical segments slows down the overall reaction, as the lower parts of the cavity can only be reached

through extended diffusion pathways. Consequently, the titration occurs more gradually and with slightly lower total collected charge at the ME.

These findings highlight that vertical feedback is not a universal feature of all conductive porous systems but depends on the degree of electronic connectivity within the porous network. In NPG, the continuous metallic ligament structure provides efficient electron pathways that couple different pore regions, resulting in the stable titration observed experimentally. Conversely, insufficient connectivity, as reflected in the continuous decay of curves 2 and 4, prevents the system from sustaining a stable reaction rate. The similar shape of curve 1 in Figure 25 may therefore indicate incomplete electrical coupling within the catalyst powder.

### 3.7 Conclusions

The simulations with the proposed reaction mechanisms between mediator and oxides successfully reproduced the experimental current transients observed in conductive CMEs. Setting a high diffusion coefficient to the surface oxides enabled the generation of an equivalent model to a uniform potential distribution across the surface of a porous electrode which is much simpler to implement in simulation than having to deal with exponential equations that need to be integrated coupled with one or several surface reactions. Consequently, this method significantly reduces mathematical complexity and calculation time. The proposed geometry further proved to be adequate to represent the experiments on CME. The simulated  $A_{ECSA}$  was in the same order of magnitude as the real CMEs, which allows to evaluate the impact of the conductive surface and the surface reactions between adsorbates and mediator, all without the need for a homogenized medium. Furthermore, fine details like the slight variation of the slope observed at the end of the titration, depending on the cavity depth, were replicated by the model.

For Pt/C-CMEs, the unexpected experimental current profile could be qualitatively reproduced by the simulations, pointing to the presence of at least two different oxide layers with significantly different reaction rate constants. The simulation model, however, could not capture all the intricacies of the experimental SI-SECM curves. This could be due to the irregular intrinsic geometric properties of the CMEs and the grain distribution and packing of the catalyst powders within the experimental setup. Nevertheless, the vertical feedback could be identified as the main effect. Its consequences to the experimental curves were reproduced by the simulation model, which explains the indirect and fast titration of oxides along the extended surface of the CMEs.

## 4. Homogeneous model of passive porous substrates

This chapter presents the use of numerical simulations and analytical models to determine transport properties of porous substrates. The primary focus lies on the development and evaluation of a new analytical equation<sup>[164]</sup> [Eq. (109)] designed to describe SECM approach curves on porous substrates, allowing for the estimation of key parameters such as porosity, tortuosity, and film thickness. The existing analytical model<sup>[165]</sup> [Eq. (94)], which simplifies SECM feedback currents into a linear combination of contributions from the porous material and the electrolyte, was found to have limitations in accurately capturing the complex transport dynamics within porous structures.

To address these limitations, numerical simulations were conducted using a two-dimensional axisymmetric geometry. These simulations modeled the diffusion of mediators through porous layers by incorporating corrected porosity and effective diffusion coefficients, following relations like the Bruggeman equation.<sup>[166,167]</sup> The simulations enabled a thorough exploration of how structural factors such as variable pore sizes, tortuosity, and skin layers influence mass transport, providing a more accurate representation of SECM responses compared to the existing analytical model.

The results from the simulations were used to refine and validate the new analytical equation, Eq. (109), which demonstrated significantly improved accuracy over a wide range of fitting parameters, including variations in film thickness, porosity, and the ratio of sheath to electrode radii. However, Eq. (109) still has some caveats, including its dependence on ten numerical parameters, which, while enhancing accuracy, add complexity to the model. Additionally, the equation does not fully cover the entire porosity range ( $P = [0-1]$ ), highlighting the need for further refinement.

This work was published as part of a collaborative study involving experimental contributions from Mareike Hänsch and analytical development and simulation by the author of this thesis.<sup>[164]</sup> The study illustrates the importance of combining analytical modeling with numerical simulations to improve the reliability of SECM-based methods for characterizing porous electrodes. Future work should aim to streamline these models and reduce parameter dependence while extending applicability to a wider range of porous systems.

### 4.1 Description of the research problem and the experimental data

This study employed scanning electrochemical microscopy (SECM) to investigate mass transport phenomena in nanoporous gold (NPG) electrodes. As discussed in Section 2.7.2, NPG has the particular characteristic in that its pore size can be tuned by controlling the dealloying

potential<sup>[121,136,168,169]</sup> during the electrochemical dealloying<sup>[170]</sup> and can be further adjusted at room temperature by post-processing.<sup>[130]</sup> SECM combined with controlled in-situ coarsening processes allows to investigate the change in structural properties of NPG and how this affects the diffusional mass transport.<sup>[164]</sup>

Experimental SECM approach curves were performed on NPG layers of 160  $\mu\text{m}$  thickness with ascorbic acid as irreversible mediator<sup>[171]</sup> so that the current at the ME corresponds to the hindered diffusion only. The oxidation of ascorbic acid at the ME is a chemically irreversible electrode reaction. Therefore, no back reaction occurs at the substrate irrespective of its chemical nature. The information from this experiment characterizes the geometric properties only and are equally applicable to conductive and insulating porous layers. This approach is important for NPG because the use of conventional mediators with the possibility of a back reaction at the porous electrode would otherwise induce a concentration cell situation as previously mentioned in Chapter 3. Such vertical feedback and back reaction would add many unknown parameters to the experiment that would prevent extracting information about the morphology. The NPG samples were mounted on top of the planar Au electrode which can be considered as a planar surface, preventing diffusion of ascorbic acid across the slab of NPG.

There were three different NPG disks obtained from the same alloy ( $\text{Ag}_{73}\text{Au}_{27}$ ) by different dealloying protocols and post-treatment. After dealloying, the NPG disks showed different pore diameters and residual Ag contents.  $\text{NPG}_{\text{standard}}$  was prepared by a standard dealloying protocol in perchloric acid.<sup>[170]</sup>  $\text{NPG}_{\text{fast}}$  was dealloyed at a higher anodic potential in order to achieve higher Ag dissolution rate which leads to smaller feature sizes. The third sample,  $\text{NPG}_{\text{anneal}}$  was dealloyed following the standard procedure and then thermally annealed, this coarsened the pores in the bulk material.<sup>[164]</sup>

The internal bulk structure and the outer surface (skin layer) of the NPG differ from one another, with the skin layer presenting much smaller pore and ligament sizes, the skin layer was determined to be around 150 nm in thickness by Graf et al.<sup>[170]</sup>

The data presented in Table 8 highlight significant differences in pore sizes between the skin layer and the bulk of the NPG samples, which could directly impact the material's transport properties. Notably, the  $\text{NPG}_{\text{fast}}$  sample, which was subjected to a higher anodic potential, exhibits the smallest pore sizes both, in the skin layer and in the bulk. This could lead to a higher resistance to mass

transport within the pores, potentially reducing the overall electrochemical performance for applications that rely on efficient ion transport.

Conversely, the NPG<sub>anneal</sub> sample, which underwent thermal annealing post-dealloying, shows substantially larger pores in both regions. This coarsening process likely enhances mass transport due to the increased pore size, which reduces the tortuosity of pathways within the electrode. The NPG<sub>standard</sub>, with intermediate pore sizes, provides a balance between the other two samples.

Table 8. Experimental pore diameters  $\delta_p$  in the bulk and in the skin layer for the three NPG samples used in this study.

Material	NPG <sub>standard</sub>	NPG <sub>fast</sub>	NPG <sub>anneal</sub>
skin layer $\delta_p^{[a]}$ / nm	$6 \pm 1$	$3 \pm 1$	$56 \pm 15$
bulk $\delta_p^{[b]}$ / nm	$76 \pm 16$	$9 \pm 2$	$253 \pm 44$

[a] determined by measuring pore diameters from top-view SEM images; [b] determined from bulk ligament diameters.

The distinct difference in pore sizes between the skin layer and the bulk across all samples also points to the importance of considering the hierarchical structure of NPG. The skin layer, with its much smaller pore sizes, could act as a barrier, affecting the overall permeability and diffusion rates through the electrode. Understanding the interplay between these layers is crucial for optimizing NPG for specific applications, such as sensors, catalysts, or energy storage devices. These insights underline the need for tailored fabrication processes that can precisely control pore size distribution to achieve desired performance characteristics.

## 4.2 Theory

In a previous work, Kuss et al.<sup>[165]</sup> proposed an analytical method to determine the porosity of passive porous films from SECM approach curves. It is based on Eq. (95) which was proposed by Cornut et al.<sup>[163]</sup> for normalized and dimensionless negative feedback currents  $\Psi_{\text{ins}} = i_T/i_{T,\infty}$  on flat substrates. Kuss et al. proposed a new expression  $\Psi_P$  which is a linear combination of  $\Psi_{\text{ins}}$ , namely

$$\Psi_P(L, R_g, P, L_{\text{film}}) = P \cdot \Psi_{\text{ins}}(L + L_{\text{film}}, R_g) + (1 - P) \cdot \Psi_{\text{ins}}(L, R_g) \quad (94)$$

with

$$\Psi_{\text{ins}}(L, R_g) = \frac{2.08R_g^{-0.358} \cdot \left(L - \frac{0.145}{R_g}\right) + 1.585}{2.08R_g^{k_2} \cdot (L + 0.0023R_g) + 1.57 + \frac{\ln(R_g)}{L} + \frac{\ln(R_g)}{\pi R_g} \cdot \ln\left(1 + \frac{\pi R_g}{2L}\right)} \quad (95)$$

$$L = \frac{d}{r_T} \quad (96)$$

$$L_{\text{film}} = \frac{l_{\text{film}}}{r_T} \quad (97)$$

Equation (94) represents a critical modification by Kuss et al., allowing for the incorporation of porosity into the feedback current model. This approach provides a more realistic representation of the influence of the porous structure on mass transport and electrochemical response.

The first term of the right-hand side (RHS) of Eq. (94) is the original  $\Psi_{\text{ins}}$  multiplied by the porosity  $P$ . It represents the contribution of the hindered diffusion as if the volume between the tip of the ME and the base of the porous layer ( $L + L_{\text{film}}$ ) was made entirely of the liquid electrolyte. The second term of the RHS adds the missing solid part ( $1 - P$ ) between the top of the porous layer and the ME corresponding to the solid that was not accounted for in the first term. By fitting the experimental approach curves to Eq. (94), a porosity value is obtained. If the tortuosity needs to be considered, as is the case for NPG, then the porosity can be corrected according to the following expression

$$P' = \frac{P}{\tau} \quad (98)$$

The porosity values fitted to Eq. (94), shown in Table 10, were well outside of the expected range dictated by the maximum porosity values of the NPG samples of 0.73 when considering no shrinkage and complete Ag dissolution. The expected value stems from the fact that Au and Ag have almost identical atomic volumes.<sup>[172]</sup> The discrepancy between fitted and expected porosity values suggests that the analytical model might have limitations in accurately capturing the complex transport phenomena within the porous NPG structure. The assumptions embedded in Eq. (94) and subsequent corrections may oversimplify the actual physical processes. Numerical simulations offer a detailed approach to verify the assumptions and simplifications embedded in the analytical model for  $\Psi_P$ , especially when dealing with complex porous structures like NPG. The analytical method proposed by Kuss et al.<sup>[165]</sup> approximates the SECM response into a linear combination of contributions from the porous material and the electrolyte. However, porous systems often exhibit intricate structural

features, such as variable pore sizes, tortuosity, presence of skin layers among others, which may not be fully captured by the analytical expression alone.

### 4.3 Simulation description and results

Numerical simulations offer a detailed approach to verify the assumptions and simplifications embedded in the analytical model for  $\mathcal{V}_p$ , especially when dealing with complex porous structures like NPG.

Simulations were done in a two-dimensional axisymmetric geometry. The diffusion of the mediator through the porous structure was calculated incorporating corrected porosity and effective diffusion coefficients as described by relations like Bruggeman equation.<sup>[166,167]</sup> The origin and assumptions of this correlation were revisited in detail by Tjaden et al.<sup>[167]</sup> who showed that it belongs to the family of effective medium theories designed to capture the influence of microstructural complexity on transport without resolving the full pore geometry. The correlation expresses that higher porosity leads to lower tortuosity, and therefore to more efficient transport. Its appeal lies in the fact that transport coefficients can be estimated directly from porosity values, without the need for direct tortuosity measurements, which are notoriously difficult to obtain experimentally.<sup>[173,174]</sup>

The validity of Bruggeman's approximation has been examined extensively in electrochemical porous media. Early studies of gas diffusion in glass bead packings<sup>[175]</sup> and electrolyte conductivity in dispersions of non-conducting spheres<sup>[176]</sup> already found tortuosity values close to Bruggeman's prediction. More recently, tomography-based investigations of battery electrodes demonstrated that ordered, isotropic yield tortuosity factors in good agreement with Bruggeman, whereas heterogeneous or anisotropic electrodes deviate significantly, requiring modified exponents or more sophisticated effective medium descriptions.<sup>[166,177]</sup>

Despite these limitations, the Bruggeman relation remains a widely applied and accepted first-order model in battery and fuel-cell modeling.<sup>[178–181]</sup> Its applicability is strongest for porous networks that are isotropic, homogeneous, and well connected. precisely the characteristics of NPG. The bicontinuous, ligament-pore structure of NPG is close to the idealized assumptions underlying Bruggeman's derivation.<sup>[167]</sup> Thus, while it is important to acknowledge that the correlation can underestimate tortuosity in more complex or anisotropic systems, its use for NPG provides a physically consistent and literature-supported approximation for effective transport, going beyond the idealized conditions assumed in the analytical equation of Kuss et al.<sup>[165]</sup>



### 4.3.1 Domain equations and boundary conditions

#### *Diffusion in the electrolyte (Domain I)*

Only the concentration of the irreversible mediator was explicitly calculated in a cylindrical coordinate system ( $r$  - radial coordinate,  $z$  - vertical coordinate). Diffusion is the only mode of transport as reported in section 2.1. The diffusion equation in cylindrical coordinates is given in Eq. (99), where  $c$  is the ascorbic acid concentration and  $D$  is its diffusion coefficient. As previously mentioned, to ensure that the NPG electrode does not participate in redox cycling, the irreversible mediator was chosen to prevent any reaction with the internal surface of the extended porous gold structure as in section 4.1.

$$\frac{\partial c}{\partial t} = D \left( \frac{\partial^2 c}{\partial r^2} + \frac{1}{r} \cdot \frac{\partial c}{\partial r} + \frac{\partial^2 c}{\partial z^2} \right) \quad (99)$$

#### *Microelectrode (Boundary 1)*

The ME was modeled using the concentration boundary condition.

$$c = 0 \quad (100)$$

The ME current was calculated as discussed in section 2.6.1

$$i_T = 2\pi nFD \int_{r=0}^{r=r_T} \frac{\partial c}{\partial z} r \, dr \quad (101)$$

In this case  $n = 2$  as the oxidation of ascorbic acid gives 2 electrons per molecule.<sup>[182,183]</sup>

#### *Diffusion in NPG (Domain II).*

The NPG is modeled as a homogeneous domain of normalized thickness  $L_{\text{film}}$  with an effective diffusion coefficient  $D_{\text{eff}}$  calculated using the corrected (Bruggeman) porosity  $P'$ , nominal porosity  $P$ , and tortuosity  $\tau$  as shown in Eqs. (103) - (105). The Bruggeman relation<sup>[166,167]</sup> links  $\tau$  to  $P$  for many practically relevant electrodes. These parameters are then used in the diffusion equation Eq. (102) to describe mass transport through the porous layer.  $J$  is the boundary flux of ascorbic acid.

$$P \frac{\partial c}{\partial t} = D_{\text{eff}} \left( \frac{\partial^2 c}{\partial r^2} + \frac{1}{r} \cdot \frac{\partial c}{\partial r} + \frac{\partial^2 c}{\partial z^2} \right) \quad (102)$$

$$D_{eff} = P' \cdot D \quad (103)$$

$$P' = \frac{P}{\tau} \quad (104)$$

$$\tau = P^{-\frac{1}{2}} \quad (105)$$

***Glass insulator (Boundary 2).***

A zero-flux condition is imposed on the glass sheath of the ME. This also applies to the flat Au surface below the porous film.

$$J = 0 \text{ mol m}^{-2}\text{s}^{-1} \quad (106)$$

***Bulk (Boundary 3).***

$$c = c^* \quad (107)$$

**4.3.2 Sensitivity to the angle  $\alpha$  between the microelectrode plane and the sidewall of the insulating sheath of the microelectrode**

In order to evaluate how geometrical details influence the simulation output, the angle  $\alpha$  between the plane of the ME and the side walls of its insulating sheath was systematically varied. Table 9 shows a sensitivity analysis for this parameter. As indicator, the normalized currents are reported at  $d = 1 \text{ }\mu\text{m}$  above a film of  $l_{film} = 150 \text{ }\mu\text{m}$  (close to condition of infinite film thickness) and two  $R_g$  values. The shaded field in the table highlights the entries in which the relative deviation from the values calculated for  $\alpha = 90^\circ$  is smaller than 2%, an accuracy that seems more than enough for most problems. The deviation increases with decreasing  $R_g$ . However, even for  $R_g = 2$  a variation of  $\alpha$  between  $90^\circ$  and  $120^\circ$  is tolerated within the 2% interval.

Table 9. Sensitivity analysis for parameter  $\alpha$  (see Figure 34). Other parameter were  $d = 1 \text{ }\mu\text{m}$  ( $L = 0.04$ ),  $l_{film} = 150 \text{ }\mu\text{m}$  ( $L_{film} = 6$ ).

$\alpha$	$\Psi_{sim}(R_g = 2)$	$\Psi_{sim}(R_g = 5)$
90	0.811	0.794
95	0.810	0.794
100	0.807	0.792

$\alpha$	$\Psi_{\text{sim}}(R_g = 2)$	$\Psi_{\text{sim}}(R_g = 5)$
105	0.805	0.791
110	0.802	0.790
115	0.799	0.788
120	0.795	0.786
125	0.790	0.783
130	0.785	0.780
135	0.779	0.776
140	0.771	0.772

After carrying out the parametric study regarding porosity in COMSOL and comparing the results with the experimental curves (shown in Figure 36), the determined values for  $\text{NPG}_{\text{standard}}$ ,  $\text{NPG}_{\text{fast}}$ , and  $\text{NPG}_{\text{anneal}}$  are much closer to the expected porosity than the porosity derived from fitting the value to Eq. (94).<sup>[165]</sup>

Table 10. Porosity comparison for the three NPG samples according to the simulation and fitting of analytical Eq. (94).<sup>[165]</sup> The porosity was corrected according to the Bruggeman relation.<sup>[166,167]</sup>

	$\text{NPG}_{\text{standard}}$	$\text{NPG}_{\text{fast}}$	$\text{NPG}_{\text{anneal}}$
$P_{\text{simulation}}$	0.70	0.61	0.75
$P_{\text{fit}}$	0.77	0.62	0.83

By looking at the difference in the simulation results and the analytical fits an effort was made to come up with a more precise analytical model that would accurately describe the diffusive transport through porous networks in SECM approach curves.

To achieve this, the first step was to generate a large database of simulated approach curves covering a wide range of possible working conditions in a realistic experimental setup. A MATLAB (MathWorks, Natick, MA, USA) script was written (See Appendix 7.3) to automate over 200,000 simulation points covering the parameters which appear in the analytical model, namely:  $L$  (0 – 40),  $R_g$  (1.1 – 20),  $P$  (0.25 – 0.75),  $L_{\text{film}}$  (1.2 – 20).

The calculation was carried out on a personal computer (Xeon 3.6 GHz, 32 Gb RAM. Windows 7). Calculation of one data point took between seconds to several minutes depending on the specific combination of  $L$ ,  $R_g$ ,  $P$ , and  $L_{\text{film}}$ .

Once the database of the simulations was created, a parameter fitting was conducted using the multi-variable nonlinear curve-fitting function (*lsqcurvefit*) from the optimization toolbox in MATLAB. The goodness of fit was quantified by the sum of squared residuals (*SSR*) provided by the output of the *lsqcurvefit* function. This value corresponds to the sum of squared differences between all simulated points (dimensionless current  $\Psi_{\text{sim}}$ ), taken as the exact value, and an analytical equation  $\Psi_{\text{fit}}$ . Both  $\Psi_{\text{sim}}$  and  $\Psi_{\text{fit}}$  represent dimensionless ME currents, defined as the ratio of the simulated current  $i_T$  to the steady-state current  $i_{T,\infty}$  at infinite distance from a planar, non-reactive substrate.

$$SSR = \sum \left( \Psi_{\text{fit}}(L, R_g, P, L_{\text{film}}) - \Psi_{\text{sim}} \right)^2 \quad (108)$$

Eq. (94) provides a correct description for the limiting cases  $P = 0$  and  $P = 1$ , which correspond to negative feedback cases on flat substrates at different distances,  $L$  for  $P = 0$  and  $L + L_{\text{film}}$  for  $P = 1$ . By analyzing the *SSR* with Eq. (94)<sup>[165]</sup> as  $\Psi_{\text{fit}}$  over a wide range of parameters it became clear that the equation produces excellent agreements when  $L_{\text{film}} \leq 1$ . This makes sense in the context that the equation is built around an analytical model for flat electrodes and at  $L_{\text{film}} \leq 1$  the influence of the porous layer is not that large in which its contribution is sufficiently accounted for by the linear combination of the two terms corrected by  $P$  and  $1-P$ .

It was not possible to come up with an equation with the same range of applicability and accuracy of Eq. (95), which is all values of  $L$  and  $R_g < 200$ , while at the same time adding the full range of porosity (0-1) and thickness (0- $\infty$ ) for porous layers  $L_{\text{film}}$ . After evaluating different forms for a new analytical equation, the simplicity and logic behind Eq. (94) seemed to deliver the best results albeit with different constants between both terms.

$$\Psi_{\text{fit}}(L, R_g, P, L_{\text{film}}) = P \cdot \Psi_1(L + L_{\text{film}}, R_g) + (1-P) \cdot \Psi_2(L, R_g) \quad (109)$$

$$\Psi_i(L, R_g) = \frac{k_{1,i} R_g^{k_{2,i}} \cdot \left( L - \frac{k_{3,i}}{R_g} \right) + k_{4,i}}{k_{1,i} R_g^{k_{2,i}} \cdot \left( L + k_{5,i} R_g \right) + k_{6,i} + \frac{\ln(R_g)}{L} + \frac{\ln(R_g)}{\pi R_g} \cdot \ln\left(1 + \frac{\pi R_g}{2L}\right)} \quad (110)$$

$$i = 1, 2$$

Table 11.  $k$ -values for  $\Psi_{\text{ins}}$ ,  $\Psi_1$ , and  $\Psi_2$  for Eq. (109).

	$\Psi_{\text{ins}}$ <sup>[a]</sup>	$\Psi_1$ <sup>[b]</sup>	$\Psi_2$ <sup>[b]</sup>
$k_1$	2.08	2.107	4.293
$k_2$	-0.358	-0.592	-0.433
$k_3$	0.145	0.181	0.212
$k_4$	1.585	1.613	2.824
$k_5$	0.0023	0.0000	0.0000
$k_6$	1.57	1.353	3.287

<sup>[a]</sup> from Cornut and Lefrou<sup>[184]</sup>, <sup>[b]</sup> by fitting over 200 000 simulated  $\Psi_{\text{fit}}$  values to Eq. (109).

By using Eq. (109) with two different normalized current contributions  $\Psi_1$  and  $\Psi_2$  and refitted numerical constants (Table 11), the *SSR* of the modified expression was over six times smaller (Table 12) than for Eq. (94) in the intervals:

- Ratio of radii of glass sheath and ME ( $R_g$ ): 1.1-20
- Dimensionless film thickness ( $L_{\text{film}}$ ): 1.2-20
- Porosity ( $P$ ): 0.25-0.75

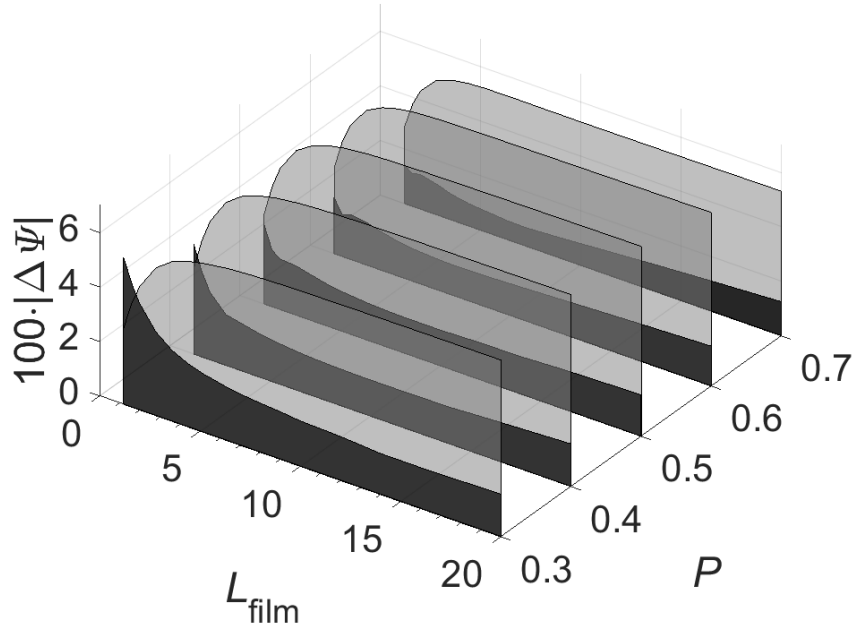


Figure 35. Absolute deviation  $\Delta\Psi$  between the simulated normalized ME current  $\Psi_{\text{sim}}$  vs. analytical approximation  $\Psi_{\text{fit}}$  in Eq. (109) (black) and Eq. (94) (light grey) against the simulated film thickness and porosity for  $R_g = 5$ . Figure taken from own publication.<sup>[164]</sup>

Figure 35 shows the absolute maximum deviation per approach curve at a range of  $L_{\text{film}} = 1.2, \dots, 20$ ;  $P = 0.3, \dots, 0.7$  and  $R_g = 5$  of both analytical expressions.  $R_g = 5$  was selected as a representative value for  $R_g$  as overall variation in  $R_g$  has a lower influence than the variation of  $L_{\text{film}}$  and  $P$ . The tendency confirms that when the contribution of the porous film is small (thin porous film and low porosity), Eq. (94)<sup>[165]</sup> delivers excellent results (light grey area, lower left). When  $L_{\text{film}}$  becomes larger its contribution slightly increases and Eq. (109) delivers consistently more accurate current values than Eq. (94).<sup>[165]</sup>

Table 12. SSR values from fitting 207,807 simulation points.

SSR from Fit Eq. (109)	SSR from Fit Eq. (94)
20.13	123.55

### 4.3.3 Determination of porosity

This section investigates whether the newly proposed analytical model, Eq. (109), can more accurately determine porosity values by comparing its output against simulations and experimental

SECM approach curves. Experimental, simulated and fitted approach curves are compared in Figure 36 and the porosity values fitted from both analytical equations are shown in Table 13.

To avoid possible confusion, it should be noted that the reported values correspond to the nominal porosity  $P$ , which was estimated using the Bruggeman relation to account for tortuosity effects. The Bruggeman relation does not define a separate porosity type but provides an approximation for  $P$  based on transport behavior.

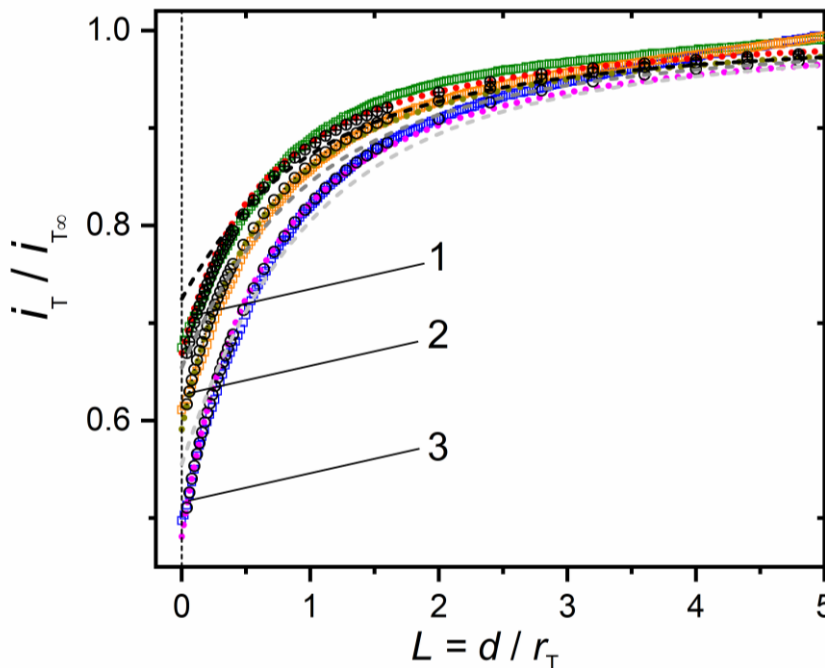


Figure 36. Comparison of experimental SECM approach curves (colored symbols), simulations (black symbols) and analytical approximation according to Eq. (109) (dotted lines) and Eq. (94) (dashed lines) for 1)  $\text{NPG}_{\text{fast}}$ ; 2)  $\text{NPG}_{\text{standard}}$ ; 3)  $\text{NPG}_{\text{anneal}}$ . Figure taken from own publication and slightly modified.<sup>[164]</sup>

Aside from delivering fitted porosity values which are closer to the simulated ones (see Table 14), Eq. (109) also better reproduces the overall shape of the simulation curve compared to Eq. (94).<sup>[165]</sup> In the three approach curves shown, Eq. (94),<sup>[165]</sup> overestimates the simulated current at very small  $L$  values, while it begins to slightly underestimate it as  $L$  increases. This reinforces the idea that the influence of the porous layer cannot be accurately approximated by a linear combination of the equation describing classical negative feedback approach curves.

## Homogeneous model of passive porous substrates

Table 13. Comparison of corrected porosity values  $P$  for the three NPG samples according to the simulation and fitting of analytical Eqs. (94)<sup>[165]</sup> and (109). The porosity was corrected according to the Bruggeman relation.<sup>[166,167]</sup>

	NPG <sub>standard</sub>	NPG <sub>fast</sub>	NPG <sub>anneal</sub>
$P_{\text{simulation}}$	0.70	0.61	0.75
$P_{\text{fit}}^{[a]}$	0.77	0.62	0.83
$P_{\text{fit}}^{[b]}$	0.71	0.62	0.77

<sup>[a]</sup> according to Eqs. (94); <sup>[b]</sup> according to Eq. (109).

Aside from fitting the experimental curves, simulations were run with a fixed porosity  $P = 0.7$  and increasing film thickness  $L_{\text{film}}$ . The results are shown in Table 14. Both approximations yield  $P$  values in a narrow interval. In case of Eq. (109), the interval encloses the values  $P = 0.70$  used in the simulation while this is not the case for Eq. (94).

Table 14. Fitting of simulated approach curves to Eq. (109) or Eq. (94)<sup>[165]</sup> assuming a known film thickness and using  $P$  as adjustable parameter. Simulated film thickness in column 1 with  $P = 0.70$ .

$L_{\text{film}}$	$P$ from Fit Eq. (109)	$P$ from Fit Eq. (94)
1.2	0.700	0.740
1.6	0.706	0.747
2.0	0.708	0.749
2.8	0.707	0.749
3.6	0.705	0.747
4.4	0.703	0.746
5.2	0.702	0.745
6.4	0.702	0.742
7.2	0.702	0.741
8.0	0.702	0.741
9.2	0.702	0.734
10	0.703	0.741
12	0.704	0.733
14	0.706	0.740
16	0.706	0.733
20	0.709	0.738

#### 4.3.4 Determination of layer thickness

Simulations were further used to evaluate the ability of the analytical models to estimate the thickness of the porous film layer when the porosity is known. A total of 16 approach curves were simulated with  $P = 0.70$  for normalized distances  $L_{\text{film}}$  between 1.2 and 20. These simulated curves were then fitted using both Eq. (94)<sup>[165]</sup> and Eq. (109), treating  $L_{\text{film}}$  as the adjustable parameter.

The results are summarized in Table 15. As expected, accurate estimation of film thickness is only possible for relatively thin films. Beyond  $L_{\text{film}} \approx 6$ , the feedback current becomes nearly insensitive to further changes in thickness, limiting the accuracy of any fitting. This phenomenon is reflected in the simulation results: Eq. (109) maintains a low error for  $L_{\text{film}} \leq 6.4$ , while Eq. (94)<sup>[165]</sup> begins to deviate significantly already for smaller values of  $L_{\text{film}}$ .

In the fitting algorithm, an upper limit for plausible film thicknesses was set to  $L_{\text{film}} = 500$ . The values  $L_{\text{film}} = 500$  shown in column 3 of 500 are therefore just placeholder values indicating a complete loss of reliability in the parameter estimation.

This analysis also highlights a key limitation. For very thick, porous layers, film thickness cannot be reliably extracted using the current analytical models. For such cases, complementary simulation-based methods may be more appropriate.

Table 15. Fitting of simulated approach curves to Eq. (109) and Eq. (94)<sup>[165]</sup> assuming a known porosity  $P = 0.70$  and using the film thickness as adjustable parameter. Simulation with the film thickness in column 1  $P = 0.70$ .

$L_{\text{film}}$ simulation	$L_{\text{film}}$ fit Eq. (109)	$L_{\text{film}}$ fit Eq. (94)
1.2	1.20	1.35
1.6	1.63	1.92
2.0	2.06	2.56
2.8	2.90	4.15
3.6	3.72	6.45
4.4	4.54	10
5.2	5.36	20
6.4	6.68	164
7.2	7.67	500.00

$L_{\text{film}}$ simulation	$L_{\text{film}}$ fit Eq. (109)	$L_{\text{film}}$ fit Eq. (94)
8.0	8.83	500.00
9.2	11	500.00
10	103	500.00
12	28	500.00
14	25	500.00
16	22	500.00
20	21	500.00

The results confirm that Eq. (109) provides significantly improved fitting performance compared to Eq. (94)<sup>[165]</sup>, especially for moderately thick films. Within the valid range, Eq. (109) not only delivers more accurate estimates of  $L_{\text{film}}$  but also tracks the simulated approach curves more closely. This underscores the utility of Eq. (109) for extracting film thickness values from SECM data, provided that the measurement conditions fall within the range of sensitivity. The green field in Table 15 indicate conditions under which the error in  $L_{\text{film}}$  remains below 5%.

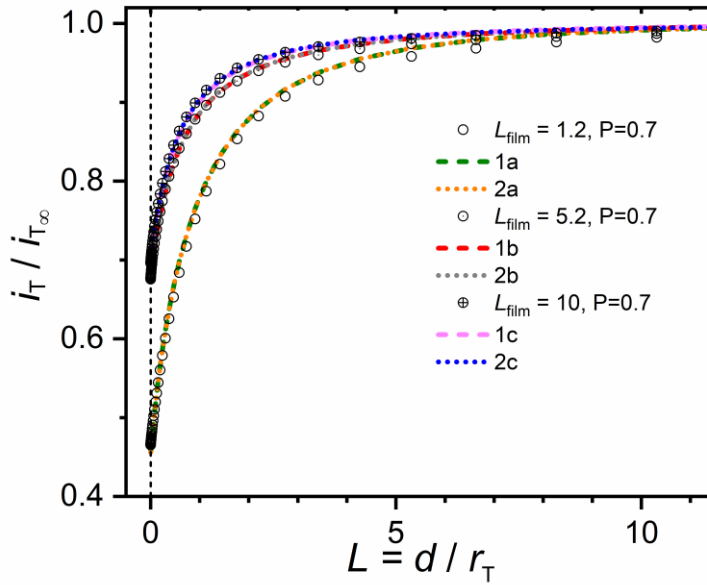


Figure 37. Simulated approach curves (O) for  $P = 0.70$  with  $L_{\text{film}}$  of a) 1.2, b) 5.2 and c) 10 together with different fits of Eq. (109) to the same simulated data. Curves 1a to 1c represent fits where the film thickness is known, and  $P$  is adjusted;  $P_{1a} = 0.700$ ,  $P_{1b} = 0.702$ ,  $P_{1c} = 0.703$ . Curves 2a to 2c are fits where  $P$  is known, and the film thickness is adjusted;  $L_{\text{film},2a} = 1.2$ ,  $L_{\text{film},2b} = 5.36$ ,  $L_{\text{film},2c} = 103$ . Figure taken from own publication and slightly modified.<sup>[164]</sup>

Figure 37 illustrates three representative cases from the simulations ( $L_{\text{film}} = 1.2, 5.2, 10$ ) where either  $P$  or  $L_{\text{film}}$  was held constant during fitting. The results clearly show that  $P$  can be fitted with high precision across all cases, while accurate estimation of  $L_{\text{film}}$  deteriorates significantly for thicker films.

#### 4.3.5 Determination of porosity and film thickness simultaneously

This section evaluates the feasibility and limitations of simultaneously fitting both porosity  $P$  and normalized film thickness  $L_{\text{film}}$  from SECM approach curves using the analytical models. While earlier sections demonstrated the independent fitting of these parameters with high accuracy within specific ranges, their concurrent fitting poses a more complex challenge due to their interdependent influence on the feedback current.

To investigate this, SECM approach curves were simulated using fixed input parameters ( $P = 0.70$ ,  $L_{\text{film}}$  from 1.2 to 20), and both  $P$  and  $L_{\text{film}}$  were treated as adjustable parameters during fitting with Eq. (94)<sup>[165]</sup> and Eq. (109). The results, summarized in Table 14, show that Eq. (109) can yield reasonably accurate results within the range  $1 \leq L_{\text{film}} \leq 6.4$ , with errors for both  $P$  and  $L_{\text{film}}$  remaining below 15%. In contrast, Eq. (94)<sup>[165]</sup> exhibits poor performance even within this favorable range, producing significantly biased values for both parameters.

Table 16. Fitting of simulated approach curves to Eq. (109) or Eq. (94)<sup>[165]</sup> using the porosity  $P$  and the film thickness  $L_{\text{film}}$  as adjustable parameters. Simulation with the film thickness in column 1 and  $P = 0.70$ .

$L_{\text{film}}$ simulation	$P$ fit Eq. (109)	$L_{\text{film}}$ fit Eq. (109)	$P$ fit Eq. (94)	$L_{\text{film}}$ fit Eq. (94)
1.2	0.728	1.12	0.528	3.39
1.6	0.727	1.50	0.587	4.06
2.0	0.726	1.87	0.623	4.92
2.8	0.719	2.61	0.662	7.12
3.6	0.713	3.38	0.681	9.97
4.4	0.708	4.20	0.694	13
5.2	0.704	5.11	0.702	18
6.4	0.699	6.81	0.710	27
7.2	0.696	8.60	0.714	37
8.0	0.698	500	0.717	52
9.2	0.700	280	0.715	500
10	0.703	235	0.723	91

$L_{\text{film}}$ simulation	$P$ fit Eq. (109)	$L_{\text{film}}$ fit Eq. (109)	$P$ fit Eq. (94)	$L_{\text{film}}$ fit Eq. (94)
12	0.703	46	0.721	500
14	0.706	41	0.729	500
16	0.706	25	0.725	500
20	0.709	22	0.732	500

These findings confirm that while Eq. (109) offers a marked improvement over Eq. (94),<sup>[165]</sup> the simultaneous determination of  $P$  and  $L_{\text{film}}$  is only reliable within a narrow window of the parameter space. Beyond  $L_{\text{film}} \approx 6.4$ , the similarity in how  $P$  and  $L_{\text{film}}$  affect the shape of the approach curve leads to strong parameter correlation. This correlation makes it difficult to uniquely identify both values from the same dataset.

Thus, although Eq. (109) improves the robustness of the analysis, fundamental limitations remain when attempting to extract both porosity and thickness from a single SECM experiment. These results underscore the importance of combining analytical fits with complementary simulations or experimental constraints when characterizing porous films in SECM.

#### 4.3.6 Influence of skin layer.

Simulations were conducted to evaluate the influence of the experimentally observed skin layer (Boundary 4 in Figure 34) on the transport properties of NPG samples. The skin layer, characterized by significantly smaller pore and ligament sizes compared to the bulk, can act as a thin diffusion barrier between the NPG domain and the electrolyte. To accurately represent this feature, a thin diffusion barrier was incorporated into the simulation model without meshing an extremely thin domain, which could complicate the computational model.

As seen in Figure 38, the skin layer forms a compact surface zone distinct from the bulk morphology. This microstructural contrast justifies its separate treatment in the simulation model as a thin diffusive barrier with modified transport properties.

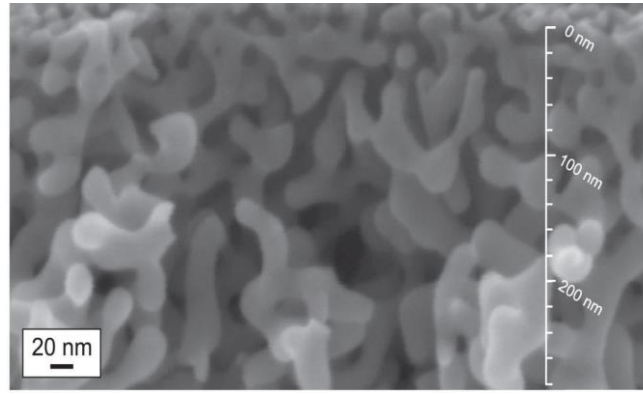


Figure 38. Cross-sectional SEM image of a NPG sample showing the surface "skin layer" with significantly smaller pores compared to the bulk. The image highlights the structural difference between the thin top layer and the deeper porous region. Taken from Graf et al.<sup>[170]</sup>

Flux equations were solved from both sides of the skin layer (up and down subscripts). Instead of meshing an extremely thin domain, the length of the skin layer is incorporated into the flux equation itself, and the flux is calculated according to Eq. (111) and Eq. (112).

$$J_{\text{up}} = \frac{D_{\text{SL}}}{l_{\text{SL}}} \cdot (c_{\text{down}} - c_{\text{up}}) \quad (111)$$

$$J_{\text{down}} = \frac{D_{\text{SL}}}{l_{\text{SL}}} \cdot (c_{\text{up}} - c_{\text{down}}) \quad (112)$$

$$\text{with } D_{\text{SL}} = P_{\text{SL}} \cdot D, \quad P_{\text{SL}} = \frac{P}{\tau} \quad \text{and} \quad \tau = P^{-\frac{1}{2}}$$

Here  $c_{\text{down}}$  and  $c_{\text{up}}$  are the concentrations of the diffusing species on either side of the skin layer. The variable  $D_{\text{SL}}$  is effective diffusion coefficient in the skin layer,  $P_{\text{SL}}$  is the porosity of the skin layer calculated using the Bruggeman relation,<sup>[166,167]</sup> as in the previous section,  $P$  is the nominal porosity,  $l_{\text{SL}}$  is the skin layer thickness.

This approach maintains computational efficiency while allowing for an accurate representation of hindered diffusion across the skin layer. The results from these simulations provide insight into the degree to which this structurally distinct layer influences the overall transport behavior in SECM measurements.

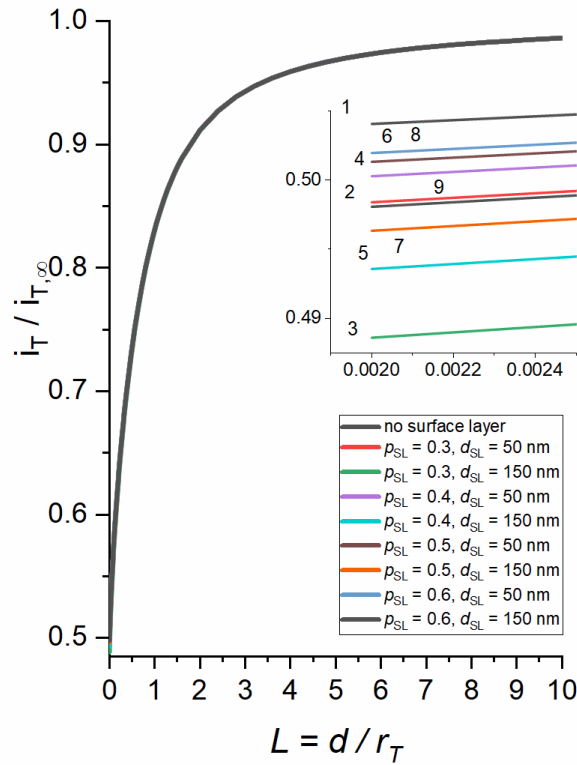


Figure 39. Simulated approach curves with a microelectrode of  $r_T = 25 \mu\text{m}$  considering the influence of the skin layer. The simulated sample has a thickness of  $160 \mu\text{m}$  and the bulk porosity  $P$  of the sample is 0.6 for all cases. (1) Without surface layer, (2)  $P_{\text{SL}} = 0.3$  and  $L_{\text{SL}} = 50 \text{ nm}$ , (3)  $P_{\text{SL}} = 0.3$  and  $L_{\text{SL}} = 150 \text{ nm}$ , (4)  $P_{\text{SL}} = 0.4$  and  $L_{\text{SL}} = 50 \text{ nm}$ , (5)  $P_{\text{SL}} = 0.4$  and  $L_{\text{SL}} = 150 \text{ nm}$ , (6)  $P_{\text{SL}} = 0.5$  and  $L_{\text{SL}} = 50 \text{ nm}$ , (7)  $P_{\text{SL}} = 0.5$  and  $L_{\text{SL}} = 150 \text{ nm}$ , (8)  $P_{\text{SL}} = 0.6$  and  $L_{\text{SL}} = 50 \text{ nm}$ , (9)  $P_{\text{SL}} = 0.6$  and  $L_{\text{SL}} = 150 \text{ nm}$ . Figure taken from own publication and slightly modified.<sup>[164]</sup>

Figure 39 includes an inset showing a zoomed-in region of the approach curves at very short distances from the substrate. While the curves are virtually indistinguishable over the full range, minor but systematic deviations become apparent in the magnified inset for very small  $L$ . Even with a skin layer thickness of up to  $150 \text{ nm}$  and a porosity as low as 0.3 (as observed in SEM images by Graf et al.,<sup>[170]</sup> the resulting change in current remains below 2%. Thus, the influence of the skin layer on SECM approach curves is negligible under typical experimental conditions, supporting the use of simplified models without extensive correction for this morphological feature.

## 4.4 Conclusions

This chapter introduced a new analytical equation [Eq. (109)] for SECM approach curves on passive porous substrates, aimed at accurately determining transport properties such as porosity (including

tortuosity) and film thickness of porous layers. Equation (109) successfully expands the range of applicability of the equation proposed by Kuss et al.<sup>[165]</sup> by accommodating a wider set of experimental conditions, including variations in the ratio of sheath to electrode radii ( $R_g$ ), porosity, and film thickness. This broader parameter range ensures that Eq. (109) can be utilized in most practical SECM setups, enhancing its utility in real-world applications. Nonetheless, an ideal model would be valid over the entire range of porosity  $P = [0,1]$ , which Eq. (109) does not fully achieve. This highlights an ongoing need for refinement, particularly in extending the model's applicability to encompass extreme porosity values.

One notable drawback of Eq. (109) is its reliance on ten numerical parameters, compared to the six parameters in Eq. (94) by Kuss et al.<sup>[165]</sup>. While this increase in the number of parameters improves the model's accuracy, it introduces additional complexity, which can be seen as a nuisance in terms of computational efficiency and simplicity. A more streamlined equation with fewer numerical parameters would be desirable, as it would reduce computational demand and simplify the fitting process.

The structure of Eq. (109) is based on a linear combination of terms derived from the analytical equation for negative feedback SECM experiments on flat substrates. This approach may inherently limit the accuracy of the model, as it suggests that the linear combination cannot fully capture the complexity of the porous systems. A closer examination reveals that the parameters associated with the first term of Eq. (109) closely resemble those used in Eq. (94),<sup>[165]</sup> indicating a reasonable consistency. In contrast, the parameters  $k_{2,i}$  for the second term are heavily corrected, which suggests that the second term might be the primary source of inaccuracy. Therefore, a targeted reformulation of the second term could potentially enhance the overall accuracy of Eq. (109).

Additionally, it is important to note the challenges associated with simultaneously fitting porosity ( $P$ ) and film thickness ( $L_{\text{film}}$ ) using either Eq. (109) or Eq. (94). The influence of changing both parameters on the feedback current ( $\mathcal{P}$ ) is often too similar, leading to ambiguous results when both parameters are adjusted simultaneously. This overlap in influence underscores the importance of separating the effects of porosity and thickness during analysis or applying the model only within specific ranges where this overlap is minimized.

When accuracy requirements are relaxed, Eq. (109) may still provide indicative values for film thicknesses in the range of  $1 \leq L_{\text{film}} \leq 6.4$ . However, for precise characterization, it remains essential

to be cautious with parameter fitting, particularly when dealing with broader or more complex experimental conditions.

Another possible approach to overcome the limitation of fitting porosity and film thickness simultaneously could involve time-resolved SECM measurements, such as chronoamperometric experiments at various distances from the substrate. In such dynamic setups, film thickness is expected to influence the delay between a perturbation (such as the sudden change of the ME potential) and the onset of a measurable current change. This delay occurs because a thicker film extends the distance that the redox mediator must diffuse through before reaching the electrode, effectively introducing a lag in the response of the system. In contrast, porosity affects the internal diffusion resistance of the porous medium. A lower porosity means that the effective diffusivity is reduced, causing the system to take longer to reach steady-state even after the initial response has begun. In other words, film thickness should control how long it takes for the response to register while porosity should determine how quickly the current approaches its final steady-state value after that initial delay. These distinct temporal effects could potentially be leveraged to decouple the influence of porosity and thickness, although this would require further theoretical development and experimental validation to determine the robustness and sensitivity of such an approach.

## 5. Current density distribution on Li electrodes combined with an SECM probe

The performance and safety of lithium metal and lithium-ion batteries are closely tied to the properties of the solid electrolyte interphase (SEI), which forms on the anode surface during initial charging cycles. The SEI plays a critical role by passivating the surface for electron transfer reaction while maintaining lithium-ion conductivity.<sup>[185]</sup> However, its structure and function remain incompletely understood due to its dynamic, heterogeneous, and nanoscale nature. As the SEI evolves during cycling, it affects lithium nucleation, dendrite formation, and coulombic efficiency.<sup>[186]</sup> Understanding the spatial and temporal evolution of the SEI under realistic operating conditions is essential for the rational design of stable lithium electrodes. The SEI helps to protect the lithium metal anode and the lithium-ion cathode from degradation extending the lifespan of the battery. However, the SEI has the potential to impede the diffusion of lithium ions, leading to a reduction in both the battery's capacity and rate performance. There are numerous reactions occurring at the electrode surface, that result in the formation of insoluble and partially soluble reduction products of electrolyte decomposition.<sup>[187]</sup> The analysis of the SEI composition in an ex-situ setting may present challenges due to potential changes of the SEI during the transfer process. While in-situ techniques such as electrochemical impedance spectroscopy (EIS) provide valuable functional information of the SEI and its impact on battery performance and stability, the signals obtained through EIS are integrated over the entire surface, making it difficult to investigate local properties.<sup>[188]</sup> SECM has been used to study local electron transfer properties of SEI.<sup>[189,190]</sup> Research in the Wittstock group aims for conducting such studies under near operando conditions.<sup>[191]</sup>

The aim of this study is to evaluate whether the presence of an SECM microelectrode affects the current distribution at lithium electrodes during galvanostatic cycling, and whether the observed SECM signals are representative of the actual electrochemical behavior of the system.

The simulations are intended to serve as a guideline for experimenters using SECM under operando conditions. Specifically, the study aims to determine whether it is valid to interpret charge–discharge processes at the sample surface while the ME remains in its imaging position. The analysis thus addresses a critical experimental question: to what extent does the presence of the ME perturb the electrochemical environment during realistic operating conditions?

The experimental setup, including the in situ SECM-compatible electrochemical cell, was developed and implemented by Bastian Krueger, while the finite element simulations and the analysis of current

distributions were carried out by the author of the thesis. The results were published and form the foundation of the modeling strategy presented in this chapter.<sup>[191]</sup>

## 5.1 Theoretical background

### 5.1.1 Solid electrolyte interphase

Metallic lithium is an attractive anode material due to its favorable thermodynamic properties, combining a highly negative standard electrode potential with a low equivalent weight. In most regularly used battery electrolytes, metallic lithium leads to thermodynamic instability due to its strong reducing capability, however in a suitable electrolyte, films of electrolyte decomposition products form as soon as the electrode comes in contact with the electrolytic solution, just as expected from the SEI behavior.<sup>[187,192]</sup> Commercial breakthrough of metallic lithium anodes in rechargeable batteries has so far failed, as during the recharge process in liquid electrolytes lithium plating occurs concurrently along lithium corrosion and passivation (SEI formation). The resulting SEI is inhomogeneous in composition and thickness which impedes a smooth deposition through the SEI and instead causes the formation of highly reactive dendritic material which at the same time function as substrate for further inhomogeneous SEI formation.<sup>[193]</sup>

While this thesis focuses on lithium metal electrodes, SEI is also central in lithium-ion batteries. In such systems, the SEI forms on graphitic (or other intercalation) anodes and fulfills a similar dual role of electronically insulating the electrolyte while maintaining  $\text{Li}^+$  conduction.<sup>[194,195]</sup> However, there are important distinctions. The SEI on graphite typically develops under less extreme reducing conditions compared to metallic lithium, resulting in comparatively thinner and more stable films. In contrast, the SEI on lithium metal must withstand repeated plating/stripping and large volume changes, which often leads to inhomogeneity, cracking, and dendrite growth.<sup>[185]</sup> Thus, while the general principles of SEI passivation and ionic conduction apply in both systems, the mechanical and morphological challenges are far more pronounced for Li metal.

The performance and stability of the electrode in lithium metal systems depend on the properties of the SEI. The SEI must simultaneously provide passivation to prevent continuous electrolyte reduction by blocking electron transfer, and ionic transport as to permit  $\text{Li}^+$  conduction to enable plating and stripping.<sup>[192]</sup> To fulfill these dual functions, it should exhibit very low electronic conductivity while maintaining sufficient ionic conductivity for  $\text{Li}^+$  transport.<sup>[185,192]</sup> Moreover, mechanical robustness is essential, as the Li electrode undergoes volume changes during cycling, the SEI must retain integrity, avoid crack formation, and suppress dendrite penetration.<sup>[192,196]</sup> A robust SEI structure

combining these traits of electron insulation, ion conduction, and mechanical stability is thus central to enabling high-efficiency and safe cycling of lithium metal anodes.

The SEI on lithium metal forms spontaneously during the first contact with the electrolyte, as electrolyte components are reduced at potentials close to the  $\text{Li}^+/\text{Li}$  couple. This self-limiting decomposition produces an ultrathin film, typically on the order of tens of nanometers, that contains inorganic species such as  $\text{Li}_2\text{O}$ ,  $\text{LiF}$ , and  $\text{Li}_2\text{CO}_3$  near the electrode and organic fragments toward the electrolyte side.<sup>[187,197]</sup> The composition of the SEI is still a subject of debate, with a wide range of components having been reported.<sup>[198–205]</sup> The organic components of the SEI are believed to be penetrated by electrolyte and jellified, forming a medium through which lithium cations can be transported. The inorganic components, on the other hand, are more stable against reduction relative to the anode material and are likely to be located closer to the electrode surface. It is thought that the inorganic components contribute to the protective properties of the SEI, which help to prevent degradation of the battery.<sup>[193]</sup>

As the SEI is of critical importance for the proper operation, longevity and safety of lithium metal and lithium-ion batteries, several *ex-situ* and *in situ* techniques have been developed. *Ex-situ* techniques include X-ray photoelectron spectroscopy,<sup>[206]</sup> secondary ion mass spectrometry,<sup>[187,202]</sup> and transmission electron microscopy,<sup>[207]</sup> which provide insights into the chemical composition and the morphology of the SEI. However, as already mentioned, the SEI keeps changing in its chemistry and properties throughout the battery's lifetime, making *in-situ* and operando studies become increasingly relevant.<sup>[187]</sup> Such studies allow observation of the SEI in electrolytes of even under realistic operating conditions, even though many mechanistic details remain poorly understood.

The Wittstock group introduced a setup in which SECM was used to evaluate the evolution of incipient SEI layers on monocrystalline silicon electrodes by *in-situ* imaging of their passivating properties.<sup>[208]</sup> This was conducted at a potential positive to where the lithiation takes place to avoid the associated severe morphological changes in the SEI layer which greatly complicate the interpretation of the measured currents. An important drawback of the study was that the current densities were far below those present in real batteries. To overcome this, a new experimental setup was developed in the Wittstock group in which metallic lithium electrodes could be investigated with SECM under realistic current densities for electrochemical dissolution and deposition.<sup>[191]</sup>

A lithium working electrode (WE) with a size of  $12 \times 12$  mm was mounted opposite a lithium counter electrode (CE) with a  $4 \times 4$  mm central aperture to allow the ME to approach the WE during the

SECM measurements. During galvanostatic charge–discharge cycles, the tip was retracted and SECM imaging was performed only in between cycles. The electrolyte consisted of 1 M LiClO<sub>4</sub> in propylene carbonate, present in excess with a conductivity of 1.1 S m<sup>-1</sup>.<sup>[209]</sup> Galvanostatic currents up to 4 mA ( $\approx 2.8 \text{ mA cm}^{-2}$ ) were applied. The corresponding overpotentials ( $\approx 0.2 - 0.38 \text{ V}$ ) confirmed that the system operated in a realistic range. These parameters and procedural constraints guided the geometry, boundary conditions, and current distribution modelling in the simulations presented below.

### 5.1.2 Current density distributions

In modeling such systems, it is essential to distinguish between primary, secondary, and tertiary current distributions, each reflecting a different set of assumptions about the dominating transport and interfacial processes. These classifications guide the level of complexity needed to accurately simulate electrochemical behavior as outlined by Newman and Balsara.<sup>[210]</sup>

The primary current distribution assumes infinitely fast electrode kinetics, meaning that the electrode overpotential vanishes and the entire electrode surface remains at the same potential. The current distribution is governed purely by the solution resistance and the geometry of the electrodes. In this regime, the Laplace equation is solved for the electrolyte potential, typically under Neumann boundary conditions that enforce a fixed total current. Neither activation overpotentials nor concentration gradients are considered. This approximation is useful as a baseline, particularly in processes dominated by geometric effects, such as electroplating.

However, in systems involving lithium metal electrodes, kinetic limitations are significant. Lithium exhibits relatively low exchange current densities, typically in the range of 0.01 to 1 mA·cm<sup>-2</sup>,<sup>[211–214]</sup> Since the applied current densities in this study are on the same order of magnitude as these in real cells, the system operates in a regime where charge-transfer kinetics limit the interfacial reaction rate, and the activation overpotential becomes significant. Therefore, the secondary current distribution model, which incorporates finite kinetics through the Butler–Volmer relationship while assuming uniform concentration, is more appropriate than the primary model.

The tertiary model, which also accounts for mass transport limitations, was not employed because the large excess of electrolyte minimizes concentration gradients and avoids unnecessary computational complexity. The secondary model therefore provides a practical and physically meaningful balance between computational efficiency and modeling accuracy.

## 5.2 Simulation description and results

As established in Section 5.1, this study employs the secondary current distribution model to simulate interfacial current behavior, which accurately captures the effects of finite charge-transfer kinetics while assuming a uniform electrolyte composition.<sup>[210,211,214]</sup> This approach enables spatially resolved predictions of current density across the electrode surface during lithium dissolution and deposition, particularly under the realistic galvanostatic conditions applied in this work.

Three simulation geometries were defined in COMSOL Multiphysics, as illustrated in Figure 40. All models shared a base configuration consisting of a thin-layer cell with lateral dimensions of  $1.2\text{ cm} \times 1.2\text{ cm}$  taken from the experimental cell. The working electrode (WE, blue) was placed at the bottom of the cell, while the counter electrode (CE, grey) was located at the top.

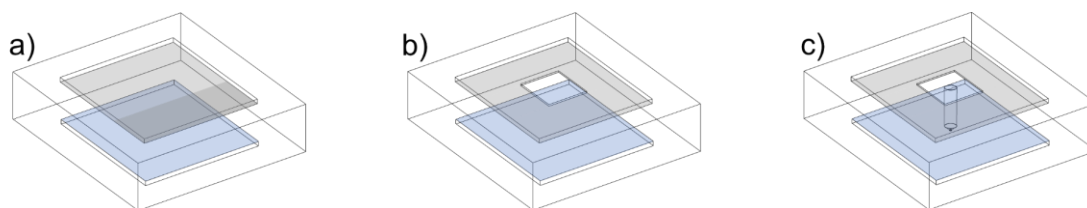


Figure 40. Schematic of the three simulation geometries with the lithium working electrode (WE) on the bottom (blue) and the lithium counter electrode (CE) at the top (grey): a) Symmetrical thin layer cell; b) CE with opening of  $4\text{ mm} \times 4\text{ mm}$ ; c) CE with opening and ME positioned over the center of the sample at a distance of  $12.5\text{ }\mu\text{m}$ .

Case a is a symmetric reference system, where the CE fully covers the WE without any opening and no ME is present. This configuration represents an idealized baseline with minimal distortion of the current field (Figure 40a).

Case b is identical to Case a, but included a  $4\text{ mm} \times 4\text{ mm}$  square opening in the CE to simulate the physical aperture used for inserting the ME. This isolates the effect of the mechanical access opening itself on the current density distribution (Figure 40b).

Case c incorporates both the CE opening and the presence of the ME, placed centrally above the WE at a vertical scanning distance of  $12.5\text{ }\mu\text{m}$ . It represents the realistic geometry encountered when the SECM probe remains in its imaging position during charge–discharge operation of the lithium electrodes (Figure 40c).

The detailed geometry of the ME is shown in Figure 41. It includes the ME radius, diameter of the outer ME body, and cone angle. This geometry was investigated to assess how the presence of the

SECM ME at its imaging position may perturb the current density distribution during galvanostatic cycling, thereby influencing the electrochemical environment at the lithium electrode.

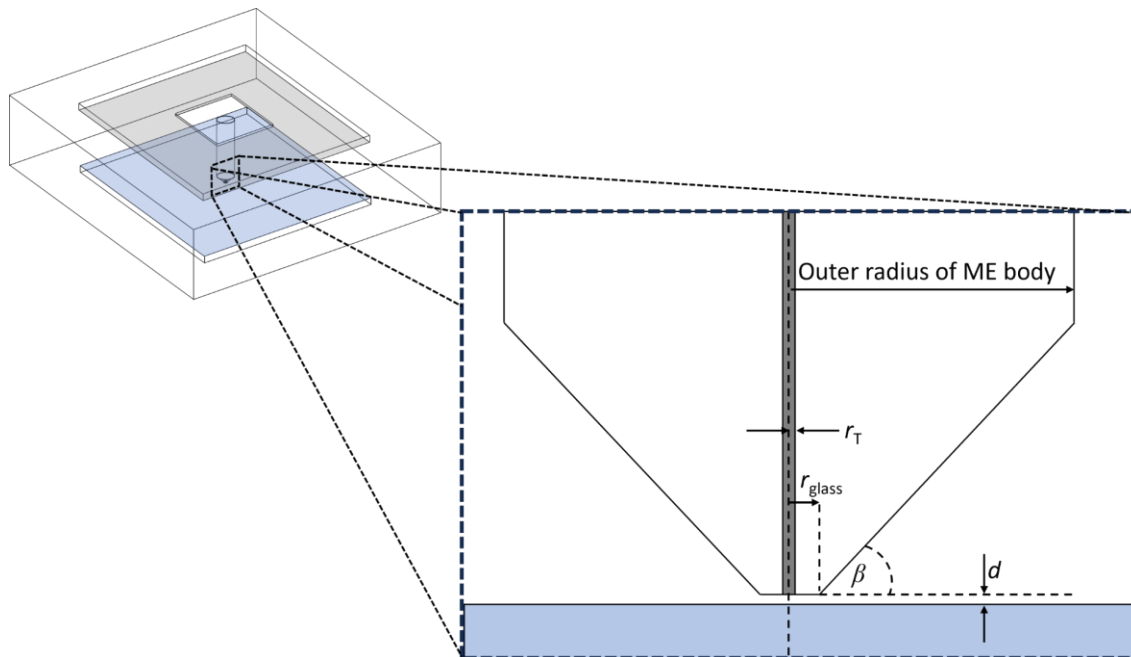


Figure 41. Geometry of the SECM microelectrode (ME) used in the simulation model. The diagram illustrates key parameters, including  $R_g = r_{\text{glass}}/r_T$ , distance  $d$  between working electrode (WE) and ME, outer radius of the ME body =  $1000 \mu\text{m}$ , and cone angle  $\beta$ .

### 5.2.1 Domain equations and boundary conditions

The current-voltage relationship is described by Eq. (113). The routine employed resolved the current and potential distributions on both the electrode and within the electrolyte. Mesh refinement was implemented along the electrode edges (electrode length/500) since these regions typically exhibit the highest errors when simulating electrochemical systems. All simulations were performed under steady-state conditions.

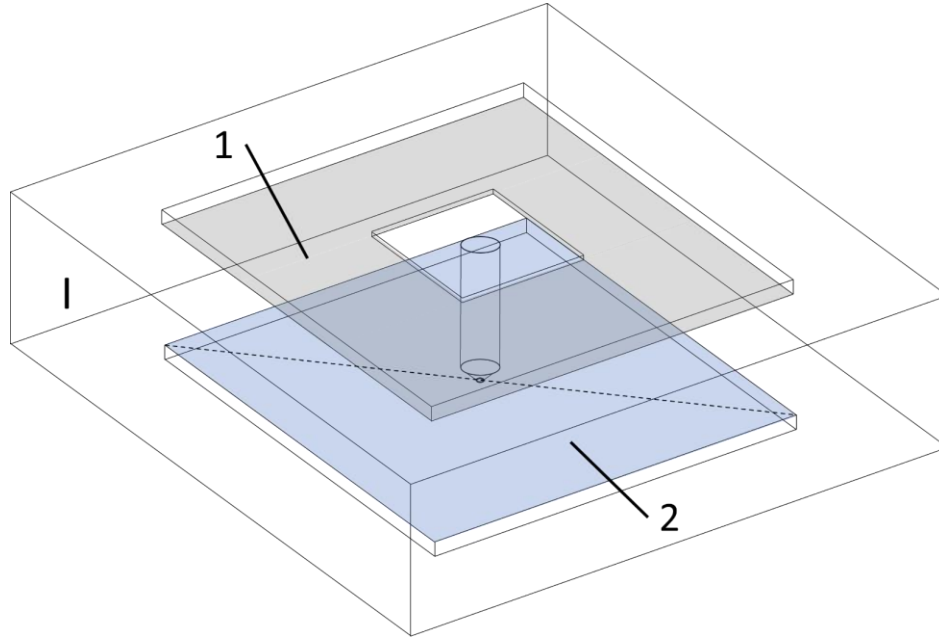


Figure 42. Schematic of the simulation geometry. The lithium WE (blue) below the ME with the lithium CE with the opening on top (grey). The secondary current density distribution was calculated along the dashed line across the working electrode.

### Electrolyte (Domain I)

Electrolyte conductivity  $\sigma_1$  [ $\text{S cm}^{-1}$ ] was considered constant according to Ohm's Law as sufficient supporting electrolyte was present in the solution. Three values were calculated:  $10 \text{ S m}^{-1}$ ,  $1 \text{ S m}^{-1}$ , and  $0.1 \text{ S m}^{-1}$ .

*Current-voltage relation in the electrolyte:*

$$i_1 = -\sigma_1 \nabla \phi_1 \quad (113)$$

with  $\phi_1$  being the electrical potential in the electrolyte.

*Current conservation in the electrolyte*

$$\nabla \cdot i_1 = 0 \quad (114)$$

### Counter electrode (Boundary 1)

The boundary condition for the CE was set to a fixed external potential of 0 V.

*External potential*

$$\phi_{\text{CE}} = 0 \text{ V} \quad (115)$$

## Working electrode (Boundary 2)

### *Local current density distribution*

The local current density was calculated using Butler-Volmer kinetics, with transfer number  $\alpha = 0.5$ , and an exchange current density  $j_0 = 10 \text{ A m}^{-2} = 1 \text{ mA cm}^{-2}$ . Examples of reported experimental values of limiting current densities of lithium ion in organic electrolytes<sup>[215]</sup> at 25 °C range between 0.95 mA/cm<sup>2</sup> (28 °C)<sup>[216]</sup> and 32 mA cm<sup>-2</sup> (25 °C).<sup>[217]</sup> Thus the simulation uses values for  $j_0$  in the range of experimental data.

$$j_{\text{loc}} = j_0 \left( \exp\left(\frac{\alpha F \eta}{RT}\right) - \exp\left(\frac{-\alpha F \eta}{RT}\right) \right) \quad (116)$$

### *Total current*

The boundary condition at the WE was set equal to the highest experimentally used total current  $i_{\text{total}} = 4 \text{ mA}$  for a geometric electrode area of  $1.44 \text{ cm}^2$  ( $j = 2.8 \text{ mA cm}^{-2}$ ). The total current is obtained by integrating the local current density across the whole electrode surface  $S$ .

$$\int_{\partial\Omega} j_{\text{loc}} \cdot \vec{n} dS = i_{\text{total}} = 4 \text{ mA} \quad (117)$$

Where  $\vec{n}$  is the normal vector at every point of the electrode surface and  $\partial\Omega$  is the boundary enclosing the electrode surface.

$$\eta = \phi_{\text{WE}} - E_{\text{ref}} \quad (118)$$

The potential distribution across the working electrode was solved in Eq. (118) to satisfy the total current imposed as a boundary condition. With  $E_{\text{ref}} = 0 \text{ V}$  as the reference potential,  $\phi_{\text{WE}}$  the working electrode potential and  $\eta$  the working electrode overpotential.

As previously mentioned, the presence of an excess amount of electrolyte facilitated the treatment of electrolyte conductivity ( $\sigma_1$ ) as a constant value. The value of  $1 \text{ S m}^{-1}$  closely aligns with the experimental value of  $1.1 \text{ S m}^{-1}$  for the  $1 \text{ M LiClO}_4$  in propylene carbonate utilized in the experimental setup.<sup>[218]</sup> Additional calculations were performed for the electrolyte conductivity, by varying the values by one order of magnitude above and below the reference value of  $1 \text{ S m}^{-1}$ . These calculations aimed to investigate the impact of different conductivity levels on the current density distribution within the system under study. The current density distribution plots are in Figure 43. The plots for a conductivity of  $1 \text{ S m}^{-1}$  (close the experimental value) are highlighted in blue in Figure 43a-c.

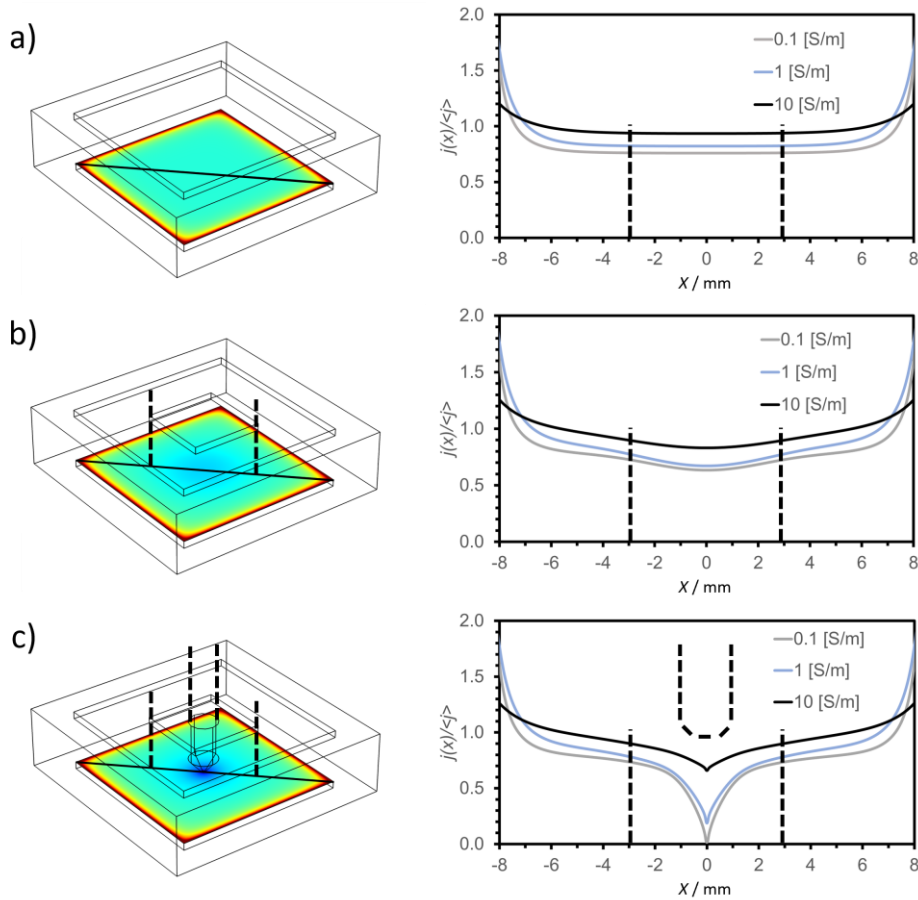


Figure 43. Simulated secondary current density distribution in the SECM cell for an average current density of  $2.8 \text{ mA cm}^{-2}$  at the bottom electrode. a) Symmetrical thin layer cell; b) CE with opening; c) CE with opening and ME positioned over the sample at  $12.5 \text{ }\mu\text{m}$ . ME dimensions were  $r_T = 12.5 \text{ }\mu\text{m}$ ,  $R_g = 4$ , cone angle  $\beta = 46.5^\circ$ , outer radius of ME body  $1000 \text{ }\mu\text{m}$ . Figure taken from own publication and slightly modified.<sup>[191]</sup>

In order to evaluate the effect of the opening in the CE on the current density of the bottom electrode, the local current density was divided by the average current density across the entire WE and compared to a setup with identical CE and WE geometries. The values along the diagonal of the bottom electrode were plotted in Figure 43 and the graph for the electrolyte conductivity used in the experiments is again emphasized in blue. The results show that, in all cases, the difference in the calculated current density between the case where the CE and WE are identical (Figure 43a) and the case where the CE has an opening (Figure 43b) present slight differences that do not significantly impact the observed results. However, when charging-discharging cycles are conducted while the microelectrode is positioned at the imaging location (Figure 43c), the local current density at the bottom electrode drops dramatically below the microelectrode. This indicates that the geometry of

the top electrode can significantly affect the current density of the sample electrode when the microelectrode is present at the imaging position. These variations are presented in Table 17.

Table 17. Comparison of normalized current densities calculated at the center of the WE ( $x = 0$ ), across the three simulated cases: Symmetrical thin layer cell (Flat), CE with opening (Gate), CE with opening and ME (Gate + ME)

<b>Conductivity</b>	<b>Flat</b>	<b>Gate</b>	<b>Gate and ME</b>	<b>Flat</b>	<b>Gate</b>	<b>Gate + ME</b>
[S m <sup>-1</sup> ]	$j(X)/\langle j \rangle$	$j(X)/\langle j \rangle$	$j(0)/\langle j \rangle$	[%]	[%]	[%]
0.1	0.76	0.63	0.01	100	83	2
1	0.82	0.67	0.19	100	82	23
10	0.93	0.83	0.66	100	89	70

For the calculations for  $\sigma_1$  values of 10 S m<sup>-1</sup>, it was possible to observe the effects of increased electrical conductivity on the current distribution. The results in Table 19 show the effect of a more efficient transport of charges within the system, leading to enhanced current densities in regions directly below the ME compared to the reference value as the drop is about 30 % compared to the flat electrodes and slightly less than 20 % compared to the cell with an opening in the top electrode.

Conversely, calculations for  $\sigma_1$  values of 0.1 S m<sup>-1</sup> provide insight into the effects of reduced electrolyte conductivity on the current density distribution. The lower conductivity limits ionic transport within the electrolyte, resulting in significantly lower current densities, down to 2 % of the reference case in the region beneath the ME.

For the case with a conductivity value of 1 S m<sup>-1</sup>, which closely matches the experimental value, there is an 18% decrease in current density between the symmetrical thin layer cell and the case with the opening present on the top electrode. This indicates that the recorded current density at the center position (without ME) is comparable to that of the thin layer case. However, current density suffers a significant reduction of 77% compared to the thin layer case when the ME was present at its working distance. This is regarded as a significant impact on the current density beneath the ME.

The effect of the radius of the electrode body along with the corresponding variation of the angle of the ME on the distribution of current density was also examined. This was conducted due to the frequent occurrence of these geometric variations in the experimental setting. Figure 44 show variations of the cone angle with  $R_g = 4$  and Figure 45 with  $R_g = 10$ . Three different outer radii of the

microelectrode were considered, 250  $\mu\text{m}$ , 500  $\mu\text{m}$  and 1000  $\mu\text{m}$ . As before, the blue lines represent the conductivity value employed in the experimental setup, while the black and grey lines depict conductivity values ten times higher and ten times lower.

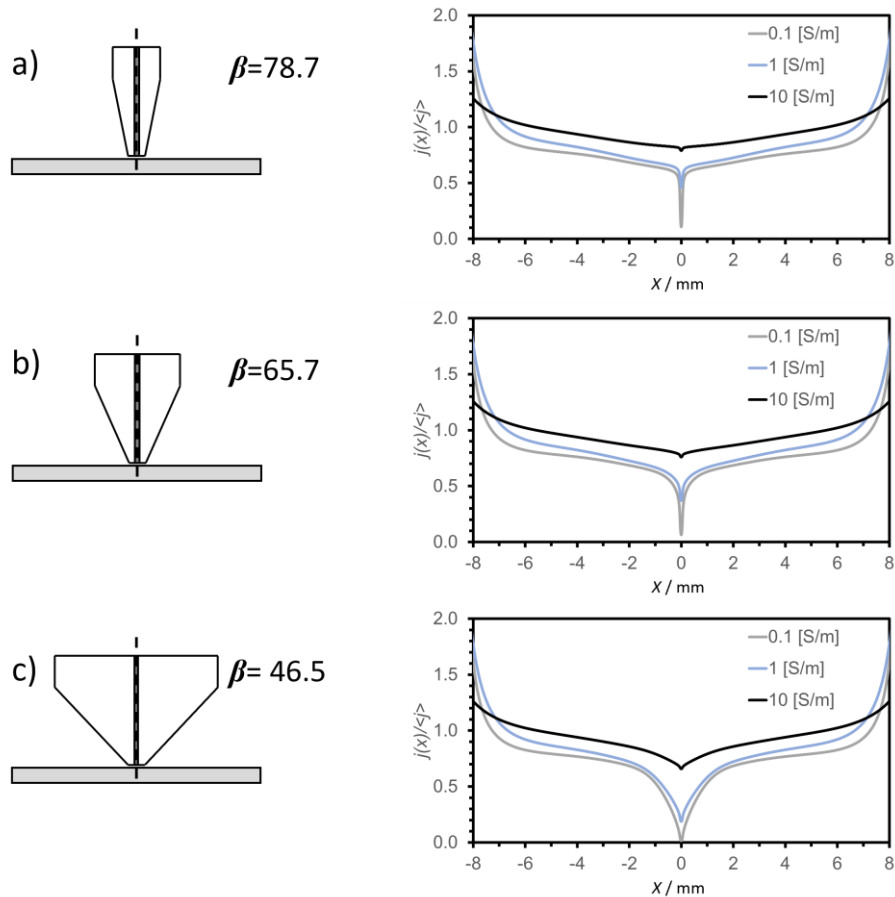


Figure 44. Simulated secondary current density distribution in the SECM cell during charging-discharging procedures with the ME at the working distance  $d = 12.5 \mu\text{m}$ . a)  $\beta = 78.7^\circ$ ,  $r_{\text{out}} = 250 \mu\text{m}$ , b)  $\beta = 65.7^\circ$ ,  $r_{\text{out}} = 500 \mu\text{m}$ ; c)  $\beta = 46.5^\circ$ ,  $r_{\text{out}} = 1000 \mu\text{m}$ ; other parameters  $r_{\text{T}} = 12.5 \mu\text{m}$ ,  $R_{\text{g}} = 4$ ,  $\langle j \rangle = 2.8 \text{ mA/cm}^2$ , electrolyte conductivities are given in the figure legend. Figure taken from own publication and slightly modified.<sup>[191]</sup>

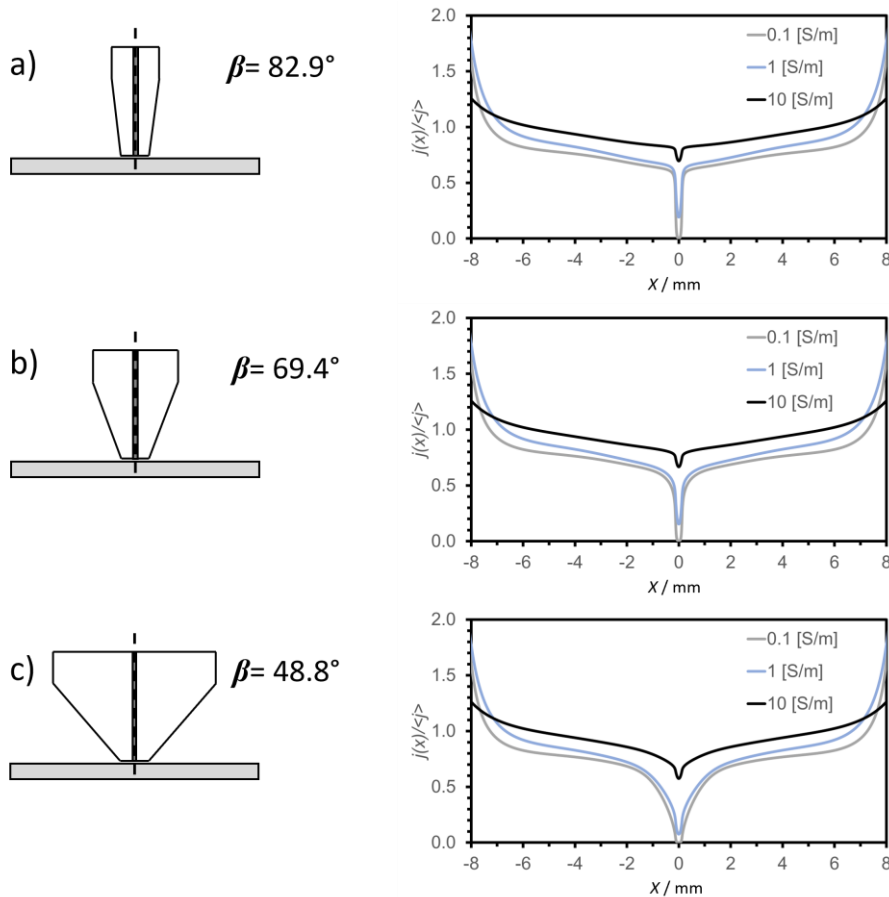


Figure 45. Simulated secondary current density distribution in the SECM cell during charging-discharging procedures with the ME at the working distance  $d = 12.5 \mu\text{m}$ . a)  $\beta = 82.9^\circ$ ,  $r_{\text{out}} = 250 \mu\text{m}$ , b)  $\beta = 69.4^\circ$ ,  $r_{\text{out}} = 500 \mu\text{m}$ ; c)  $\beta = 48.8^\circ$ ,  $r_{\text{out}} = 1000 \mu\text{m}$ ; other parameters  $r_T = 12.5 \mu\text{m}$ ,  $R_g = 10$ ,  $\langle j \rangle = 2.8 \text{ mA/cm}^2$ , electrolyte conductivities are given in the figure legend. Figure taken from own publication and slightly modified.<sup>[191]</sup>

The current density distribution was significantly influenced by the outer radius of the ME body. However, even when using the thinnest electrode, a substantial deviation in the local current density at the lithium electrode remained unavoidable directly below the ME. This effect was attributed to the inherent limitations of MEs and the complex nature of electrochemical systems. To mitigate this effect, the size of the insulating ME shaft could be reduced as much as possible, resulting in a more uniform current density distribution. However, this results in a very steep gradient of the local current density near the ME position for the cases where  $\sigma_1 = 1 \text{ S m}^{-1}$  or  $0.1 \text{ S m}^{-1}$ . This poses challenges in obtaining representative SECM images. Consequently, during the charging-discharging protocols, the ME must be retracted to address this issue and ensure reliable data acquisition.

The dimensionless current densities calculated at the center of the WE under the ME for all cases are presented in Table 18.

Table 18. Calculated normalized dimensionless current densities at  $x = 0$  at the sample electrode (bottom) for  $R_g = 4$ ,  $R_g = 10$ ;  $\sigma_1 = 0.1 \text{ S m}^{-1}$ ,  $1 \text{ S m}^{-1}$ ,  $10 \text{ S m}^{-1}$ ; outer radius = 1 mm, 0.50 mm, 0.25 mm.

$\sigma_1 [\text{S m}^{-1}]$	outer radius	$j(0)/\langle j \rangle, R_g = 4$	$j(0)/\langle j \rangle, R_g = 10$
0.1	1.00 mm	0.01	$4.5 \times 10^{-04}$
0.1	0.50 mm	0.07	$2.1 \times 10^{-03}$
0.1	0.25 mm	0.11	$3.4 \times 10^{-03}$

$\sigma_1 [\text{S m}^{-1}]$	outer radius	$j(0)/\langle j \rangle, R_g = 4$	$j(0)/\langle j \rangle, R_g = 10$
1	1.00 mm	0.19	0.08
1	0.50 mm	0.37	0.15
1	0.25 mm	0.46	0.19

$\sigma_1 [\text{S m}^{-1}]$	outer radius	$j(0)/\langle j \rangle, R_g = 4$	$j(0)/\langle j \rangle, R_g = 10$
10	1.00 mm	0.66	0.57
10	0.50 mm	0.76	0.67
10	0.25 mm	0.79	0.70

In a study conducted by Zampardi et al.,<sup>[219]</sup> graphite composite electrodes were cycled while keeping the ME in close proximity to the sample, with the aim to observe the influence of SEI formation on the feedback current of SECM. However, according to our simulation, this approach does not prevent the significant deviation of the local current density at the sample directly beneath the SECM microelectrode as demonstrated in this chapter.

The spatial resolution required to detect local defects associated with lithium dissolution and deposition is lacking in integral techniques such as electrochemical impedance spectroscopy (EIS). This limitation highlights the value of the methodology presented in this study, which enables the effective investigation and characterization of such localized features. The results emphasize the importance of retracting the microelectrode prior to SECM imaging in order to obtain accurate and representative current density distributions. These findings underscore the need for careful experimental design and operation when combining SECM with charge and discharge protocols for lithium electrodes. The same considerations apply to other electrode materials, provided that comparable average current densities and electrolyte conductivities are used.

The thoughts and simulations presented here can also be transferred to other scanning probe techniques aiming for imaging under operando conditions, such as electrochemical scanning force microscopy.

## 6. Summary and Outlook

This work used finite element method (FEM) simulations to explore transport properties and electrochemical behavior in experiments with scanning electrochemical microscopy (SECM) in nanoporous gold, supported platinum nanoparticles, and lithium electrodes. The focus was to develop modeling approaches that capture the complex spatial dynamics in electrochemical systems, aiming to support the quantitative interpretation of SECM measurements and bridge the gap between experimental observation and theoretical prediction.

The thesis explores electrochemical processes in nanoporous gold and supported platinum nanoparticles on carbon, using heterogeneous models of nanomaterials held in a cavity microelectrode (CME). These studies revealed how structural factors such as pore size and pore distribution impact the current response in SECM experiments and highlighted the limitations of existing analytical models, prompting the development of a simplified geometric simulation model that more accurately captures mass transport dynamics in porous media. A key outcome was the identification of vertical feedback, where electronic conductivity within the porous network enables rapid, indirect titration of adsorbed oxides throughout the electrode and stabilizes the SECM response. This phenomenon, reproduced by the simulations, explains why titration behavior becomes largely independent of cavity depth and establishes conductive connectivity as a decisive factor in porous electrode dynamics. For Pt/C electrodes, the model further suggested the coexistence of oxide layers with different reactivities, even though their full complexity could not yet be resolved. These discrepancies likely originate from the geometric complexities of the electrodes and the intrinsic variability in material properties, underscoring the challenges of accurately simulating real porous electrodes.

Building on this foundation, the research transitioned to the development of homogeneous models for porous substrates. The exploration of morphology of porous electrodes was made possible by the use of irreversible mediators excluding any effect of reaction at the porous substrate on the SECM ME current. The aim was to simplify the description of transport behavior while maintaining accuracy across various porosities and configurations. A new analytical equation for SECM approach curves for porous substrates was developed, incorporating parameters such as corrected porosity and effective diffusion coefficients. It provided a reliable representation of how porosity variations affect system behavior, covering a broad parameter space including film thickness and electrode geometry. However, it still requires refinement due to its dependence on multiple numerical parameters and its limited coverage of the full porosity range.

The FEM simulations were also used to evaluate secondary current density distributions in SECM experiments of lithium electrodes. In order to study the formation and evolution of the solid electrolyte interphase, Li metal electrodes are charged/discharged directly in a SECM cell. The SEI is crucial for battery performance and safety but difficult to characterize due to its dynamic and heterogeneous nature. The simulations demonstrated that the SECM probe can perturb local current distributions, underscoring the need for careful positioning and retraction during galvanostatic cycling in operando experiments. Such probe-induced effects must be accounted for when using SECM to characterize reactive electrode surfaces and when comparing results to real battery cells, where the microelectrode does not alter the local current density. The study was conducted for Li metal for methodological reasons. The obtained insights regarding all setup and appropriate experimental sequences can be directly transferred to analogous experiments with Li intercalation electrodes (graphite, Si, Sn). The developed models and simulations thus offer valuable tools for enhancing the interpretation of SECM imaging.

A key insight from this study is the importance of understanding the SECM measurement itself before drawing conclusions about battery behavior. The simulations illustrate how the presence and positioning of the SECM probe can influence local current distributions, particularly under galvanostatic conditions. Recognizing and quantifying these effects is essential for placing SECM observations into the correct electrochemical context. This understanding is a necessary step before such observations can meaningfully inform the interpretation of interfacial processes or guide the development of device materials and configurations.

Overall, this work highlights the value of combining SECM with FEM simulations to enhance the characterization of transport properties in complex electrochemical systems. The integrated approach supports the rational planning and analysis of SECM experiments and can aid in the design of materials and electrodes optimized for local electrochemical activity. While the developed models provide valuable insights, they also involve assumptions and simplifications that may limit their applicability under certain experimental conditions. Future work should aim to further refine these models, reduce their numerical complexity, and expand their relevance to a broader range of systems. Additionally, the development of alternative modeling strategies could address the limitations of current methods and support more robust interpretation of spatially resolved electrochemical data.

## 7. Appendix

### 7.1 Parameters, variables, and equations used in Chapter 3

Parameters employed in one of the simulations of Chapter 3 are shown in Table 19. The formatting of variables and expressions reflects their exact appearance as entered in the COMSOL Multiphysics interface. To maintain consistency with the input structure used in the software, typographic conventions such as italicizing variables have not been applied.

Table 19. Simulation parameters as defined in COMSOL Multiphysics.

Name	Expression	Value	Description
D	5[ $\mu\text{m}$ ]	5E-6 m	Tip-sub dist
d_L	d/rt	0.2	
Rt	25[ $\mu\text{m}$ ]	2.5E-5 m	Tip radius
St	25[ $\mu\text{m}$ ]	2.5E-5 m	CME radius
RG	3.5	3.5	Tip RG
RG2	3.5	3.5	CME RG
BH	500	500	Box size
Stz	16[ $\mu\text{m}$ ]	1.6E-5 m	CME depth
Pw	50[nm]	5E-8 m	Pore diameter
Asub	1.9635e-09[m <sup>2</sup> ]	1.9635E-9 m <sup>2</sup>	Sub area
E01	0.0[V]	0 V	Std pot
k01	0.1[m*s <sup>-1</sup> ]	0.1 m/s	Tip het const
Do1	5.5e-10[ m <sup>2</sup> /s]	5.5E-10 m <sup>2</sup> /s	Diff. coeff. ox
Dr1	5.5e-10[ m <sup>2</sup> /s]	5.5E-10 m <sup>2</sup> /s	Diff. coeff. red
co1	10[mmol/L]	10 mol/m <sup>3</sup>	Bulk conc.
I_ss	4*F_const*co1*Do1*rt	5.3067E-8 A	St. state curr. inf. dist.
T	298[K]	298 K	
R	R_const	8.3145 J/(mol·K)	
k_ox2	0.01[(m/s)]	0.01 m/s	Rate mediator Ox2
k_ox1	0.001[(m/s)]	0.001 m/s	Rate mediator Ox1
q10	1.6*q1ML	1.9564E-6 C	Input charge Ox1

## Appendix

Name	Expression	Value	Description
q20	$1.6 \cdot q_{1ML}$	$1.9564E-6 \text{ C}$	Input charge Ox2
i10	$q_{10}/(A_{sub} \cdot F)$	$1.4876E-4 \text{ mol/m}^2$	Surf. conc. of Ox1
i20	$q_{20}/(A_{sub} \cdot F)$	$6.4673E-5 \text{ mol/m}^2$	Surf. conc. of Ox2
F	F_const	$96485 \text{ C/mol}$	Faraday constant
F	$F/(R \cdot T)$	$38.941 \text{ 1/V}$	F/RT
N	1	1	Num. elec. tip reac.
A	0.50	0.5	symmetry factor
cs0	$2e-5[\text{mol/m}^2]$	$2E-5 \text{ mol/m}^2$	
ksi0	$100[1/s]$	$100 \text{ 1/s}$	
Cell_lim	BH*rt	$0.0125 \text{ m}$	
i1ML	$q_{10}/(A_{sub})/ML$	1.6	
i2ML	$q_{20}/(A_{sub})/ML$	1.6	
ML_mol	$ML/F\_const$	$4.0421E-5 \text{ mol/m}^2$	
ML	$390[\mu\text{C/cm}^2]$	$3.9 \text{ C/m}^2$	1 ML charge conc.
q1ML	$ML \cdot A_{sub}$	$1.2228E-6 \text{ C}$	Charge of 1 ML
A_sub	$0.31353[\text{mm}^2]$	$3.1353E-7 \text{ m}^2$	CME area
Theta_max	ML_mol	$4.0421E-5 \text{ mol/m}^2$	Max ox. coverage
Sigma_cs1	1	1	Occupancy Ox1
Sigma_cs2	1	1	Occupancy Ox2
pore_num	$st/(2 \cdot pw)$	250	Num. of pores
Dcs1	$100 \cdot Dr1$	$5.5E-8 \text{ m}^2/\text{s}$	Ox. diff. coeff
A_sub_8	$3.1549E-7[\text{m}^2]$	$3.1549E-7 \text{ m}^2$	CME $8\mu\text{m}$ area
A_sub_12	$4.7226E-7[\text{m}^2]$	$4.7226E-7 \text{ m}^2$	CME $12\mu\text{m}$ area
A_sub_16	$6.2903E-7[\text{m}^2]$	$6.2903E-7 \text{ m}^2$	CME $16\mu\text{m}$ area

Table 20: Variables defined at the ME boundary in COMSOL.

Name	Expression	Unit	Description
kf1	$k_{01} \cdot \exp(-a \cdot f \cdot (E - E_{01}))$	m/s	Fwd. const.
kb1	$k_{01} \cdot \exp((1 - a) \cdot f \cdot (E - E_{01}))$	m/s	Back const.
E	$-0.5[\text{V}]$	V	Tip pot.

## Appendix

Name	Expression	Unit	Description
current	$2*\pi*F\_const*\intop1(tds.ndflux\_o1*r)$	A	Tip current

Table 21. Variables defined at the substrate (CME) employed in one of the simulations of Chapter 3

Name	Expression	Unit	Description
theta1	$\max(\text{eps}, \min(\text{Sigma\_cs1}*cs1/\text{Theta\_max}, 1))$	1	Ox1 frac. coverage
theta2	$\max(\text{eps}, \min(\text{Sigma\_cs2}*cs2/\text{Theta\_max}, 1))$	1	Ox2 frac. coverage

Table 22. Inward flux equations defined at the tip ME

Description	Value
Flux type	General inward flux
Species o1	$(-kf1*o1 + kb1*r1)$
Species r1	$-(-kf1*o1 + kb1*r1)$

Table 23. Inward flux equations defined at the substrate CME

Description	Value
Flux type	General inward flux
Species o1	$(\text{theta1} - \text{theta2})*k\_ox1*r1 + (\text{theta2})*k\_ox2*r1$
Species r1	$-((\text{theta1} - \text{theta2})*k\_ox1*r1 + (\text{theta2})*k\_ox2*r1)$

Table 24. Inward flux equations defined at the substrate CME

Description	Value
Reaction rate for surface species cs1	$(-(\text{theta1} - \text{theta2})*k\_ox1*r1)$
Reaction rate for surface species cs2	$(-(\text{theta2})*k\_ox2*r1)$

## 7.2 Parameters, variables, and equations used in Chapter 4

Parameters employed in one of the simulations of Chapter 4 are shown in Table 19. The formatting of variables and expressions reflects their exact appearance as entered in the COMSOL Multiphysics interface. To maintain consistency with the input structure used in the software, typographic conventions such as italicizing variables have not been applied.

Table 25. Simulation parameters as defined in COMSOL Multiphysics.

Name	Expression	Value	Description
A	0.50	0.5	symmetry factor
Alpha	$\log(2) + \log(2)*(1 - (2/\pi)*\text{acos}(1/RG))$ $\log(2)*(1 - ((2/\pi)*\text{acos}(1/RG))^2)$	0.61828 rad	
Beta	$1 + 0.639*(1 - (2/\pi)*\text{acos}(1/RG))$ $0.186*(1 - ((2/\pi)*\text{acos}(1/RG))^2)$	1.0357 rad	
BH	1000	1000	Box size
c_bulk	1[mmol/L]	1 mol/m <sup>3</sup>	Concentration of ox species, bulk mM
Cell_lim	BH*rt	0.025 m	Cell boundaries
D	1000[μm]	0.001 m	Tip-Sub distance
D_eff	por/tau_br	0.71554	Effective Diff.
d_film	800[μm]	8E-4 m	Porous substrate thickness
d_film2	50[nm]	5E-8 m	Skin layer
d_L	d/rt	40	
Do1	5.8e-10[ m <sup>2</sup> /s]	5.8E-10 m <sup>2</sup> /s	Diffusion coefficients in bulk m <sup>2</sup> /s

Name	Expression	Value	Description
E	-0.5[V]	-0.5 V	
epsilon	0.5	0.5	
F	$F/(R\_const*T)$	38.941 1/V	F/RT
F	F_const	96485 C/mol	Faraday constant
glass_incline	84	84	
glass_wall	1650[μm]	0.00165 m	
I_nf	$\frac{((2.08/(RG^{0.358}))*(d\_L - 0.145/RG) + 1.585)/((2.08/RG^{0.358})*(d\_L + 0.0023*RG) + 1.57 + \log(RG)/d\_L + ((2/(pi*RG))*\log(1 + (pi*RG)/2*d\_L))) \alpha + pi/(4*beta*atan(d\_L))}{(1 - \alpha) + 1/(2*beta)*(2/pi)*atan(d\_L)}$	0.98387	
I_pf		1.1166 rad	
I_ss	$4*beta*F\_const*Do1*c\_bulk*rt$	5.796E-9 A	
k0	0.1[m/s]	0.1 m/s	Tip Standard
k01	0.1[m*s^- 1]	0.1 m/s	Electrochemical reaction constant for tip
k02	0.1[m*s^- 1]	0.1 m/s	Substrate Standard EC constant
Kappa	$(k02*rt)/Do1$	4310.3	
Lefrou	$I\_ss*I\_nf$	5.7025E-9 A	
N	1	1	number of electrons, tip reaction
Por	0.8	0.8	
por_2	0.5	0.5	

Name	Expression	Value	Description
RG	5.2	5.2	
RG2	3.5	3.5	
Rt	25[ $\mu\text{m}$ ]	2.5E-5 m	
St	1000[ $\mu\text{m}$ ]	0.001 m	
Stz	150[ $\mu\text{m}$ ]	1.5E-4 m	
T	298[K]	298 K	
tau_br	por <sup>(-1/2)</sup>	1.118	
tau_mq	por <sup>(-1/3)</sup>	1.0772	
Tilt	0[ $^\circ$ ]	0 rad	
Tor	por_2 <sup>-0.5</sup>	1.4142	
V	2*pi*stz*st <sup>2</sup>	9.4248E-10 m <sup>3</sup>	

Table 26. Variables defined at the ME boundary in COMSOL.

Name	Expression	Unit	Description
Beta	$1 + 0.639*(1 - (2/\pi)*\text{acos}(1/\text{RG})) - 0.186*(1 - ((2/\pi)*\text{acos}(1/\text{RG}))^2)$	rad	
Iss	$4*\text{Beta}*F_{\text{const}}*\text{Do1}*c_{\text{bulk}}*r_t$	A	
NiT	current/Iss		
Current	$F_{\text{const}}*\text{intop1}(\text{tds.bndFlux}_c)$	A	

### 7.3 MATLAB script used in Chapter 4

```

% This routine performs the Fit calibration (12 parameters).
% INPUT
% matFile    : MAT-file containing the data from the COMSOL simulations:
%              - Sim_data (Nx5) -> [ d NiT RG porosity d_film ]
% d = ME-substrate distance
% NiT = dimensionless ME current
% RG = glass sheath/ ME factor
% d_film = porous substrate thickness
%
% OUTPUT
% Pfit       : 1x12 vector of fitted model parameters
% resnorm    : Sum of squares of residuals returned by LSQCURVEFIT
% exitflag   : Optimizer exit condition flag
% output     : Structure with optimization diagnostics
%
% NOTES

```

---

```

% - Requires MATLAB Optimization Toolbox.
%
% MODEL
% The response NiT is modeled as a weighted combination of two terms:
% porosity * f(d,RG,por,d_film; P1..P6) + (1-porosity) * g(d,RG,por; P7..P12)
% where the algebra matches the original (Kuss-Mauzerol-type form).

%loads simulation data
load Sim_data.mat

% ME radius in μm
rt = 25;

%Renaming of the loaded variables
Res_sim = [Res(:,1)/rt Res(:,2) Res(:,3) Res(:,4) Res(:,5)/rt];

%[d RG por d_film], fit whole data set
x = [Res_sim(:,1) Res_sim(:,3) Res_sim(:,4) Res_sim(:,5)];

NiT_sim = Res_sim(:,2); %fit whole data set

% initial estimates of fitting parameters
P_0 = [1 1 1 1 1 1 1 1 1 1];

% Recalculation of parameters
N_it_fit = @(P,x) (x(:,3)).*(P(1)./x(:,2).^P(2).*((x(:,4)+x(:,1))- ...
P(3)./x(:,2))+P(4)).*((P(1)./x(:,2).^P(2).*((x(:,4)+x(:,1)))+P(5)+ ...
log(x(:,2))./(x(:,4)+x(:,1))+2./pi./x(:,2).*log(1+pi.*x(:,2)./2./(x(:,4)+ ...
x(:,1))))).^(-1) ...
+ (1-x(:,3)).*(P(6)./x(:,2).^P(7).*((x(:,1))- ...
P(8)./x(:,2))+P(9)).*(P(6)./x(:,2).^P(7).*((x(:,1)))+P(10)+ ...
log(x(:,2))./(x(:,1))+2./pi./x(:,2).*log(1+pi.*x(:,2)./2./(x(:,1))))).^(-1;

% optimization options
opts = optimoptions(@lsqcurvefit,'Algorithm','trust-region-...
reflective','FunctionTolerance',1e-26,'optimalitytolerance',1e-16...
,'StepTolerance',1e-28,'StepTolerance',1e-24, ...
'MaxFunctionEvaluations',200000,'MaxIterations',8000);

% Result
[Pfit,resnorm,~,exitflag,output] = lsqcurvefit(N_it_fit,P_0,x,NiT_sim);

```

## 7.4 Parameters, variables, and equations used in Chapter 5

Parameters employed in one of the simulations of Chapter 5 are shown in Table 27. The formatting of variables and expressions reflects their exact appearance as entered in the COMSOL Multiphysics interface. To maintain consistency with the input structure used in the software, typographic conventions such as italicizing variables have not been applied.

Table 27. Variables defined at the substrate (CME) employed in one of the simulations of Chapter 5

Name	Expression	Value	Description
box_size	16[mm]	0.016 m	Cell width
d1	12[mm]	0.012 m	Elect. depth
w1	12[mm]	0.012 m	Elect. width
h1	0.5[mm]	5E-4 m	Elect. thickness
z2	3.3[mm]	0.0033 m	WE / CE distance
d2	5[mm]	0.005 m	Gate depth
h2	h1	5E-4 m	Gate thickness
w2	5[mm]	0.005 m	Gate width
LiClO4	1[M]	1000 mol/m <sup>3</sup>	Electrolyte conc.
E1	0[V]	0 V	
i0	1e2[A/m <sup>2</sup> ]	100 A/m <sup>2</sup>	Ex. current dens.
sigma	10[S/m]	10 S/m	Conductivity
D	1e-10[m <sup>2</sup> /s]	1E-10 m <sup>2</sup> /s	Diffusion coeff.
E2	0.0[V]	0 V	""
E_ini_Liion	E_eq_Liion + R_const*T/(2*F_const)*log( c_Liion_bulk/c_Liion_bulk)	-3.04 V	"Initial electrolyte potential"
T	298[K]	298 K	Temperature
c_Liion_bulk	1[M]	1000 mol/m <sup>3</sup>	Electrolyte concentration
i_app	4[mA]	0.004 A	Applied current
E_eq_Liion	-3.04[V]	-3.04 V	Standard eq. potential
c0	1000[mol/m <sup>3</sup> ]	1000 mol/m <sup>3</sup>	Initial concentration

---

## 7.5 Abbreviations

CE	counter electrode
CME	cavity microelectrode
CV	cyclovoltammetry
EIS	electrochemical impedance spectroscopy
FB	Feedback
FEM	finite element method
IUPAC	The International Union of Pure and Applied Chemistry
ME	microelectrode
ML	monolayer
MSM	multi-scale methods
NPG	nanoporous gold
Pt/C	platinum supported on carbon
SECM	scanning electrochemical microscopy
SEI	solid electrolyte interphase
SEM	scanning electron microscopy
SHE	standard hydrogen electrode
SI-SECM	Surface interrogation mode SECM
WE	working electrode

## 7.6 Symbols

$J_i$	molar flux per unit area of species $i$
$D_i$	diffusion coefficient of species $i$
$c_i$	concentration of species $i$
$z_i$	charge number of species $i$
$F$	Faraday constant (96,485 C·mol <sup>-1</sup> )
$R$	universal gas constant (8.314 J·mol <sup>-1</sup> ·K <sup>-1</sup> )
$T$	absolute temperature in Kelvin
$\Phi$	electric potential
$V$	fluid velocity
$I$	current
$R$	net reaction rate
$N$	number of electrons
$A$	surface area of the electrode
O	oxidized form of a redox pair
R	reduced form of a redox pair
$E$	transferred electron
$r_f$	rate of the forward reaction (mol·s <sup>-1</sup> ·m <sup>-2</sup> )
$r_b$	rate of the backward reaction (mol·s <sup>-1</sup> ·m <sup>-2</sup> )
$E$	electrode potential (V)
$E^0$	standard potential (V)
$E^{0'}$	formal potential (V)
$E_{eq}$	equilibrium potential of a redox couple (V)
$k^0$	heterogeneous rate constant (m·s <sup>-1</sup> )
$c^*_O$	bulk concentration of the oxidized species
$c^*_R$	bulk concentration of the reduced species
$c_O$	concentration of the oxidized species
$c_R$	concentration of the reduced species
$i_c$	cathodic current (A)
$i_a$	anodic current (A)
$i_{T,\infty}$	steady-state tip current at infinite distance from the substrate
$R_g$	geometric factor, accounts for the tip shape

## Appendix

---

$r_T$	radius of the microelectrode tip
$I_T$	dimensionless current at the ME
$i_T$	current at the tip of the ME
$L$	distance between the ME and the substrate divided by the radius of the ME
$K$	dimensionless rate constant
$k_s$	heterogeneous rate constant
$P$	porosity
$V_V$	void volume
$V_T$	total volume
$D_{\text{eff}}$	effective diffusion coefficient
$T$	tortuosity factor
$\mathbf{D}$	diffusion coefficients diagonal matrix
$\mathbf{k}$	reaction matrix for first-order reactions
$\vec{c}$	concentration vector
$\Omega$	spatial domain
$\Omega_D$	dirichlet domain
$\Omega_N$	neumann boundary
$\mathbf{E}$	electrode matrix
$\Psi_{\text{rs}}$	dimensionless analytical negative feedback current
$\Psi_{\text{sim}}$	dimensionless current from simulations
$\Psi_{\text{fit}}$	dimensionless current from analytical equation
$L$	dimensionless ME-substrate distance
$L_{\text{film}}$	dimensionless substrate thickness
$\sigma_1$	electrolyte conductivity
$j$	current density
$\eta$	overpotential

## 8. References

- [1] A. Huang, Y. He, Y. Zhou, Y. Zhou, Y. Yang, J. Zhang, L. Luo, Q. Mao, D. Hou, J. Yang, *J. Mater. Sci.* **2019**, *54*, 949.
- [2] S. A. Kirillov, *Theor. Exp. Chem.* **2019**, *55*, 73.
- [3] G. Wittstock, M. Burchardt, S. E. Pust, Y. Shen, C. Zhao, *Angew. Chem., Int. Ed.* **2007**, *46*, 1584.
- [4] A. J. Bard, L. R. Faulkner, H. S. White in *Electrochemical methods. Fundamentals and applications*, Wiley, Hoboken NJ, **2022**, pp. 4–11.
- [5] R. C. Engstrom, M. Weber, D. J. Wunder, R. Burgess, S. Winquist, *Anal. Chem.* **1986**, *58*, 844.
- [6] A. J. Bard, F. R. F. Fan, J. Kwak, O. Lev, *Anal. Chem.* **1989**, *61*, 132.
- [7] A. L. Barker, J. V. Macpherson, C. J. Slevin, P. R. Unwin, *J. Phys. Chem. B* **1998**, *102*, 1586.
- [8] J. Izquierdo, S. Gonzalez, R. M. Souto, *Int. J. Electrochem. Sci.* **2012**, *7*, 11377.
- [9] Y. Selzer, I. Turyan, D. Mandler, *J. Phys. Chem. B* **1999**, *103*, 1509.
- [10] J. L. Fernández, M. Wijesinghe, C. G. Zoski, *Anal. Chem.* **2015**, *87*, 1066.
- [11] L. P. Bauermann, W. Schuhmann, A. Schulte, *Phys. Chem. Chem. Phys.* **2004**, *6*, 4003.
- [12] K. Nagamine, S. Onodera, A. Kurihara, T. Yasukawa, H. Shiku, R. Asano, I. Kumagai, T. Matsue, *Biotechnol. Bioeng.* **2007**, *96*, 1008.
- [13] E. M. Oliveira, S. Beyer, J. Heinze, *Bioelectrochemistry* **2007**, *71*, 186.
- [14] C. Kurzawa, M. Mosbach, E. Bensen, W. Schuhmann, *Proc. - Electrochem. Soc.* **2001**, *2001-18*, 304.
- [15] B. R. Horrocks, G. Wittstock in *Scanning electrochemical microscopy* (Eds.: A. J. Bard, M. V. Mirkin) 2<sup>nd</sup> ed., CRC Press, Boca Raton Fla., **2012**, pp. 317–378.
- [16] D. E. Tallman, M. B. Jensen in *Scanning electrochemical microscopy* (Eds.: A. J. Bard, M. V. Mirkin) 2<sup>nd</sup> ed., CRC Press, Boca Raton Fla., **2012**, pp. 451–488.
- [17] J. Mauzeroll, S. B. Schougaard in *Scanning electrochemical microscopy* (Eds.: A. J. Bard, M. V. Mirkin) 2<sup>nd</sup> ed., CRC Press, Boca Raton Fla., **2012**, pp. 379–416.
- [18] J. R. Lopéz, C. G. Zoski, A. J. Bard in *Scanning electrochemical microscopy* (Eds.: A. J. Bard, M. V. Mirkin) 2<sup>nd</sup> ed., CRC Press, Boca Raton Fla., **2012**, pp. 525–568.
- [19] J. Heinze, *Angew. Chem., Int. Ed.* **1993**, *32*, 1268.
- [20] A. M. Bond, M. Fleischmann, J. Robinson, *J. Electroanal. Chem.* **1984**, *168*, 299.

- [21] J. Ghoroghchian, F. Sarfarazi, T. Dibble, J. Cassidy, J. J. Smith, A. Russell, G. Dunmore, M. Fleischmann, S. Pons, *Anal. Chem.* **2002**, *58*, 2278.
- [22] Y. Saito, *Rev. Polarogr.* **1968**, *15*, 177.
- [23] J. Heinze, *Angew. Chem., Int. Ed.* **1991**, *30*, 170.
- [24] D. Mandler, A. J. Bard, *J. Electrochem. Soc.* **1989**, *136*, 3143.
- [25] A. J. Bard, M. V. Mirkin, P. R. Unwin, D. O. Wipf, *J. Phys. Chem.* **1992**, *96*, 1861.
- [26] H. Xiong, J. Guo, S. Amemiya, *Anal. Chem.* **2007**, *79*, 2735.
- [27] P. R. Unwin, A. J. Bard, *J. Phys. Chem.* **1991**, *95*, 7814.
- [28] F. Zhou, P. R. Unwin, A. J. Bard, *J. Phys. Chem.* **1992**, *96*, 4917.
- [29] C. Demaille, P. R. Unwin, A. J. Bard, *J. Phys. Chem.* **1996**, *100*, 14137.
- [30] C. M. Sanchez-Sanchez, J. Rodriguez-Lopez, A. J. Bard, *Anal. Chem.* **2008**, *80*, 3254.
- [31] J. Y. Kim, H. S. Ahn, A. J. Bard, *Anal. Chem.* **2018**, *90*, 3045.
- [32] Z. Liang, H. S. Ahn, A. J. Bard, *J. Am. Chem. Soc.* **2017**, *139*, 4854.
- [33] J. Rodríguez-López, A. J. Bard, *J. Am. Chem. Soc.* **2010**, *132*, 5121.
- [34] H. S. Ahn, A. J. Bard, *J. Am. Chem. Soc.* **2016**, *138*, 313.
- [35] J. Rodríguez-López in *Electroanalytical Chemistry: A Series of Advances* (Eds.: A. J. Bard, C. Zoski), CRC Press, **2012**, pp. 287–352.
- [36] C. M. Sanchez-Sanchez, A. J. Bard, *Anal. Chem.* **2009**, *81*, 8094.
- [37] Y.-F. Yang, G. Denuault, *J. Electroanal. Chem.* **1998**, *443*, 273.
- [38] Q. Wang, J. Rodríguez-López, A. J. Bard, *J. Am. Chem. Soc.* **2009**, *131*, 17046.
- [39] A. J. Bard, G. Denuault, R. A. Friesner, B. C. Dornblaser, L. S. Tuckerman, *Anal. Chem.* **1991**, *63*, 1282.
- [40] B. H. Simpson, J. Rodríguez-López, *Electrochim. Acta* **2015**, *179*, 74.
- [41] H. S. Ahn, A. J. Bard, *J. Phys. Chem. Lett.* **2016**, *7*, 2748.
- [42] C. G. Zoski, C. R. Luman, J. L. Fernández, A. J. Bard, *Anal. Chem.* **2007**, *79*, 4957.
- [43] K. C. Leonard, K. M. Nam, H. C. Lee, S. H. Kang, H. S. Park, A. J. Bard, *J. Phys. Chem. C* **2013**, *117*, 15901.
- [44] S. B. Basame, H. S. White, *J. Phys. Chem. B* **1998**, *102*, 9812.
- [45] J. Rodriguez-Lopez in *Electroanal. Chem.*, **2012**, pp. 287–341.
- [46] E. Abucayon, N. Ke, R. Cornut, A. Patelunas, D. Miller, M. K. Nishiguchi, C. G. Zoski, *Anal. Chem.* **2014**, *86*, 498.
- [47] E. Weinan, *Principles of multiscale modeling*, Cambridge University Press, Cambridge, New York, **2011**.

- [48] A. Doménech-Carbó, *Electrochemistry of porous materials*, CRC Press, Boca Raton FL, **2010**.
- [49] J. Newman, W. Tiedemann, *AIChE Journal* **1975**, *21*, 25.
- [50] A. Gully, H. Liu, S. Srinivasan, A. K. Sethurajan, S. Schougaard, B. Protas, *J. Electrochem. Soc.* **2014**, *161*, E3066-E3077.
- [51] J. L. Auriault, *Int. J. Eng. Sci.* **1991**, *29*, 785.
- [52] X. Zhang, D. M. Tartakovsky, *J. Electrochem. Soc.* **2017**, *164*, E53-E61.
- [53] E. E. Petersen, *AIChE J.* **1958**, *4*, 343.
- [54] M. B. Clennell, *Geol. Soc. Spec. Publ.* **1997**, *122*, 299.
- [55] N. Epstein, *Chem. Eng. Sci.* **1989**, *44*, 777.
- [56] P. C. Carman, *Chem. Eng. Res. Des.* **1997**, *75*, S32-S48.
- [57] J. Chaskalovic, *Finite element methods for engineering sciences. Theoretical approach and problem solving techniques*, Springer, Berlin, **2008**.
- [58] S. W. Feldberg, C. Auerbach, *Anal. Chem.* **1964**, *36*, 505.
- [59] M. Rudolph, *J. Electroanal. Chem. Interfacial Electrochem.* **1991**, *314*, 13.
- [60] M. Rudolph, *J. Electroanal. Chem.* **1992**, *338*, 85.
- [61] M. Penczek, Z. Stojek, J. Osteryoung, *J. Electroanal. Chem. Interfacial Electrochem.* **1984**, *170*, 99.
- [62] M. Penczek, Z. Stojek, *J. Electroanal. Chem. Interfacial Electrochem.* **1984**, *181*, 83.
- [63] T. Nann, J. Heinze, *Electrochem. Commun.* **1999**, *1*, 289.
- [64] R. Ferrigno, P.-F. Brevet, H. H. Girault, *J. Electroanal. Chem.* **1997**, *430*, 235.
- [65] R. L. Taylor, J. Z. Zhu, O. C. Zienkiewicz, *The Finite Element Method: Its Basis and Fundamentals*, Elsevier Butterworth-Heinemann, Amsterdam, **2005**.
- [66] Z. Ye, Z. Zhu, Q. Zhang, X. Liu, J. Zhang, F. Cao, *Corros. Sci.* **2018**, *143*, 221.
- [67] S. Kuss, C. Kuss, D. Trinh, S. B. Schougaard, J. Mauzeroll, *Electrochim. Acta* **2013**, *110*, 42.
- [68] R. Cornut, C. Lefrou, *J. Electroanal. Chem.* **2008**, *623*, 197.
- [69] R. Cornut, C. Lefrou, *J. Electroanal. Chem.* **2008**, *621*, 178.
- [70] E. J. Dickinson, H. Ekström, E. Fontes, *Electrochem. Commun.* **2014**, *40*, 71.
- [71] D. O. Kim, A. Mishra, M. Zorigt, Y. Li, R. T. Haasch, J. Rodríguez-López, *J. Mater. Chem. A* **2025**, *13*, 10540.
- [72] A. Minguzzi, M. A. Alpuche-Avilés, J. R. López, S. Rondinini, A. J. Bard, *Anal. Chem.* **2008**, *80*, 4055.

- [73] C.-L. Lin, J. Rodríguez-Lopez, A. J. Bard, *Anal. Chem.* **2009**, *81*, 8868.
- [74] M. Shen, J. Rodríguez-López, J. Huang, Q. Liu, X.-H. Zhu, A. J. Bard, *J. Am. Chem. Soc.* **2010**, *132*, 13453.
- [75] Z. J. Barton, J. Rodríguez-López, *Anal. Chem.* **2017**, *89*, 2708.
- [76] Z. T. Gossage, N. B. Schorr, K. Hernández-Burgos, J. Hui, B. H. Simpson, E. C. Montoto, J. Rodríguez-López, *Langmuir* **2017**, *33*, 9455.
- [77] Z. J. Barton, J. Rodríguez-López, *Anal. Chem.* **2014**, *86*, 10660.
- [78] F. Cao, J. Kim, A. J. Bard, *J. Am. Chem. Soc.* **2014**, *136*, 18163.
- [79] K. C. Leonard, A. J. Bard, *J. Am. Chem. Soc.* **2013**, *135*, 15890.
- [80] D. Britz, J. Strutwolf in *Lecture notes in physics, Vol. 666*, Springer, Berlin, New York, **2005**, pp. 6–7.
- [81] F. G. Cottrell, *Z. Phys. Chem. (Muenchen, Ger.)* **1903**, *42U*.
- [82] P. J. Mahon, K. B. Oldham, *Anal. Chem.* **2005**, *77*, 6100.
- [83] D. J. Gavaghan, *J. Electroanal. Chem.* **1997**, *420*, 147.
- [84] D. J. Gavaghan, *J. Electroanal. Chem.* **1998**, *456*, 1.
- [85] M. G. D. Geers, V. G. Kouznetsova, K. Matouš, J. Yvonnet in *Encyclopedia of computational mechanics* (Eds.: E. Stein, R. d. Borst, T. J. R. Hughes), John Wiley & Sons Ltd, Chichester, West Sussex, England, Hoboken, NJ, **2018**, pp. 1–34.
- [86] U. Hornung in *Interdisciplinary Applied Mathematics, Vol. 6*, Springer, New York, NY, **1997**, pp. 1–4.
- [87] W. E., B. Engquist, X. Li, W. Ren, E. Vanden-Eijnden, *Commun. Comput. Phys.* **2007**, *2*, 367.
- [88] T. D. Le, D. Lasseux, X. P. Nguyen, G. Vignoles, N. Mano, A. Kuhn, *Chem. Eng. Sci.* **2017**, *173*, 153.
- [89] T. Fatima, N. Arab, E. P. Zemskov, A. Muntean, *J. Eng. Math.* **2011**, *69*, 261.
- [90] G. A. Pavliotis, A. M. Stuart, *Multiscale Methods. Averaging and Homogenization*, Springer New York; Springer e-books, New York, NY, **2008**.
- [91] M. Geers, V. G. Kouznetsova, W. Brekelmans, *J. Comput. Appl. Math.* **2010**, *234*, 2175.
- [92] Y. Davit, C. G. Bell, H. M. Byrne, L. A. Chapman, L. S. Kimpton, G. E. Lang, K. H. Leonard, J. M. Oliver, N. C. Pearson, R. J. Shipley et al., *Adv. Water Resour.* **2013**, *62*, 178.
- [93] J. Biener, M. M. Biener, R. J. Madix, C. M. Friend, *ACS Catal.* **2015**, *5*, 6263.
- [94] M. Haruta, T. Kobayashi, H. Sano, N. Yamada, *Chem. Lett.* **1987**, *16*, 405.
- [95] D. A. Outka, R. J. Madix, *Surf. Sci.* **1987**, *179*, 351.

- [96] M. Haruta, S. Tsubota, T. Kobayashi, H. Kageyama, M. J. Genet, B. Delmon, *J. Catal.* **1993**, *144*, 175.
- [97] S. Tsubota, M. Haruta, T. Kobayashi, A. Ueda, Y. Nakahara in *Studies in Surface Science and Catalysis : Preparation of Catalysts V* (Eds.: G. Poncelet, P. A. Jacobs, P. Grange, B. Delmon), Elsevier, **1991**, pp. 695–704.
- [98] A. Ueda, T. Oshima, M. Haruta, *Appl. Catal., B* **1997**, *12*, 81.
- [99] M. Haruta, *Catal. Today* **1997**, *36*, 153.
- [100] M. Haruta, *Cattech* **2002**, *6*, 102.
- [101] M. Haruta, *J. Catal.* **1989**, *115*, 301.
- [102] B. Chen, C. Bai, R. Cook, J. Wright, C. Wang, *Catal. Today* **1996**, *30*, 15.
- [103] T. Aida, R. Higuchi, H. Niiyama, *Chem. Lett.* **1990**, *19*, 2247.
- [104] R. Ciriminna, E. Falletta, C. Della Pina, J. H. Teles, M. Pagliaro, *Angew. Chem., Int. Ed.* **2016**, *55*, 14210.
- [105] G. Wittstock, M. Bäumer, W. Dononelli, T. Klüner, L. Lührs, C. Mahr, L. V. Moskaleva, M. Oezaslan, T. Risse, A. Rosenauer et al., *Chem. Rev.* **2023**, *123*, 6716.
- [106] A. Corma, H. Garcia, *Chem. Soc. Rev.* **2008**, *37*, 2096.
- [107] R. G. Kelly, A. J. Frost, T. Shahrabi, R. C. Newman, *Metall. Trans. A* **1991**, *22*, 531.
- [108] D. H. Everett, *Pure and Applied Chemistry* **1972**, *31*, 577.
- [109] J. Erlebacher, R. Seshadri, *MRS Bull.* **2009**, *34*, 561.
- [110] J. Biener, A. Wittstock, L. A. Zepeda-Ruiz, M. M. Biener, V. Zielasek, D. Kramer, R. N. Viswanath, J. Weissmüller, M. Bäumer, A. V. Hamza, *Nat. Mater.* **2009**, *8*, 47.
- [111] A. Y. Chen, S. S. Shi, Y. D. Qiu, X. F. Xie, H. H. Ruan, J. F. Gu, D. Pan, *Microporous Mesoporous Mater.* **2015**, *202*, 50.
- [112] L. Y. Chen, T. Fujita, Y. Ding, M. W. Chen, *Adv. Funct. Mater.* **2010**, *20*, 2279.
- [113] P. N. Ciesielski, A. M. Scott, C. J. Faulkner, B. J. Berron, D. E. Cliffler, K. G. Jennings, *ACS Nano* **2008**, *2*, 2465.
- [114] B. Zugic, L. Wang, C. Heine, D. N. Zakharov, B. A. J. Lechner, E. A. Stach, J. Biener, M. Salmeron, R. J. Madix, C. M. Friend, *Nat. Mater.* **2017**, *16*, 558.
- [115] C. Xu, J. Su, X. Xu, P. Liu, H. Zhao, F. Tian, Y. Ding, *J. Am. Chem. Soc.* **2007**, *129*, 42.
- [116] V. Zielasek, B. Juergens, C. Schulz, J. Biener, M. M. Biener, A. V. Hamza, M. Bäumer, *Angew. Chem., Int. Ed.* **2006**, *45*, 8241.
- [117] B. Xu, G. F. Siler Cassandra, J. Madix Robert, M. Friend Cynthia, *Chem. - Eur. J.* **2014**, *20*, 4646.

- [118] A. Wittstock, V. Zielasek, J. Biener, C. M. Friend, M. Bäumer, *Science* **2010**, *327*, 319.
- [119] T. Fujita, P. Guan, K. McKenna, X. Lang, A. Hirata, L. Zhang, T. Tokunaga, S. Arai, Y. Yamamoto, N. Tanaka et al., *Nat. Mater.* **2012**, *11*, 775.
- [120] K. Hu, D. Lan, X. Li, S. Zhang, *Anal. Chem.* **2008**, *80*, 9124.
- [121] R. C. Newman, S. G. Corcoran, J. Erlebacher, M. J. Aziz, K. Sieradzki, *MRS Bull.* **1999**, *24*, 24.
- [122] J. Weissmüller, R. C. Newman, H.-J. Jin, A. M. Hodge, J. W. Kysar, *MRS Bull.* **2009**, *34*, 577.
- [123] J. Erlebacher, I. McCue, *Acta Mater.* **2012**, *60*, 6164.
- [124] X. Li, Q. Chen, I. McCue, J. Snyder, P. Crozier, J. Erlebacher, K. Sieradzki, *Nano Lett.* **2014**, *14*, 2569.
- [125] Y. Lu, Q. Wang, J. Sun, J. Shen, *Langmuir* **2005**, *21*, 5179.
- [126] D. M. Artymowicz, R. C. Newman, J. Erlebacher, *ECS Trans.* **2007**, *3*, 499.
- [127] G. Tammann, *Z. Anorg. Allg. Chem* **1919**, *107*, 1.
- [128] O. Kurtulus, P. Daggumati, E. Seker, *Nanoscale* **2014**, *6*, 7062.
- [129] K.-U. Lee, T. H. Tran, S. H. Kim, H.-J. Shin, *J. Alloys Compd.* **2017**, *713*, 132.
- [130] Y. Ding, Y.-J. Kim, J. Erlebacher, *Adv. Mater.* **2004**, *16*, 1897.
- [131] M. C. Dixon, T. A. Daniel, M. Hieda, D. M. Smilgies, M. H. W. Chan, D. L. Allara, *Langmuir* **2007**, *23*, 2414.
- [132] S. Parida, D. Kramer, C. A. Volkert, H. Rösner, J. Erlebacher, J. Weissmüller, *Phys. Rev. Lett.* **2006**, *97*, 035504-1–035504-4.
- [133] B. Xu, C. M. Friend, *Faraday Discuss.* **2011**, *152*, 307-20; discussion 393-413.
- [134] B. Xu, R. J. Madix, C. M. Friend, *Acc. Chem. Res.* **2014**, *47*, 761.
- [135] J. H. Bae, J.-H. Han, T. D. Chung, *Phys. Chem. Chem. Phys.* **2012**, *14*, 448.
- [136] J. Erlebacher, M. J. Aziz, A. Karma, N. Dimitrov, K. Sieradzki, *Nature* **2001**, *410*, 450.
- [137] D. A. Porter, K. E. Easterling, M. Y. Sherif in *Phase transformations in metals and alloys*, CRC Press, Boca Raton, FL, **2009**, pp. 302–309.
- [138] J. W. Cahn, *J. Chem. Phys.* **1965**, *42*, 93.
- [139] J. W. Cahn, *J. Chem. Phys.* **1959**, *30*, 1121.
- [140] J. W. Cahn, J. E. Hilliard, *J. Chem. Phys.* **1958**, *28*, 258.
- [141] J. W. Cahn, J. E. Hilliard, *J. Chem. Phys.* **1959**, *31*, 688.
- [142] S. J. Cooper, A. Bertei, P. R. Shearing, J. A. Kilner, N. P. Brandon, *SoftwareX* **2016**, *5*, 203.

- [143] V. Vivier, C. Cachet-Vivier, B. L. Wu, C. S. Cha, J. Y. Nedelec, L. T. Yu, *Electrochem. Solid-State Lett.* **1999**, *2*, 385.
- [144] S. Morandi, A. Minguzzi, *Electrochem. Commun.* **2015**, *59*, 100.
- [145] C. Cachet-Vivier, M. Keddou, V. Vivier, L. T. Yu, *J. Electroanal. Chem.* **2013**, *688*, 12.
- [146] C. Locatelli, A. Minguzzi, A. Vertova, P. Cava, S. Rondinini, *Anal. Chem.* **2011**, *83*, 2819.
- [147] L. Athouël, P. Arcidiacono, C. Ramirez-Castro, O. Crosnier, C. Hamel, Y. Dandeville, P. Guillemet, Y. Scudeller, D. Guay, D. Bélanger et al., *Electrochim. Acta* **2012**, *86*, 268.
- [148] R. Lin, P. L. Taberna, J. Chmiola, D. Guay, Y. Gogotsi, P. Simon, *J. Electrochem. Soc.* **2009**, *156*, A7.
- [149] E. Torralba, E. Laborda, A. Molina, C. Cachet-Vivier, S. Bastide, *ChemElectroChem* **2021**, *8*, 735.
- [150] M. L. Tremblay, M. H. Martin, C. Lebouin, A. Lasia, D. Guay, *Electrochim. Acta* **2010**, *55*, 6283.
- [151] M. Haensch, J. Behnken, L. Balboa, A. Dyck, G. Wittstock, *Phys. Chem. Chem. Phys.* **2017**, *19*, 22915.
- [152] Y. Ding, Z. Zhang in *Nanoporous Metals for Advanced Energy Technologies*, Springer International Publishing; Imprint: Springer, Cham, **2016**, pp. 1–7.
- [153] D. Menshukau, R. G. Compton, *Electroanalysis* **2008**, *20*, 2387.
- [154] J. Zhang, C. J. Slevin, C. Morton, P. Scott, D. J. Walton, P. R. Unwin, *J. Phys. Chem. B* **2001**, *105*, 11120.
- [155] C. J. Slevin, P. R. Unwin, *J. Am. Chem. Soc.* **2000**, *122*, 2597.
- [156] J. Rodríguez-López, M. A. Alpuche-Avilés, A. J. Bard, *J. Am. Chem. Soc.* **2008**, *130*, 16985.
- [157] J. Rodríguez-López, A. Minguzzi, A. J. Bard, *J. Phys. Chem. C* **2010**, *114*, 18645.
- [158] D. Zigah, J. Rodríguez-López, A. J. Bard, *Phys. Chem. Chem. Phys.* **2012**, *14*, 12764.
- [159] S. Trasatti, O. A. Petrii, *Pure Appl. Chem.* **1991**, *63*, 711.
- [160] B. E. Conway, *Prog. Surf. Sci.* **1995**, *49*, 331.
- [161] G. Tremiliosi-Filho, L. H. Dall'Antonia, G. Jerkiewicz, *J. Electroanal. Chem.* **1997**, *422*, 149.
- [162] D. Chen, Q. Tao, L. W. Liao, S. X. Liu, Y. X. Chen, S. Ye, *Electrocatalysis* **2011**.
- [163] R. Cornut, C. Lefrou, *J. Electroanal. Chem.* **2007**, *604*, 91.
- [164] M. Haensch, L. Balboa, M. Graf, A. R. Silva Olaya, J. Weissmüller, G. Wittstock, *ChemElectroChem* **2019**, *6*, 3160.
- [165] C. Kuss, N. A. Payne, J. Mauzeroll, *J. Electrochem. Soc.* **2016**, *163*, H3066.

- [166] D.-W. Chung, M. Ebner, D. R. Ely, V. Wood, R. Edwin García, *Modell. Simul. Mater. Sci. Eng.* **2013**, *21*, 74009.
- [167] B. Tjaden, S. J. Cooper, D. J. L. Brett, D. Kramer, P. R. Shearing, *Curr. Opin. Chem. Eng.* **2016**, *12*, 44.
- [168] K. Sieradzki, N. Dimitrov, D. Movrin, C. McCall, N. Vasiljevic, J. Erlebacher, *J. Electrochem. Soc.* **2002**, *149*, B370.
- [169] R. Li, K. Sieradzki, *Phys. Rev. Lett.* **1992**, *68*, 1168.
- [170] M. Graf, B. Roschning, J. Weissmüller, *J. Electrochem. Soc.* **2017**, *164*, C194.
- [171] M. Nebel, S. Neugebauer, K. Eckhard, W. Schuhmann, *Electrochem. Commun.* **2013**, *27*, 160.
- [172] H. Okamoto, T. B. Massalski, *Bulletin of Alloy Phase Diagrams* **1983**, *4*, 30.
- [173] L. Shen, Z. Chen, *Chem. Eng. Sci.* **2007**, *62*, 3748.
- [174] B. Ghanbarian, A. G. Hunt, R. P. Ewing, M. Sahimi, *Soil Sci. Soc. Am. J.* **2013**, *77*, 1461.
- [175] J. Hoogschagen, *Ind. Eng. Chem.* **1955**, *47*, 906.
- [176] R. E. D. La Rue, C. W. Tobias, *J. Electrochem. Soc.* **1959**, *106*, 827.
- [177] M. Ebner, D.-W. Chung, R. E. García, V. Wood, *Adv. Energy Mater.* **2014**, *4*.
- [178] I. V. Thorat, D. E. Stephenson, N. A. Zacharias, K. Zaghbi, J. N. Harb, D. R. Wheeler, *J. Power Sources* **2009**, *188*, 592.
- [179] D. Kehrwald, P. R. Shearing, N. P. Brandon, P. K. Sinha, S. J. Harris, *J. Electrochem. Soc.* **2011**, *158*, A1393.
- [180] M. Ebner, V. Wood, *J. Electrochem. Soc.* **2015**, *162*, A3064-A3070.
- [181] J. Newman, W. Tiedemann, *AIChE Journal* **1975**, *21*, 25.
- [182] D. E. Hughes, *Anal. Chem.* **1985**, *57*, 555.
- [183] M. Nebel, S. Neugebauer, K. Eckhard, W. Schuhmann, *Electrochem. Commun.* **2013**, *27*, 160.
- [184] R. Cornut, C. Lefrou, *J. Electroanal. Chem.* **2007**, *608*, 59.
- [185] X.-B. Cheng, R. Zhang, C.-Z. Zhao, F. Wei, J.-G. Zhang, Q. Zhang, *Adv. Sci.* **2016**, *3*, 1500213.
- [186] M. Winter, B. Barnett, K. Xu, *Chem. Rev.* **2018**, *118*, 11433.
- [187] S. M. E. Peled, *J. Electrochem. Soc.* **2017**, *164*.
- [188] Q. Xu, Y. Yang, H. Shao, *Phys. Chem. Chem. Phys.* **2015**, *17*, 20398.
- [189] H. Bülter, F. Peters, G. Wittstock, *Energy Technol.* **2016**, *4*, 1486.

- [190] H. Bülter, M. Sternad, E. d. Santos Sardinha, J. Witt, C. Dosche, M. Wilkening, G. Wittstock, *J. Electrochem. Soc.* **2016**, *163*, A504-A512.
- [191] B. Krueger, L. Balboa, J. F. Dohmann, M. Winter, P. Bieker, G. Wittstock, *ChemElectroChem* **2020**, *7*, 3590.
- [192] B. Jagger, M. Pasta, *Joule* **2023**, *7*, 2228.
- [193] M. Winter, *Z. Phys. Chem. (Muenchen, Ger.)* **2009**, *223*, 1395.
- [194] S. J. An, J. Li, C. Daniel, D. Mohanty, S. Nagpure, D. L. Wood, *Carbon* **2016**, *105*, 52.
- [195] P. Lu, C. Li, E. W. Schneider, S. J. Harris, *J. Phys. Chem. C* **2014**, *118*, 896.
- [196] S. Park, R. Chaudhary, S. A. Han, H. Qutaish, J. Moon, M.-S. Park, J. H. Kim, *Energy Mater.* **2023**, *3*.
- [197] D. Aurbach, *J. Power Sources* **2000**, *89*, 206.
- [198] D. Aurbach, B. Markovsky, A. Shechter, Y. Ein-Eli, H. Cohen, *J. Electrochem. Soc.* **1996**, *143*, 3809.
- [199] S. H. Kang, D. P. Abraham, A. Xiao, B. L. Lucht, *J. Power Sources* **2008**, *175*, 526.
- [200] E. Peled, D. Bar Tow, A. Merson, A. Gladkich, L. Burstein, D. Golodnitsky, *J. Power Sources* **2001**, *97-98*, 52.
- [201] K. Edström, M. Herstedt, D. P. Abraham, *J. Power Sources* **2006**, *153*, 380.
- [202] D. Bar-Tow, E. Peled, L. Burstein, *J. Electrochem. Soc.* **1999**, *146*, 824.
- [203] A. M. Andersson, A. Henningson, H. Siegbahn, U. Jansson, K. Edström, *J. Power Sources* **2003**, *119-121*, 522.
- [204] M. B. Pinson, M. Z. Bazant, *J. Electrochem. Soc.* **2013**, *160*, A243-A250.
- [205] K. Xu, *Chem. Rev.* **2004**, *104*, 4303.
- [206] D. Aurbach, K. Gamolsky, B. Markovsky, Y. Gofer, M. Schmidt, U. Heider, *Electrochim. Acta* **2002**, *47*, 1423.
- [207] M. Dollé, S. Grugeon, B. Beaudoin, L. Dupont, J. M. Tarascon, *J. Power Sources* **2001**, *97-98*, 104.
- [208] E. dos Santos Sardinha, M. Sternad, H. M. R. Wilkening, G. Wittstock, *ACS Appl. Energy Mater.* **2019**, *2*, 1388.
- [209] H. P. Chen, J. W. Fergus, B. Z. Jang, *J. Electrochem. Soc.* **2000**, *147*, 399.
- [210] J. S. Newman, N. P. Balsara in *Electrochemical systems, The electrochemical society series*, Wiley, Hoboken NJ, **2019**, pp. 365–397.
- [211] M. Doyle, J. Newman, A. S. Gozdz, C. N. Schmutz, J.-M. Tarascon, *J. Electrochem. Soc.* **1996**, *143*, 1890.

- [212] Q. Zhao, Y. Deng, N. W. Utomo, J. Zheng, P. Biswal, J. Yin, L. A. Archer, *Nat. Commun.* **2021**, *12*, 1.
- [213] A. Ferrese, P. Albertus, J. Christensen, J. Newman, *J. Electrochem. Soc.* **2012**, *159*, A1615-A1623.
- [214] M. Doyle, T. F. Fuller, J. Newman, *J. Electrochem. Soc.* **1993**, *140*, 1526.
- [215] S.-I. Lee, U.-H. Jung, Y.-S. Kim, M.-H. Kim, D.-J. Ahn, H.-S. Chun, *Korean J. Chem. Eng.* **2002**, *19*, 638.
- [216] S. G. Meibuhr, *J. Electrochem. Soc.* **1970**, *117*, 56.
- [217] M. W. Verbrugge, B. J. Koch, *J. Electroanal. Chem.* **1994**, *367*, 123.
- [218] H. P. Chen, J. W. Fergus, B. Z. Jang, *J. Electrochem. Soc.* **2000**, *147*, 399.
- [219] G. Zampardi, F. La Mantia, W. Schuhmann, *Electrochem. Commun.* **2015**, *58*, 1.

## 9. Own publications and conference contributions

### 9.1 Publications

[X1] M. Haensch, J. Behnken, L. Balboa, A. Dyck, G. Wittstock, *Phys. Chem. Chem. Phys.* **2017**, *19*, 22915.

[X2] M. Haensch, L. Balboa, M. Graf, A. R. Silva Olaya, J. Weissmüller, G. Wittstock, *ChemElectroChem* **2019**, *6*, 3160.

[X3] B. Krueger, L. Balboa, J. F. Dohmann, M. Winter, P. Bieker, G. Wittstock, *ChemElectroChem* **2020**, *7*, 3590.

### 9.2 Conference contributions

[Y1] L. Balboa, G. Wittstock. Modeling and simulation of transient scanning electrochemical microscopy response of porous electrodes. 67th Annual Meeting of the International Society of Electrochemistry, The Hague, The Netherlands, Aug. 21 – 26, 2016; Conference – Poster Contribution

[Y2] L. Balboa, G. Wittstock. Modeling and Simulation of Transient SECM (Scanning Electrochemical Microscopy) Response of Porous Electrodes. COMSOL Conference. Munich, Germany, Oct. 12-14, 2016; Conference – Poster Contribution

[Y3] L. Balboa, M. Hänsch, J. Behnken, G. Wittstock. Modeling and Simulation of Redox Titration of Metal Oxides at Porous Microelectrodes. COMSOL Conference. Rotterdam, The Netherlands, Oct 18-20, 2017; Conference – Poster Contribution

## 10. Curriculum Vitae

### Personal Data

First and last names: Luis Humberto Balboa Blanco  
Date of birth: 23.04.1981  
Place of birth: Mexico City  
Nationality: Mexican

### Education

Since 05/2015            Doctoral candidate at the Carl von Ossietzky University of Oldenburg

10/2008-04/2014        Master program of Process Energy and Environmental Systems Engineering at the Technical University of Berlin (TU-Berlin)

08/2005-04/2013        Master program in Chemical Sciences at the National Autonomous University of Mexico (UNAM)

08/2000-01/2006        Bachelor of Science in Chemical Engineering, National Autonomous University of Mexico (UNAM)

Ich versichere hiermit, dass ich diese Arbeit selbständig verfasst und nur die angegebenen Quellen und Hilfsmittel benutzt habe. Während des Arbeitens an der Dissertation, sind die unter „Publications“ aufgelisteten Veröffentlichungen entstanden. Veröffentlichte Ergebnisse aus dieser Arbeit wurden an den gegebenen Stellen dementsprechend deklariert. Die Leitlinien der guten wissenschaftlichen Praxis der Carl von Ossietzky Universität Oldenburg sind mir bekannt und wurden zur Fertigung dieser Arbeit befolgt. Des Weiteren bestätige ich, dass ich im Zusammenhang mit dem Promotionsvorhaben keine kommerziellen Vermittlungs- oder Beratungsdienste (Promotionsberatung) in Anspruch genommen habe. Die Dissertation hat weder zu Teilen noch in Gänze einer anderen wissenschaftlichen Hochschule zur Begutachtung in einem Promotionsverfahren vorgelegen.

Luis Humberto Balboa Blanco

Berlin, den 08.10.2025